TUNING THE ELECTROCHEMICAL PROPERTIES OF METAL DOPANTS SUPPORTED ON TRANSITION METAL DICHALCOGENIDES

by

Erika Yadira Meza

A Dissertation

Submitted to the Faculty of Purdue University

In Partial Fulfillment of the Requirements for the degree of

Doctor of Philosophy

Department of Chemistry

West Lafayette, Indiana

May 2021

THE PURDUE UNIVERSITY GRADUATE SCHOOL

STATEMENT OF COMMITTEE APPROVAL

Dr. Christina Li, Chair

Department of Chemistry

Dr. Tong Ren

Department of Chemistry

Dr. Jianguo Mei

Department of Chemistry

Dr. Jonathan J. Wilker

Department of Chemistry

Approved by:

Dr. Christine Hrycyna

To my parents, I would not be where I am without your love and support.

To my brother and sister, for always being there for me.

Thank you for believing in me.

ACKNOWLEDGMENTS

First, I want to express my gratitude to my advisor and mentor Dr. Christina Li. Christina, since day one I have admired you for your passion and creativity towards science. Your enthusiasm and professional skills were a few of the things that made me decide to work with you. I am very thankful to have learned from you throughout my graduate studies, because you motivated me about my research and helped me grow professionally. Thank you for your guidance, your support, and the opportunity to work with you.

I also want to thank my committee members, Dr. Ren Tong, Dr. Jianguo Mei, and Dr. Jonathan Wilker, for their discussions and advice to improve my research presentations. All of you are a great inspiration to me.

To the Li group, thank you so much for being with me in this journey. I am grateful for all of you, for the lab environment we created and for always being available to help each other in our projects. Thank you for all your feedback and advice during presentations and group meetings, and for our shared love for sushi and bubble tea. It has been a pleasure to work with all of you. Eve and Nicole, I am very happy to have met you. I respect both of you as my friends and my colleagues, and I appreciate our small and not so small conversations about our research and our personal lives. I wish the very best to both of you.

Finally, I want to acknowledge my family. Dad, thank you for your constant reminder of how much you care for me and how much you wanted me to succeed. I appreciate all our talks and your advice. Mom, thank you for letting me go and pursue my career goals. I know it is very hard for you, but you are and always will be the greatest motivation I have. Osmara, thank you for being a constant presence in my graduate career, either physically or virtually. I don’t know what I would have done without you. Oscar, thank you so much for all the good laughs and talks that we had. To my best friend Chavez, thank you for your constant reminder and motivation speeches to pursue my career goals. To my family in Mexico, thank you so much for always supporting me and welcoming me with great food and company every time I went back to visit you.

TABLE OF CONTENTS

LIST OF TABLES

LIST OF FIGURES

ABSTRACT

Metal-doped transition metal dichalcogenides (TMDs) have emerged as versatile optoelectronic, magnetic, and electrocatalytic materials due their tunable properties and two-dimensional structure. Functionalizing the surface of the TMD with catalytically relevant transition metal ions is a particularly intriguing strategy to generate single atom catalysts (SACs) with tunable local geometry and electronic properties. Although solution-phase methods have been developed to dope transition metal single atoms on TMDs surfaces, control over the local coordination environment of the doped metal atom remains a major challenge. In this dissertation, we develop a solution-phase synthetic method to controllably functionalize TMDs with transition metal ions. We are able to achieve control over the adsorbate morphology, ranging from single atoms to multimetallic clusters, and local coordination environment. We then utilize this range of doped TMDs to understand how metal atom coordination and clustering impact electrocatalytic activity in the oxygen evolution and oxygen reduction reactions.

We utilize colloidal WS_2 nanosheets as the starting point for our synthetic method, which as synthesized, are completely inert toward metal functionalization on the basal plane. Therefore, we use n-butyllithium to generate nucleophilic sulfide sites on the basal planes that are capable of binding first-row transition metal ions. The dopants are subsequently introduced in solution and permitted to passively adsorb to the WS_2 surface. Using $NiCl_2$, it is possible to achieve Ni concentrations ranging from 9% to 47% with respect to W simply by varying the amount of $NiCl_2$ introduced in solution. Through X-ray absorption spectroscopy (XAS) and high-resolution scanning transmission electron microscopy (HR-STEM) coupled to electron energy loss spectroscopy (EELS), we show that Ni single atoms predominant at low loadings of Ni ($\leq$ 14 at.%) and mixtures of single atoms and multimetallic clusters exist at higher loadings. Electrochemical studies reveal that the single atom Ni-WS_2 sample experiences the strongest electronic perturbation due to the WS_2 nanosheet and thus, a much higher intrinsic activity for the alkaline oxygen evolution reaction.

Using the same solution-phase strategy, we dope isolated Co atoms onto the WS_2 nanosheets and develop a post-sulfidation process in order to explicitly control the cobalt-sulfur coordination environment at the WS_2 surface. Bulk cobalt sulfide materials are known catalysts for the electrochemical oxygen reduction reaction in neutral electrolyte, but the active site in these

materials has been difficult to determine due to the non-uniform and dynamic nature of the cobalt and sulfur atoms at the surface of the bulk material. By studying our Co-doped WS_2 materials with Co-S coordination ranging from monodentate to tetradentate, we show that the optimal active site for the oxygen reduction reaction features three-fold Co-S binding to the surface. These single atom Co-doped WS_2 materials serve as important structural models for bulk cobalt sulfides and provide design principles for active site geometry and electronics in order to achieve more efficient electrocatalytic reactivity.

CHAPTER 1. SOLUTION-PHASE ACTIVATION AND FUNCTIONALIZATION OF COLLOIDAL WS_2 NANOSHEETS WITH NI SINGLE ATOMS

1.1 Abstract

Single atom functionalization of transition metal dichalcogenide (TMD) nanosheets is a powerful strategy to tune the optical, magnetic, and catalytic properties of two-dimensional materials. In this work, we demonstrate a simple solution phase method to generate nucleophilic sulfide sites on colloidal WS_2 nanosheets that subsequently serve as ligands for Ni single atoms. These materials can be controllably functionalized with varying amounts of Ni on the surface ranging from 9% to 47% coverage with respect to W. High-resolution scanning transmission electron microscopy coupled to electron energy loss spectroscopy and X-ray absorption spectroscopy indicate that adsorbed Ni species bind as single atoms at low coverage and a mixture of single atoms and multimetallic clusters at high coverage. The Ni single atoms adsorbed on WS_2 show altered electronic properties, and both the electronic perturbation and isolated atom geometry play a role in enhancing the intrinsic catalytic activity of Ni-WS_2 samples for the electrochemical oxygen evolution reaction.

1.2 Introduction

Functionalization of transition metal dichalcogenide (TMD) nanosheets with metal single atoms has important potential applications in optoelectronic materials, magnetism, and catalysis.[1-5] Previous studies on doped TMDs, focusing primarily on MoS_2, have utilized hydrothermal syntheses, chemical vapor deposition, chemical vapor transport, sonochemical synthesis, or electrodeposition to achieve substitutional doping of transition metal atoms into the TMD lattice.[6-14] These studies have demonstrated that Pt and Pd single atoms doped or adsorbed onto MoS_2 monolayers enhance the reactivity of the TMD for the hydrogen evolution reaction, and Co single atoms introduce oxygen evolution reactivity.[6,9,10,14-16] However, precise control over the

localization and speciation of the dopant is difficult to control using these synthetic methods. For dopants with catalytic functionality in particular, controlling the coordination environment as well as its localization as a surface *versus* substitutional dopant is critical to achieving high catalytic turnover. We postulated that a solution-phase surface functionalization strategy, based in part on the covalent functionalization of TMDs with electrophilic organic moieties, would serve as a general method to anchor catalytically accessible single transition metal sites onto activated metal chalcogenide surfaces through coordinate covalent interactions.[17-20]

While much of the synthetic work on transition metal dichalcogenide doping has focused on MoS_2, tungsten disulfide has similarly attractive optical and catalytic properties with the added advantage of being readily accessible *via* colloidal synthesis.[21-26] Rather than requiring a harsh exfoliation process from the bulk crystal to access monolayer structures, it is possible to synthesize monodisperse nanosheets of WS_2 using colloidal methods, thus providing an ideal platform to study the mild activation and functionalization of WS_2 surfaces with transition metal ions. In this work, we demonstrate a simple solution phase method to generate activated sites on a WS_2 nanosheet that subsequently serve as ligands for Ni single atoms. These materials can be controllably functionalized with varying amounts of Ni on the surface, and the Ni sites show unique electronic properties and reactivity towards the oxygen evolution reaction.

1.3 Results and Discussion

1.3.1 Synthesis

In this work, we put forward a colloidal strategy towards single atom functionalization of WS_2 nanosheets. Colloidal 1T-WS_2 nanosheets are synthesized based on a literature method using oleylamine as the ligand, which results in nanosheets with 100 nm diameter and ~10-14 monolayer height (Figures 1.1a and 1.2).[21] X-ray diffraction and UV-Visible spectroscopy match literature reports for the 1T or distorted 1T phase of WS_2 (Figure 1.3). After several cycles of centrifugation and redispersion to remove excess precursor and ligand, the purified nanosheets are colloidally stable in hexanes when triethylamine is added as a stabilizer. As-synthesized, we anticipate that these WS_2 nanosheets have relatively low defect density along the basal plane with functionalization sites only present at the edges of the nanosheet, evidenced by the near-zero ζ-

potential of –2.01 mV. As a result, treatment of as-synthesized nanosheets with a transition metal ion, in this case, $NiCl_2$, results in negligible incorporation of Ni (Figure 1.4, Table 1.1).

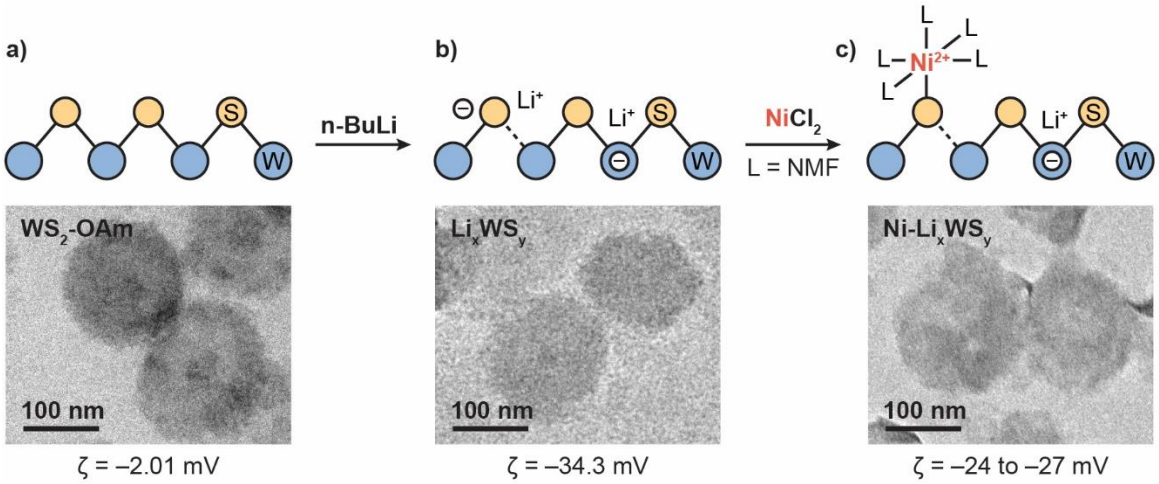

Figure 1.1. Schematic structure, corresponding TEM image, and ζ-potential at each step in the solution-phase activation and functionalization of colloidal WS_2 nanosheets.

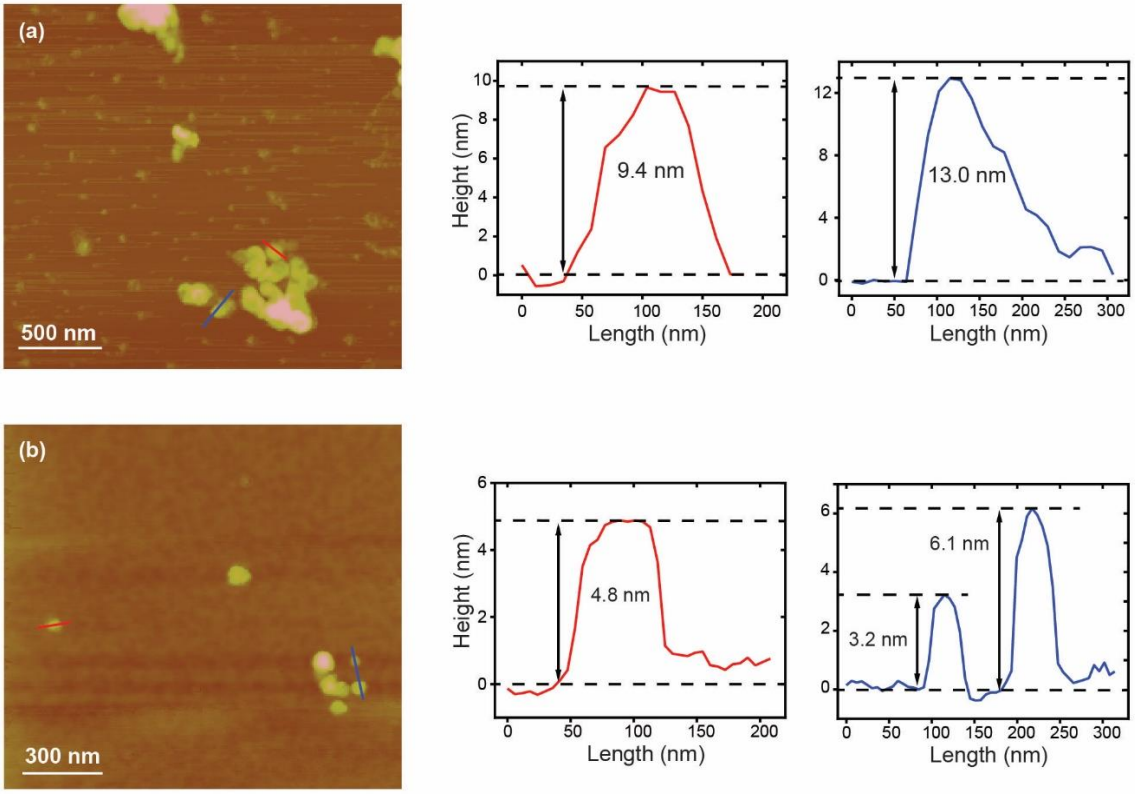

Figure 1.2. AFM images with height profiles on two different areas for **(a)** as-synthesized WS_2-OAm and **(b)** Li_xWS_y after n-BuLi treatment.

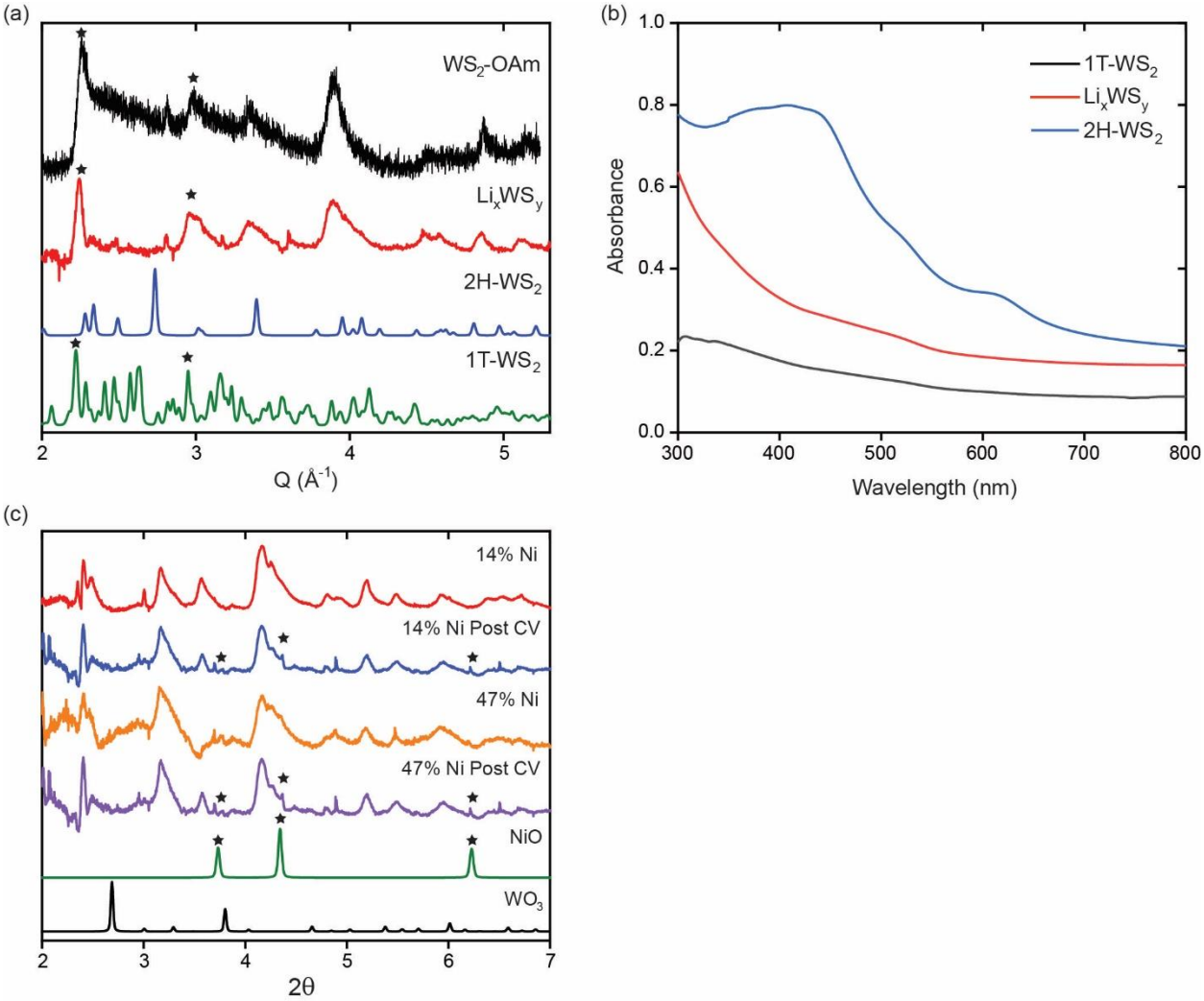

Figure 1.3. **(a)** Experimental XRD pattern for WS_2-OAm and Li_xWS_y and reference XRD patterns for 1T-WS_2 and 2H-WS_2. The 1T-WS_2 reference pattern was generated theoretically based on the previously reported structure of ReS_2. **(b)** UV-Vis spectra of WS_2-OAm (black) and Li_xWS_y (red) showing the retention of the 1T phase after lithiation. A sample of the semiconducting 2H-WS_2 phase (blue) was independently synthesized as a comparison.[6] **(c)** XRD pattern for Ni-Li_xWS_y pre and post 75 CV scans along with reference XRD patterns for NiO and WO_3. NiO is seen after oxidative conditions.

In order to generate free sulfide functionalization sites on the basal plane, we adapted a strategy used for the exfoliation and covalent functionalization of bulk MoS_2.[17] N-Butyllithium (n-BuLi) is commonly used to exfoliate MoS_2 monolayers from bulk crystals based on the principle that Li^+ ions intercalate between layers when n-BuLi injects negative charge into the TMD layer.[27] After exfoliation, both nucleophilic and electrophilic organic molecules have been introduced onto the surface, indicating that complex defect chemistry occurs concurrently to exfoliation during the

n-BuLi treatment. It has been postulated that both sulfur vacancies and dangling sulfides are generated, which interact with nucleophiles and electrophiles, respectively.[17,18,28-33] In this work, the dangling sulfide defects will serve as binding moieties to introduce Lewis-acidic transition metal ions onto the surface of colloidal WS_2 nanosheets (Figure 1.1b-c).

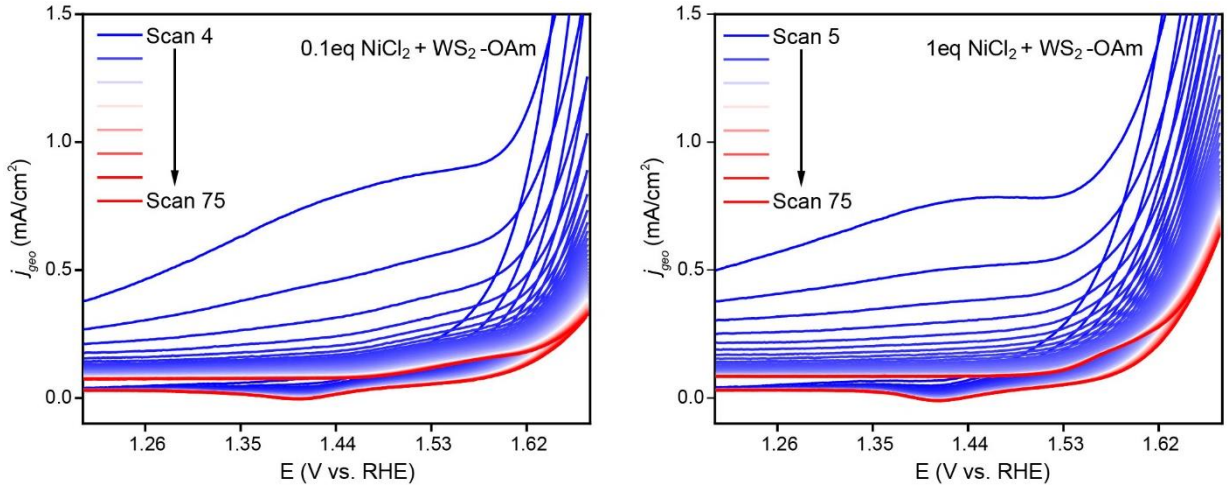

Figure 1.4. CV scans of the Ni(II/III) redox region for Ni-treated WS_2-OAm nanosheets without n-BuLi activation at two different solution concentrations of $NiCl_2$.

Table 1.1. Ni reduction peak positions and peak areas for Ni-treated WS_2-OAm nanosheets without n-BuLi activation. As a comparison, 2 eq. $NiCl_2$ added to n-BuLi treated WS_2 has ~30-fold higher Ni RF (see **Table 1.7**).

	Ni(II/III) E_{red} (V vs. RHE)	**Ni Red. Area ($\mu C/cm^2$)**	**Ni Roughness Factor (RF)**
0.2 eq. $NiCl_2$ + WS_2-OAm	1.41	37	0.15
2 eq. $NiCl_2$ + WS_2-OAm	1.41	38	0.15

The n-BuLi treatment conditions reported in the literature are optimized for chemical exfoliation of bulk MoS_2 and are necessarily harsh due to the kinetic limitations of intercalating ions into a micron-sized crystal. In our colloidal WS_2 nanosheets, because the material is already ~10-14 layers in thickness, we anticipate much milder conditions would be warranted to generate the desired functionalization sites on the surface. We studied this process in some detail to

understand the rate of defect formation and the nature of the defects formed during this process by varying n-BuLi treatment concentration and time. Using conditions akin to those reported for the chemical exfoliation of bulk MoS_2 (1.6 M n-BuLi in hexanes, 18 hours), we observe near complete degradation of the colloidal WS_2 nanosheets.

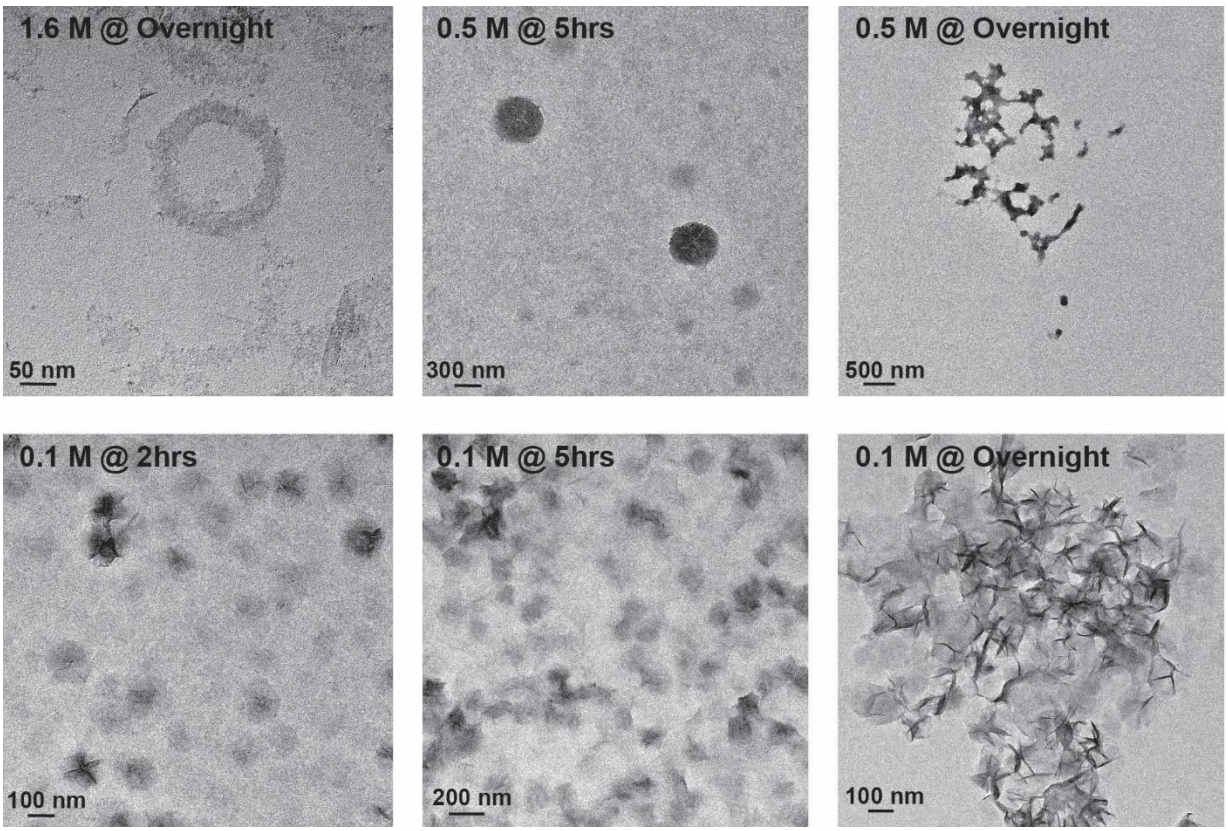

Figure 1.5. TEM images of WS_2 nanosheet morphology after n-BuLi treatments of varying concentration and duration.

The centers of the nanosheets are completely etched away, leaving behind ring-like structures and small flakes (Figure 1.5). Slightly milder conditions reduce etching but induce nanosheet aggregation. These data clearly indicate that n-BuLi does not merely inject negative charge into the two-dimensional layer but rather actively breaks W–S bonds in the lateral dimension to form undercoordinated W ions and dangling sulfides, and in the extreme case, to completely dissolve both W and S into solution. We modulated our conditions accordingly to generate the desired defects without destroying the morphology. Treating the nanosheets in 0.1 M n-BuLi for only two hours, we observe that the overall morphology and crystal structure remain

intact but the ζ-potential drops precipitously to –34.3 mV, and the material becomes completely soluble in polar solvents such as water and N-methylformamide (NMF) (Figure 1.1b , 1.6). While the lateral dimension of the nanosheets remains largely intact, the transverse dimension is strongly affected by the n-BuLi treatment. Atomic force microscopy (AFM) images reveal that the nanosheets are reduced in thickness from 10-14 monolayers to 3-6 monolayers (Figure 1.2). The total concentration of tungsten in solution based on inductively coupled plasma-optical emission spectroscopy (ICP-OES) is also reduced correspondingly from 9.6 mM in the as-synthesized colloidal WS_2 solution to 6.2 mM after lithiation.

To dope the nanosheets, we then introduce $NiCl_2$ to the colloidal solution of lithiated tungsten disulfide (Li_xWS_y) at varying equivalents (0.1 eq. to 4 eq.) with respect to W and allow the NMF solution to stir for 24 hours at room temperature. Under these conditions, the $NiCl_2$ precursor remains completely soluble in NMF, and any unincorporated or weakly adsorbed Ni^{2+} is readily removed during the washing and centrifugation steps. We postulate that any Ni^{2+} species that remain on the surface after the cleaning procedure should be bound *via* covalent coordinate bonds rather than weak physisorption (Figure 1.1c).

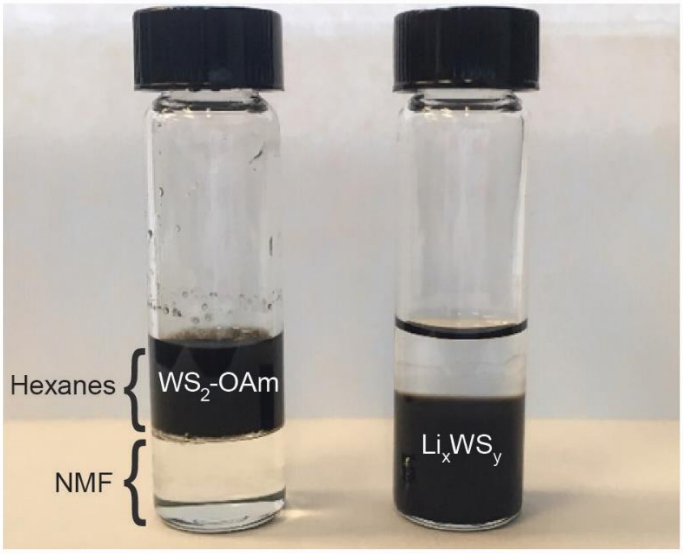

Figure 1.6. Photograph of as-synthesized WS_2 nanosheets capped with OAm in hexanes and after n-BuLi treatment, redispersed in NMF.

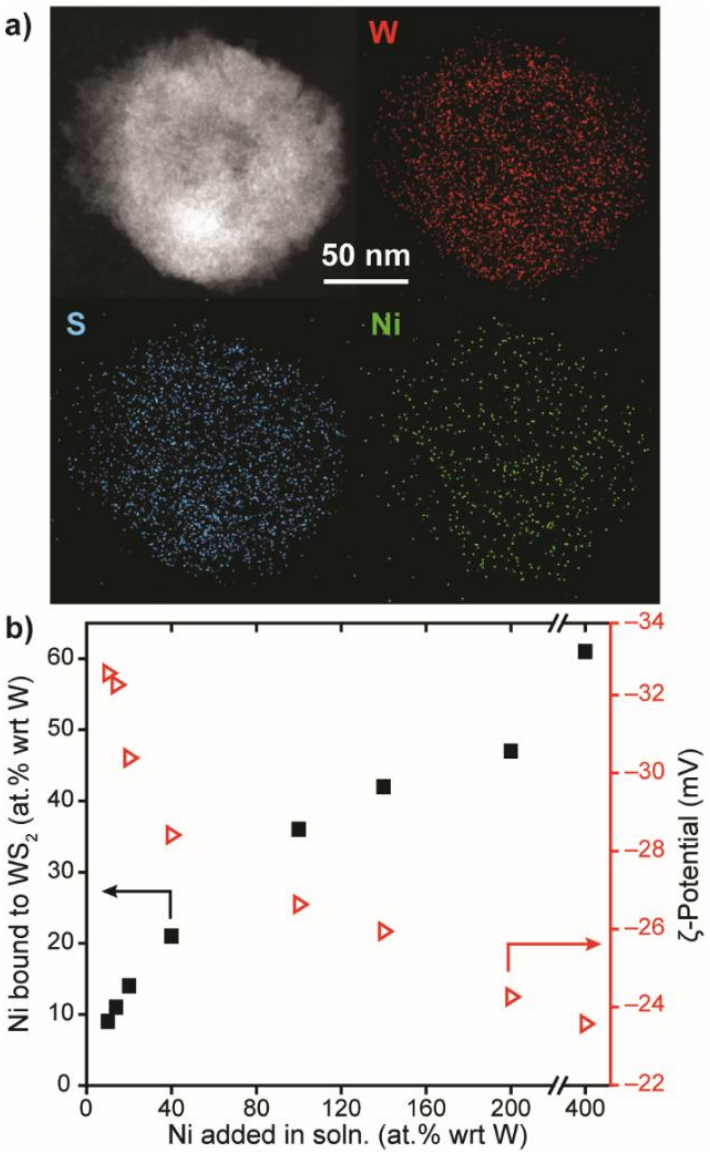

Figure 1.7. **(a)** STEM image and EDS maps for 36% Ni-Li_xWS_y, **(b)** Atomic percent Ni bound to WS_2 obtained from ICP-OES and ζ-potential as a function of Ni precursor added in solution.

1.4 Characterization

Using the colloidal activation and adsorption method described herein, we have generated seven different samples with wide ranging Ni loading on Li_xWS_y nanosheets. Transmission electron microscopy (TEM) and scanning transmission electron microscopy (STEM) coupled to energy-dispersive X-ray spectroscopy (EDS) mapping demonstrate that the morphology of the lithiated WS_2 nanosheets are retained after Ni^{2+} addition and that Ni atoms are co-localized and evenly distributed across the WS_2 nanosheets (Figure 1.7a, 1.8, 1.9). The STEM images and

elemental maps show no evidence of secondary nucleation or segregation of Ni-only nanostructures. Atomic ratios of W and Ni are obtained by EDS and ICP-OES, which show that the amount of Ni incorporated into the sample correlates with the atomic percent of Ni added in solution during the functionalization step (Table 1.2, 1.3). At a solution loading of 10 mol% $NiCl_2$ with respect to Li_xWS_y, approximately 9 at.% Ni relative to W actually adsorbs to the surface as determined by ICP-OES (Figure 1.7b).

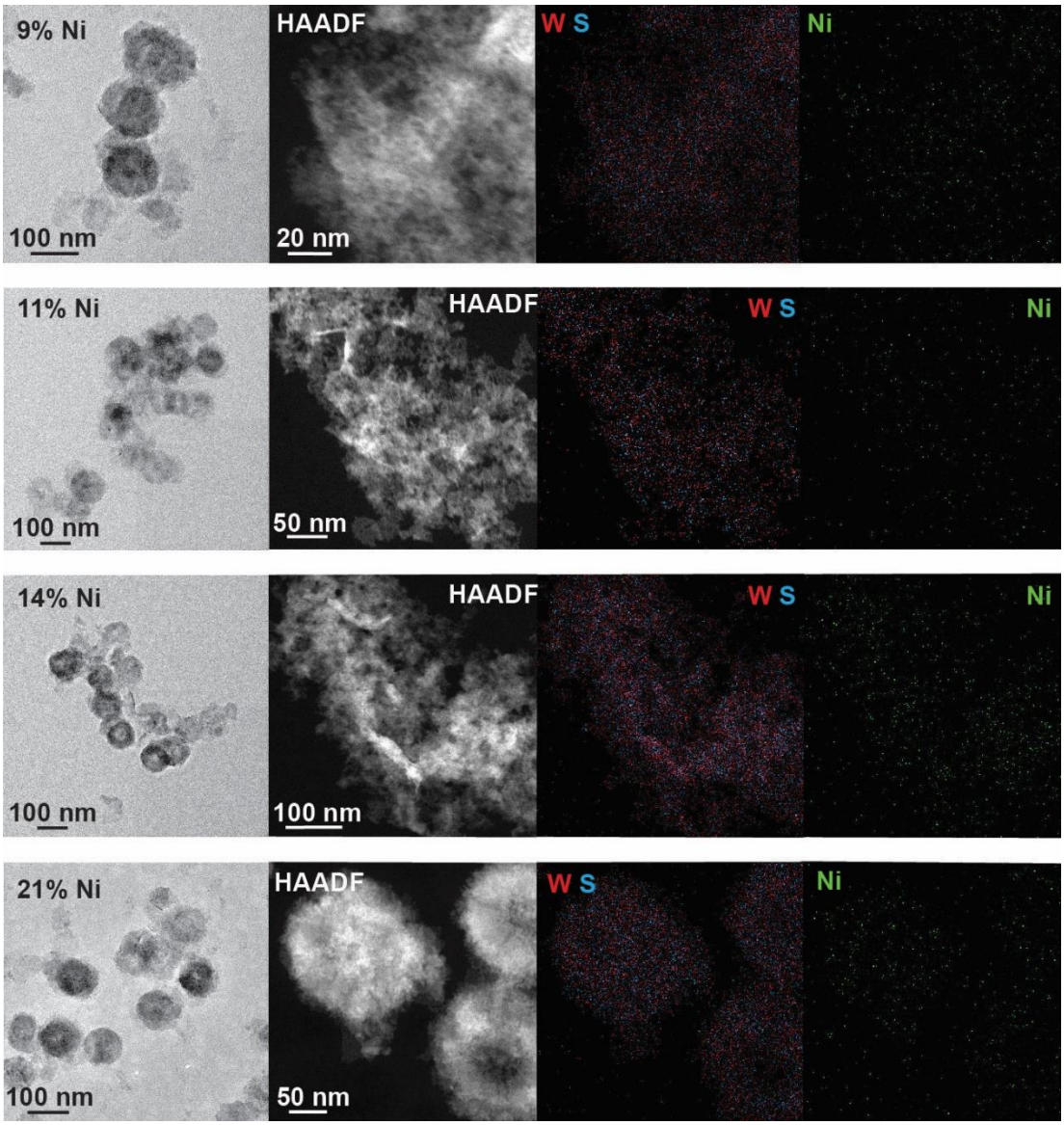

Figure 1.8. TEM, HAADF-STEM and EDS mapping of 9% to 21% Ni-Li_xWS_y samples showing a uniform distribution of Ni throughout theWS_2 nanosheets.

The percentage of bound Ni increases steadily with the amount of added $NiCl_2$ but begins to plateau at ~40% when the solution loading is increased beyond 140 mol%, suggesting that the total density of functionalization sites created by lithiation is limited to this regime. If we use a large excess of $NiCl_2$ (400 mol%), secondary nucleation of $Ni(OH)_2$ into 400 nm square platelets and obvious Ni segregation by EDS mapping is observed (Figure 1.10). The strong negative ζ-potential of the lithiated WS_2 nanosheets provides an initial indication that negatively charged and nucleophilic functionalization sites are present on the surface of Li_xWS_y.[17] Indeed, the magnitude of the negative ζ-potential drops steadily upon incorporation of Ni^{2+} (Figure 1.7b, Table 1.4). An initial steep decline in magnitude from –34 to –28 mV occurs with the first 20% of Ni loaded onto Li_xWS_y and is followed by a shallower decline in the plateau regime. At the plateau loading of 47% Ni atoms on the surface, the ζ-potential remains quite negative at –24 mV. These data indicate that nucleophilic sites make up only a fraction of the negative ζ-potential, and the remainder of the negative charge stays delocalized in the nanosheet. Nonetheless, the compensation of negative charge clearly indicates that Ni^{2+} adsorbs to the surface as a cationic species rather than secondary nucleating as neutral $Ni(OH)_2$ or NiS.

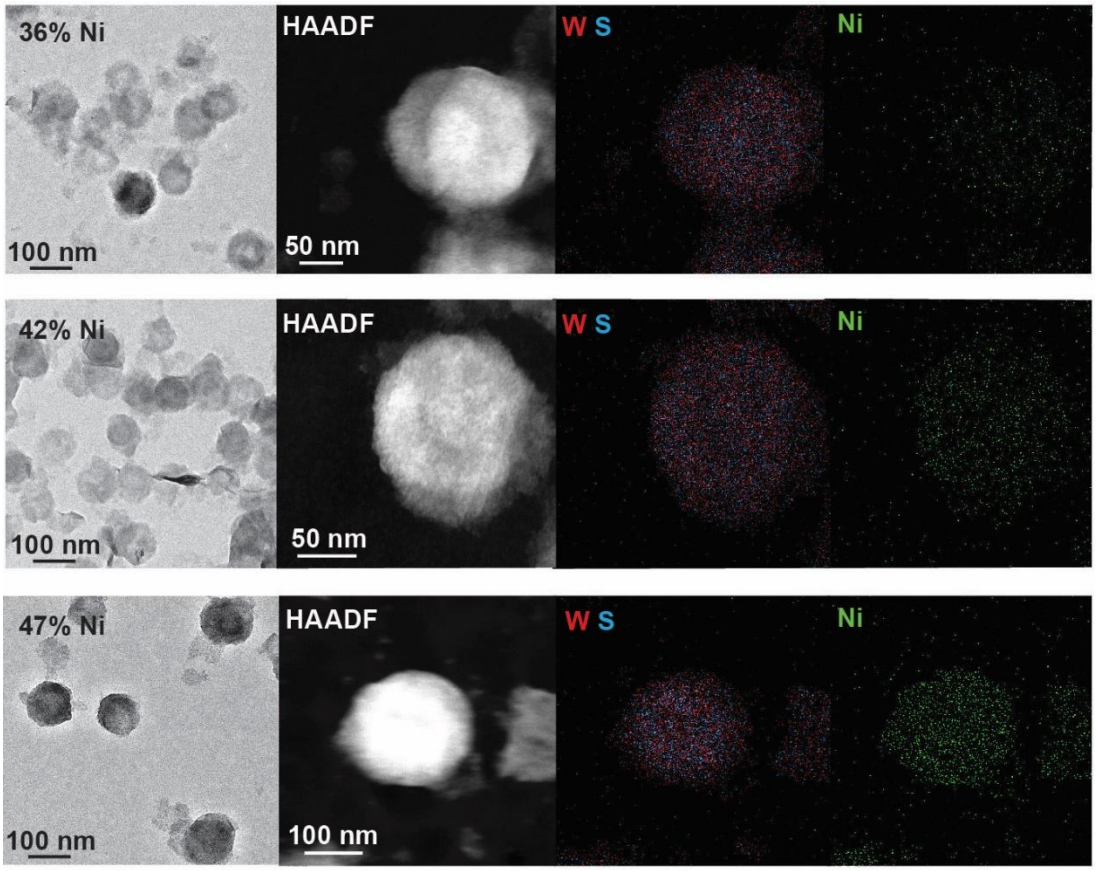

Figure 1.9. TEM, HAADF-STEM and EDS mapping of 36% to 47% Ni-Li_xWS_y samples showing a uniform distribution of Ni throughout theWS_2 nanosheets.

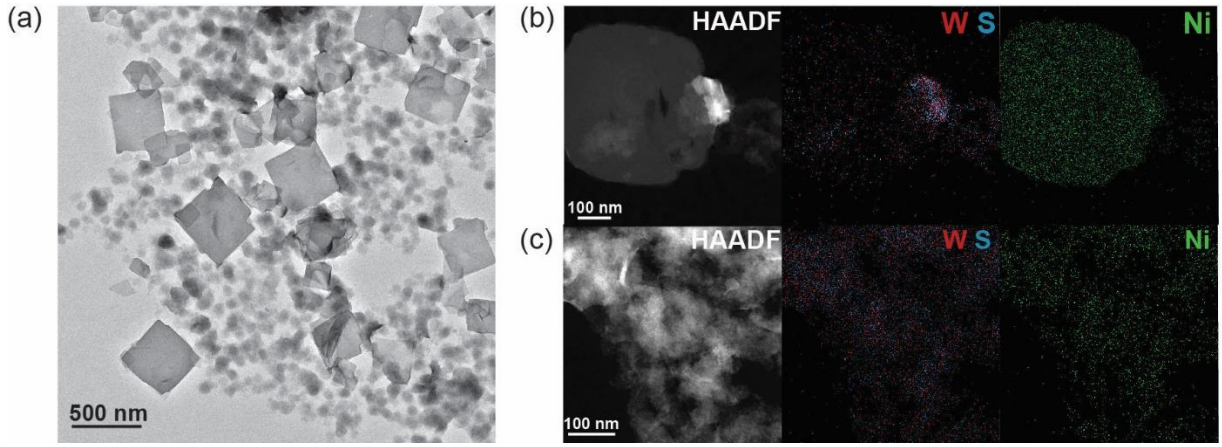

Figure 1.10. **(a)** TEM image of 61% Ni-Li_xWS_y showing the formation of secondary nucleated $Ni(OH)_2$ films on top of the Li_xWS_y nanosheets. HAADF and EDS elemental mapping showing **(b)** regions of major $Ni(OH)_2$ secondary nucleation and **(c)** regions where Ni remains uniformly distributed on the Li_xWS_y nanosheets.

Table 1.2. Summary of elemental analysis obtained using EDS. The tungsten M edge, sulfur K edge, and nickel K edge were used for quantification.

Sample	**W at.%**	**S at.%**	**Ni at.%**	**W:Ni (%)**	**W+Ni : S**
0.1 eq Ni wrt W	25	74	1	96 : 4	1 : 3
0.14 eq Ni wrt W	23	76	1	96 : 4	1 : 3
0.2 eq Ni wrt W	23	75	2	92 : 8	1 : 3
0.4 eq Ni wrt W	23	75	2	92 : 8	1 : 3
1.0 eq Ni wrt W	19	74	6	75 : 25	1 : 3
1.4 eq Ni wrt W	21	69	10	68 : 32	1 : 2
2.0 eq Ni wrt W	27	62	11	71 : 29	1 : 2
4.0 eq Ni wrt W	21	55	24	47 : 53	1 : 1
WS_2-OAm (no TEA in cleaning)	20	80	---	---	W : S → 1 : 4
WS_2 (TEA added in cleaning)	24	76	---	---	W : S → 1 : 3
Li_xWS_y	31	69	---	---	W : S → 1 : 2

Table 1.3. Summary of elemental analysis obtained using ICP-OES. These Ni at.% values used to label samples in the rest of the paper.

Sample	**Ni ppm**	**W ppm**	**Ni wt.%**	**W wt.%**	**Ni at.%**	**W at.%**
0.1 eq Ni wrt W	0.2	7.7	3.0	97	9	91
0.14 eq Ni wrt W	0.3	7.3	4.0	96	11	89
0.2 eq Ni wrt W	0.4	7.8	5.0	95	14	86
0.4 eq Ni wrt W	0.6	7.2	8.0	92	21	79
1.0 eq Ni wrt W	1.6	9.1	15	85	36	64
1.4 eq Ni wrt W	1.8	7.8	19	81	42	58
2.0 eq Ni wrt W	2.7	9.4	22	78	47	53
4.0 eq Ni wrt W	4.3	8.9	33	67	61	39

High-resolution STEM (HR-STEM) imaging of the Li_xWS_y, 14% Ni-Li_xWS_y, 36% Ni-Li_xWS_y, and 47% Ni-Li_xWS_y samples show a random pattern of high and low contrast regions on a 1-2 nm size scale, indicating that the n-BuLi activation step generates variable layer thicknesses on the basal plan due to non-uniform etching (Figure 1.11, 1.12a-b). While the bright regions are difficult to analyze due to multilayer stacking, the dimmer parts of the sample clearly show the well-defined hexagonal pattern of tungsten atoms expected for crystalline 1T-WS_2. Tungsten vacancies and internal voids scattered throughout the monolayer regions are also evident. In previous examples of single-atom doped MoS_2, the dopant is typically detected in HR-STEM images due to intensity differences in annular dark-field (ADF) Z-contrast between the dopant and Mo.[6,8,10-12,34-36] Analysis of monolayer regions in the 36% and 47% Ni-Li_xWS_y images reveal two distinct morphologies of extra-lattice intensity that can be assigned to the presence of Ni atoms (Figure 1.12a-b). In Figure 1.12c and 1.12e, an additional atom is located on a hollow or bridge site on top of the W lattice (h-Top) and appears interstitial to the underlying W atoms as evidenced by both the image and the integrated intensity line scan across the boxed atoms. In Figure 1.12d and 1.12f, a Ni atom is located directly on top of a W atom (W-Top), making it particularly bright relative to its neighbors. Based on the crystal structure of 1T-WS_2, the h-Top configuration involves a Ni atom bound to a single sulfide ligand while the W-Top includes up to three sulfide coordination sites. Both of these configurations have been computationally predicted and experimentally observed for transition metal adsorbates on MoS_2.[3,10,16,37]

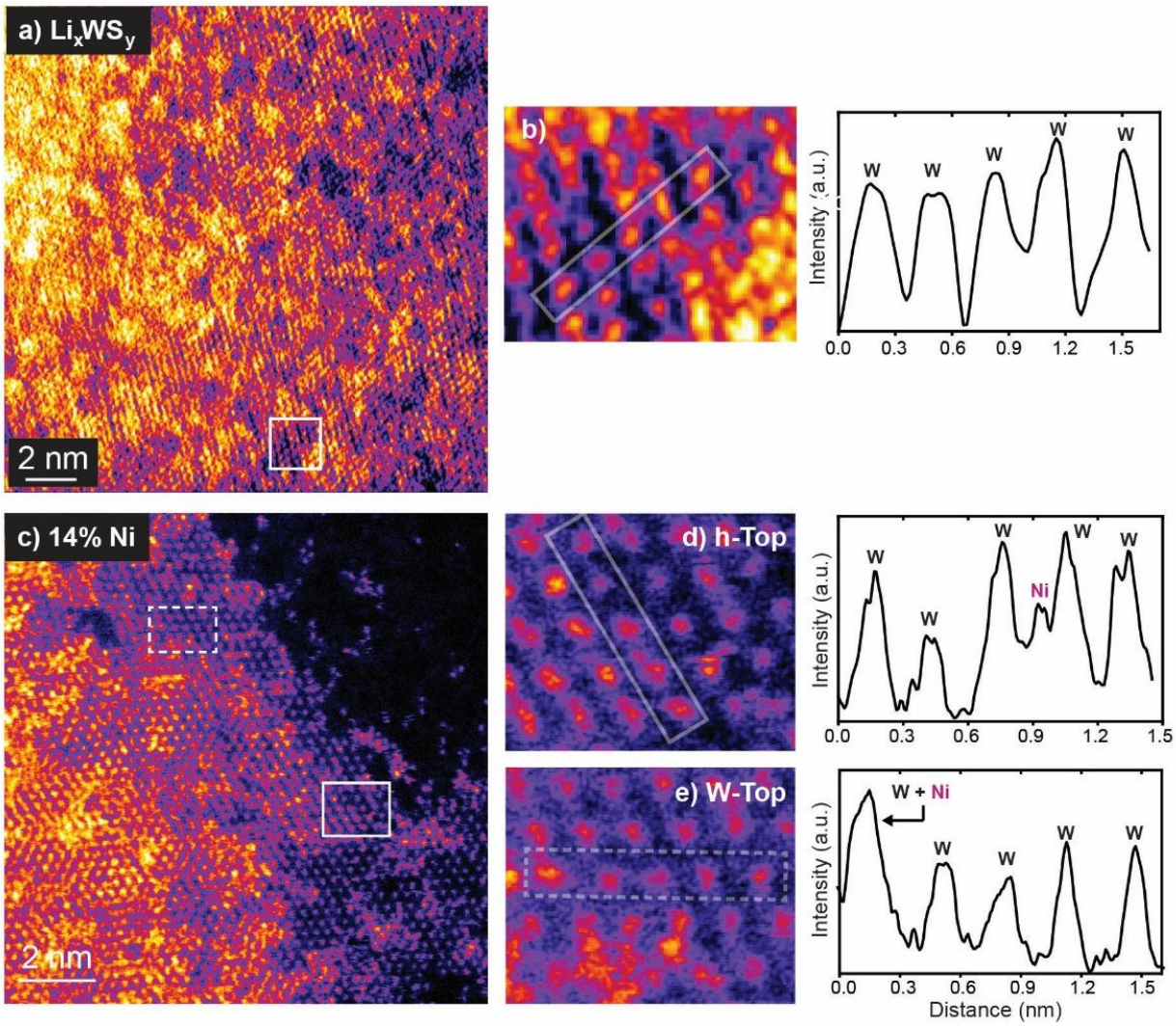

Figure 1.11. High-resolution STEM image of **(a)** Li_xWS_y with an enlarged region showing a **(b)** line intensity scan. High-resolution STEM image of **(c)** 14% Ni sample with enlarged regions and line intensity scans showing Ni single atom as an **(d)** interstitial atom (h-Top) and **(e)** on top of a W atom (W-Top).

Table 1.4. Zeta-potential measurements of as-synthesized WS_2, Li_xWS_2, and Ni-Li_xWS_y samples. Three measurements were made for selected samples to obtain an average and standard deviation.

Sample	**ζ (mV)**	**Std. Dev.**
WS_2	-2.02 (avg)	±0.1 mV
Li_xWS_y	-34.3 (avg)	±0.5 mV
9% Ni- Li_xWS_y	-32.7	--
11% Ni- Li_xWS_y	-32.4	--
14% Ni- Li_xWS_y	-30.5 (avg)	±0.8 mV
21% Ni- Li_xWS_y	-28.5	--
36% Ni- Li_xWS_y	-26.7	--
42% Ni- Li_xWS_y	-26.0	--
47% Ni- Li_xWS_y	-24.3 (avg)	±0.8 mV
61% Ni- Li_xWS_y	-23.6 (avg)	±0.3 mV

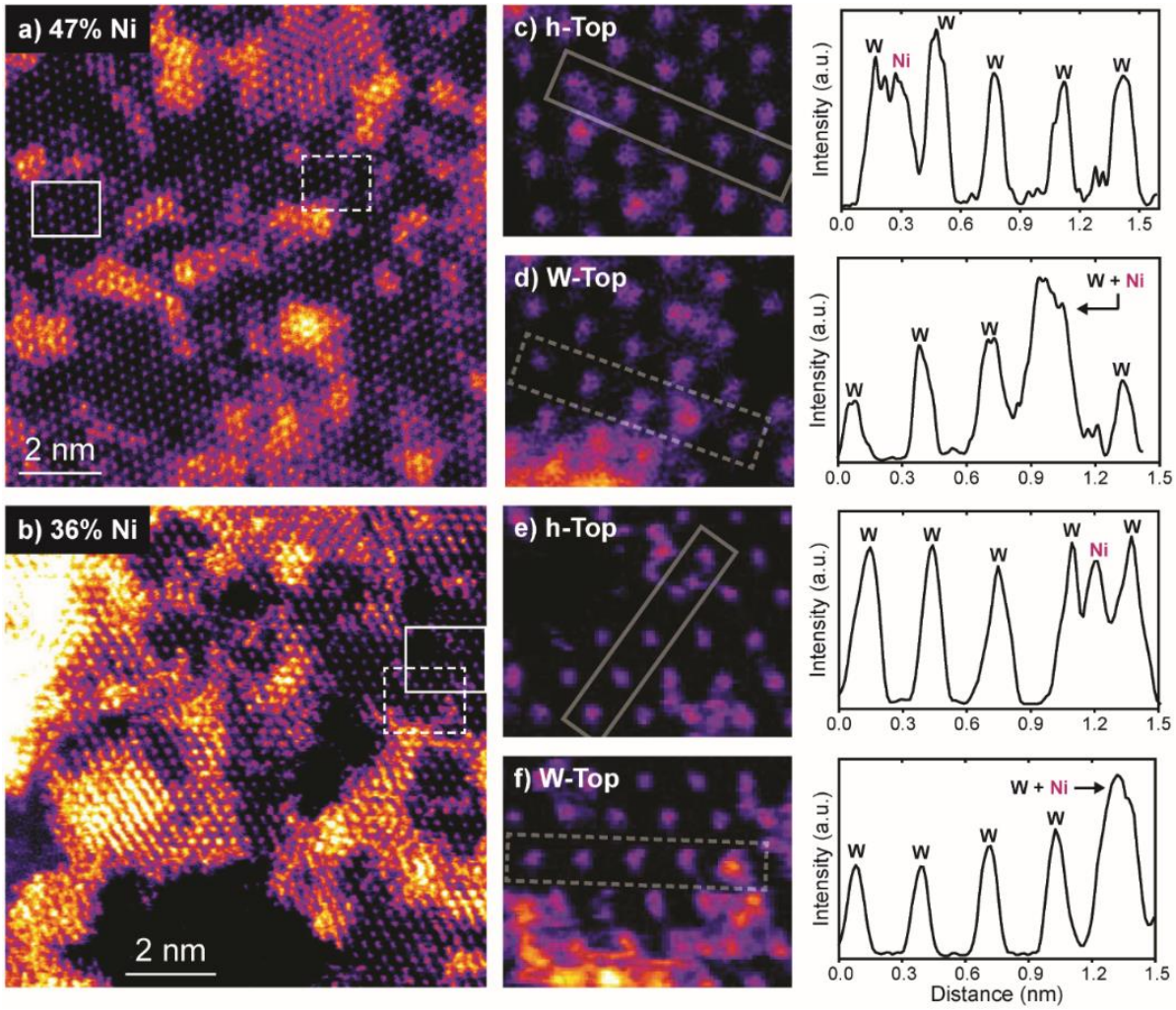

Figure 1.12. HR-STEM image of **(a)** 47% Ni-Li_xWS_y, and **(b)** 36% Ni-Li_xWS_y, **(c-f)** enlarged regions of the STEM images and intensity line scans for the boxed atoms illustrating different Ni single atom morphologies.

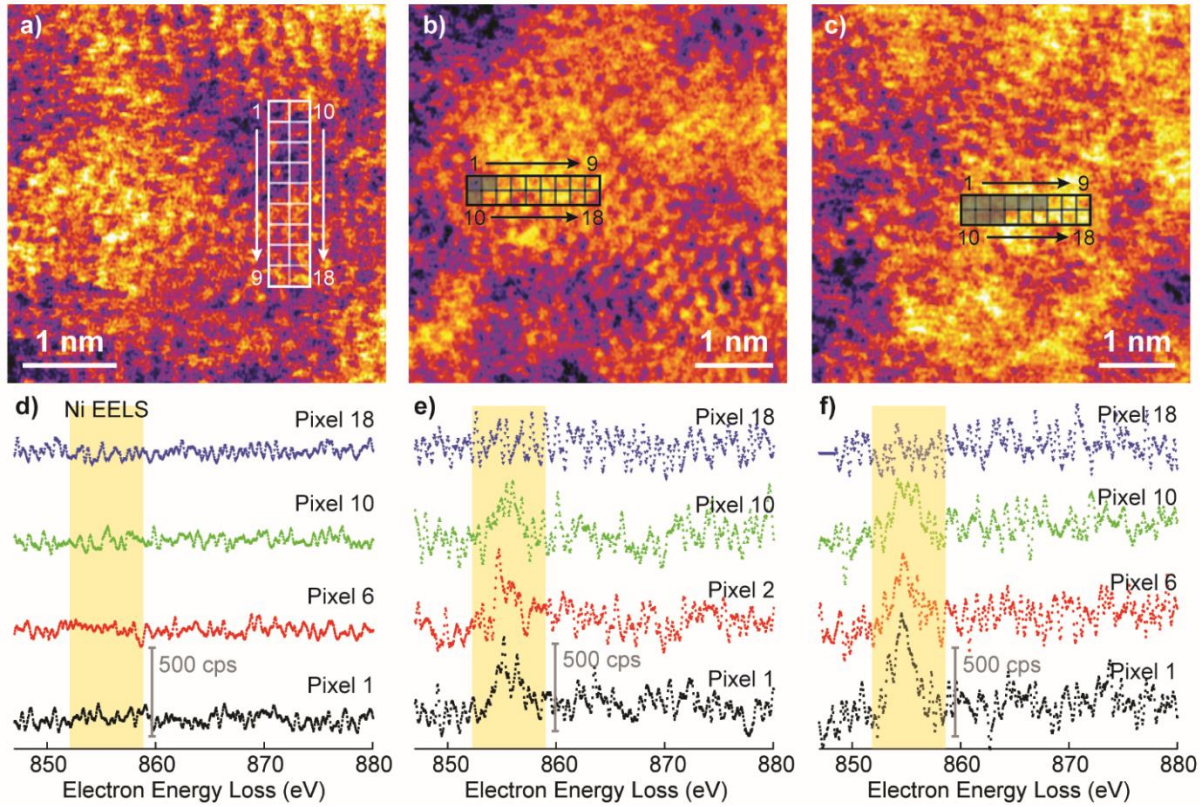

Figure 1.13. **(a-c)** HR-STEM images of 47% Ni-Li_xWS_y and the pixel grid where EELS mapping was obtained, **(d-f)** EELS spectra for individual pixels in each region.

Analyses of ADF Z-contrast for dopant identification are most reliable on defect-free single monolayer sheets because the contrast of the TMD sheet itself is extremely uniform. In our solution-processed nanosheets that contain defects and variable thickness, it is more difficult to definitively ascertain the location of Ni atoms simply through contrast analysis. As a result, we also performed electron energy loss spectroscopy (EELS) coupled to HR-STEM imaging. EELS mapping with 2 Å resolution confirms the presence of Ni atoms in a diversity of binding morphologies on the 47% Ni-Li_xWS_y sample. Three regions of the sample are shown in Figure 13a-c. In each region, EELS spectra were acquired from each of the eighteen pixels shown in the image, and only the pixels shaded in gray contain Ni (L-edge 855 eV). Representative EELS spectra acquired at individually numbered pixels in each region are provided in Figure 1.13d-f, and all of the remaining spectra are provided in Figure 1.14. In Figure 1.13a, a region where no Ni is observed, each pixel in the grid spans laterally across 0-2 W atoms on the WS_2 sheet, which would imply that single atoms of Ni bound in either h-Top or W-Top sites on the WS_2 sheet should be present *via* EELS mapping in a maximum of 3-4 square pixels. In Figure 1.13b, Ni is observed

in three pixels on the left-most edge of the mapped region, and the Ni EELS feature is extremely low in intensity in all three of those spectra (Figure 1.13b, 1.13e, 1.14a). In contrast, Figure 1.13c shows a region where both the Ni EELS intensity in a given pixel and the number of pixels where Ni is detected are both significantly higher (Figure 1.13c, 1.13f, 1.14b). In Figure 1.13c, each Ni-containing pixel has ~2-fold higher Ni concentration compared to Figure 1.13b based on the integrated area under the Ni EELS peak. Combined with the spatial extent of Ni detected in pixels 1-6 and 10-12, these data suggest that a significant agglomeration of Ni in the form of a multimetallic cluster is present on the surface of WS_2 in Figure 1.13c while a smaller Ni cluster or Ni single atom is present in Figure 1.13b. The clustering of Ni observed in this sample (47% Ni-Li_xWS_y) is likely due to the high atomic percentage of Ni present on the surface of WS_2, which, for our synthetic method, is the maximum Ni loading before obvious secondary nucleation of $Ni(OH)_2$ occurs. We anticipate that the relative proportion of isolated to clustered Ni atoms should be strongly dependent on the loading of Ni on the Li_xWS_y nanosheet.

Because HR-STEM coupled to EELS mapping is an inherently localized characterization technique and isolated atoms of Ni are extremely difficult to locate in more dilute Ni-Li_xWS_y samples, we turned to X-ray absorption spectroscopy to elucidate the average coordination environment and electronic structure of Ni atoms on the surface. The X-ray absorption near-edge structure (XANES) of the Ni K-edge clearly indicate that all Ni species adsorbed on WS_2 remain in the oxidized Ni^{2+} form. The white line intensities and edge energies for the 14% and 47% Ni-Li_xWS_y samples are close to that of the reference $Ni(OH)_2$ powder with slight shifts in E_0 toward lower energy (Figure 1.15a). These data indicate that there is a small perturbation in the electronic properties of the Ni species due to binding to the electron-rich WS_2 substrate, but the oxidation state remains essentially unchanged.[38,39] The XANES data for Ni foil is provided as a reference, which exhibits obviously lower edge energy and lower white line intensity compared to the doped Ni-Li_xWS_y samples.

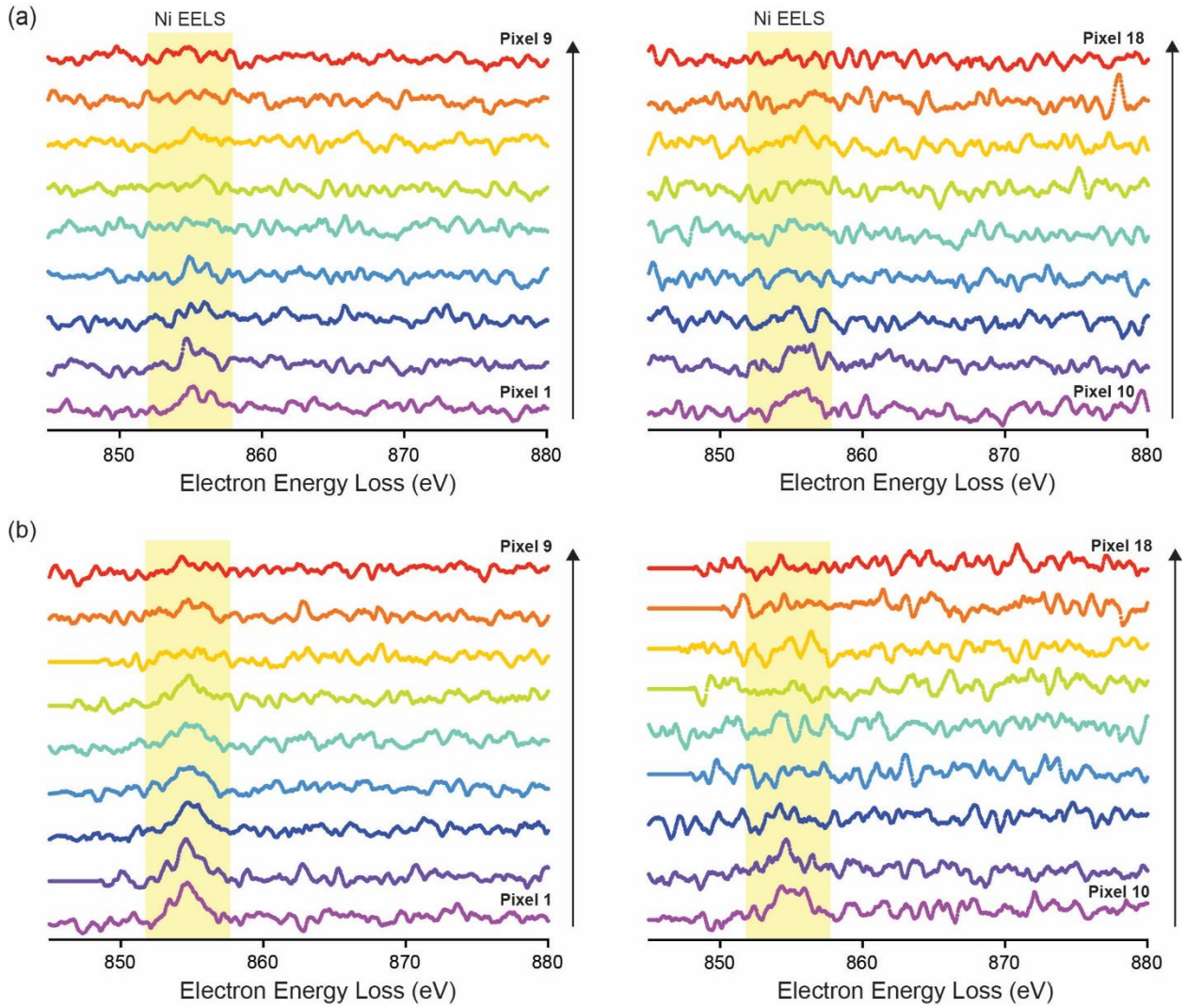

Figure 1.14. EELS spectra from the 47% Ni-Li_xWS_y sample for all pixels in **(a)** the region in Figure 1.12b and **(b)** the region in Figure 1.12c.

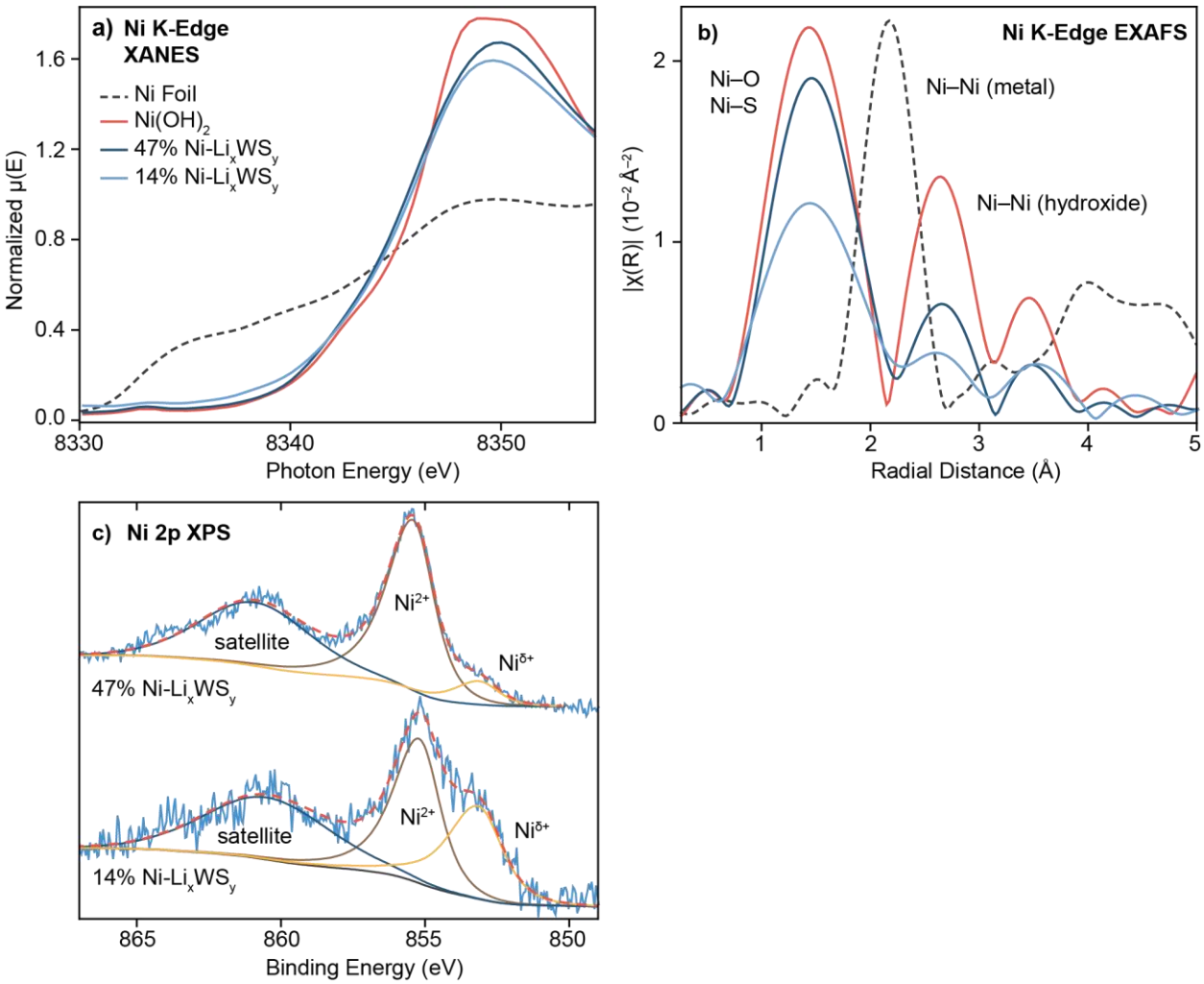

Figure 1.15. **(a)** XANES region, **(b)** EXAFS data in R-space, and **(c)** XPS of the Ni 2p region for 14% and 47% Ni-Li_xWS_y as well as Ni foil and $Ni(OH)_2$ control samples.

The extended X-ray absorption fine structure (EXAFS) provides more detailed information on the local coordination environment of Ni species on the surface of WS_2. On the three Ni-Li_xWS_y samples analyzed (14%, 36% and 47%), the first coordination shell is dominated by Ni–O scattering pathways with small contributions from Ni–S scattering, likely due to solvent coordination to the molecular Ni complex adsorbed onto the WS_2 surface (Figure 1.15b, 1.16, Table 1.5). Due to the isolated nature of adsorbed Ni species, the second coordination shell is relatively weak, which is markedly different from the strong Ni–Ni scattering present in the $Ni(OH)_2$ control. EXAFS data fitting reveal that 36% Ni-Li_xWS_y and 47% Ni-Li_xWS_y, high coverage samples in the plateau regime of Ni loading, have Ni–Ni coordination numbers (CN) of 2.6 and 3.1, respectively (Table 1.5). While still substantially lower than the expected Ni–Ni CN

of 6 in bulk $Ni(OH)_2$, these CN values corroborate the observation of Ni cluster formation in the EELS mapping for high Ni coverage samples. In contrast, at 14% Ni-Li_xWS_y, the Ni–Ni scattering peak is much lower in intensity (CN 1.5), suggesting that Ni atoms remain more isolated when the Ni loading is relatively low (Figure 1.15b).

X-ray photoelectron spectroscopy (XPS) also reveals a perturbation in the Ni electronic properties upon binding to the electron-rich WS_2 nanosheet. In the Ni 2p region, the primary Ni^{2+} peak at 855 eV is accompanied by an additional lower energy shoulder at 853 eV in all Ni-Li_xWS_y samples (Figure 1.15c). The lower binding energy is likely indicative of greater electron density due to binding to the electron-rich sulfur ligands on the surface and partial electron transfer from the WS_2 nanosheet.[40,41] The proportion of electron-rich Ni is higher in the sample with the lower Ni coverage and decreases as the Ni coverage on the surface increases.

Importantly, the synthetic process was found to be highly reproducible based on elemental analysis and electrochemical characterization of three independent preparations of Ni-Li_xWS_y at 0.2 eq. and 2 eq. $NiCl_2$ added in solution (Table 1.6, 1.7).

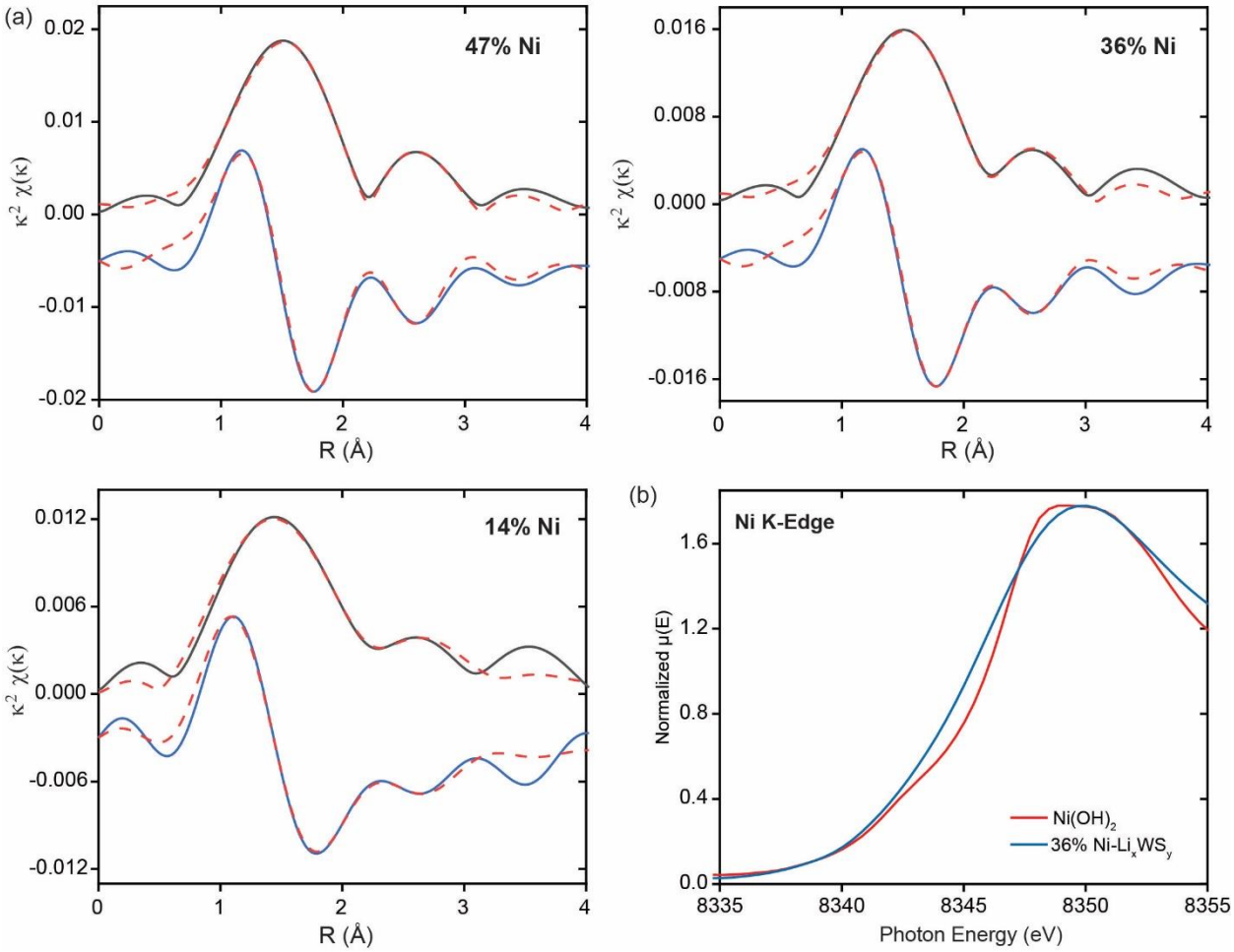

Figure 1.16. **(a)** EXAFS fits (dotted) overlaid with experimental data (solid) for the first and second coordination sphere (0.6–3.2 Å) in R-space for three Ni-Li_xWS_y samples. **(b)** XANES region for the 36% Ni-Li_xWS_y sample. The XANES region for the 14% and 47% Ni-Li_xWS_y samples are provided in the main text.

Table 1.5. Summary of EXAFS best fit parameters for the Ni K edge on a $Ni(OH)_2$ sample and three representative Ni-Li_xWS_y samples. Ni foil was used a reference.

Sample	**XANES Energy (KeV)**	**XANES Pre-edge Energy (KeV)**	**Scattering Pair**	**CN**	**R (Å)**	**$\Delta\sigma^2$(Å)^2**	**E_o (eV)**	**Res. %**
Ni Foil (Ref)	8.3328	---	Ni-Ni	12	2.492	---	---	---
$Ni(OH)_2$	8.3469	8.332	Ni-O	6.3	2.069	0.001	0.63	---
			Ni-Ni	6.3	3.114	0.001	-0.99	
47% Ni	8.3459	8.333	Ni-O	5.1	2.089	0.001	2.47	5.6%
			Ni-S	0.55	2.369	0.001	-6.18	
			Ni-Ni	3.2	3.019	0.003	-3.02	
36% Ni	8.3460	8.333	Ni-O	4.2	2.078	0.001	2.31	5.2%
			Ni-S	0.83	2.398	0.001	-5.28	
			Ni-Ni	2.7	2.953	0.003	-5.57	
14% Ni	8.3463	8.333	Ni-O	4.6	2.112	0.001	4.37	3.8%
			Ni-S	0.96	2.212	0.001	13.7	
			Ni-Ni	1.5	3.098	0.003	-3.62	

Table 1.6. Electrochemical reproducibility studies on representative Ni-Li_xWS_y samples showing reproducible Ni(II/III) redox behavior and Ni RF. Averages and standard deviations are obtained from three separate electrochemical experiments for each sample.

Sample	**Ni Red. E (V vs. RHE)**	**Avg. E_{NiRed} (V vs. RHE)**	**Ni Red. Area ($\mu C/cm^2$)**	**Ni RF**	**Avg. Ni RF**
11% Ni	1.44	1.44 ± 0.003	133	0.54	0.56 ± 0.06
	1.44		122	0.50	
	1.43		157	0.64	
14% Ni	1.44	1.45 ± 0.001	183	0.74	0.77 ± 0.03
	1.45		187	0.76	
	1.44		200	0.81	
47% Ni	1.43	1.43 ± 0.003	1140	4.65	4.85 ± 0.3
	1.43		1130	4.57	
	1.43		1310	5.34	

Table 1.7. Synthetic reproducibility studies. Elemental analysis for four independent preparations of Ni-Li_xWS_y for a fixed 0.2 eq $NiCl_2$ added in solution.

	Ratios W : Ni at.%
0.2 eq Ni-Li_xWS_y Batch #1	93 : 7 (XPS)
0.2 eq Ni-Li_xWS_y Batch #2	94 : 6 (XPS)
0.2 eq Ni-Li_xWS_y Batch #3	93 : 7 (EDS)
0.2 eq Ni-Li_xWS_y Batch #4	93 : 7 (EDS)

1.4.1 Electrochemical Reactivity

Numerous examples from the literature featuring composite materials comprising Ni-containing nanoparticles and metal chalcogenide nanosheets have been shown to exhibit enhanced hydrogen evolution or oxygen evolution reactivity, due in part perhaps to an electronic perturbation of Ni centers in close contact with the metal chalcogenide.[42-48] Based on the microscopic and spectroscopic characterization of our Ni-Li_xWS_y samples, we hypothesized that

the relatively isolated Ni^{2+} ions bound to the electron-rich WS_2 nanosheet would exhibit very different redox properties from bulk nickel sulfide or nickel hydroxide materials. All samples used for electrochemical comparison were synthesized based on literature reports and tested under identical electrochemical conditions to Ni-Li_xWS_y (Figure 1.17-1.20).

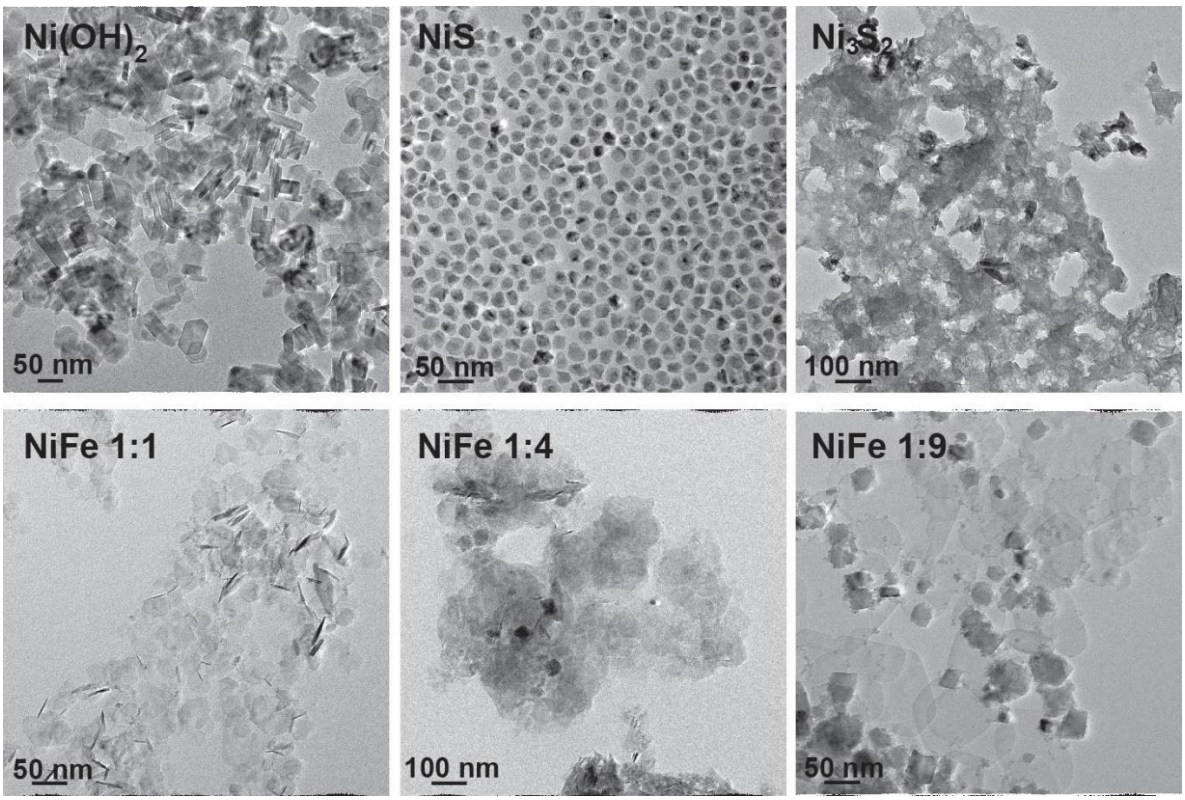

Figure 1.17. TEM images of Ni-containing control samples: $Ni(OH)_2$ sheets, NiS nanoparticles, Ni_3S_2 films, and NiFe LDHs.

We used electrochemistry in 0.1 M KOH to probe the redox and catalytic properties of Ni^{2+} atoms in Ni-Li_xWS_y. In all cases, a large oxidation feature is observed in the first two CV scans corresponding to partial oxidation of the WS_2 nanosheet itself (Figure 1.21). Thereafter, the Ni(II/III) redox feature between 1.4 V and 1.6 V vs. RHE appears, grows steadily in area for the next 30-40 scans, and remains stable thereafter (Figure 1.22, 1.23a). The cathodic peak position at both the 4th and 75th CV scan as well as the peak center at the 75th CV for the Ni(II/III) redox couple are plotted as a function of %Ni loading on WS_2 along with NiS, Ni_3S_2, and $Ni(OH)_2$ control samples (Figure 1.23b). The trend in Ni(II/III) redox potential is consistent regardless of the number of CV scans performed. All of the Ni-Li_xWS_y samples exhibit a significant positive shift

in Ni peak position of 80-140 mV relative to the $Ni(OH)_2$ control. The observed Ni(II/III) peak centers ($E_{1/2}$) fall between 1.48 and 1.51 V vs. RHE, which is relatively similar to the $E_{1/2}$ of 20 nm NiS nanoparticles, suggesting that the adsorbed Ni^{2+} species are bound to sulfides on the Li_xWS_y surface. Intriguingly, the positive shift in redox potential observed here is similar in magnitude to that of one of the most active Ni-based oxygen evolution catalysts, Ni-Fe layered double hydroxides (LDH) (Figure 1.20).[49-54] In the Ni-Fe LDHs, the redox potential shift due to Fe doping accelerates the key O–O bond forming step in water oxidation, and a significant amount of Fe doping is required in order to shift the overall band structure of $Ni(OH)_2$ to the optimal energy for water oxidation.[55-57] Here, every Ni atom up to the maximum loading of 47% Ni-Li_xWS_y is directly bound to sulfides on the WS_2 surface and experiences the strong positive shift in redox potential.

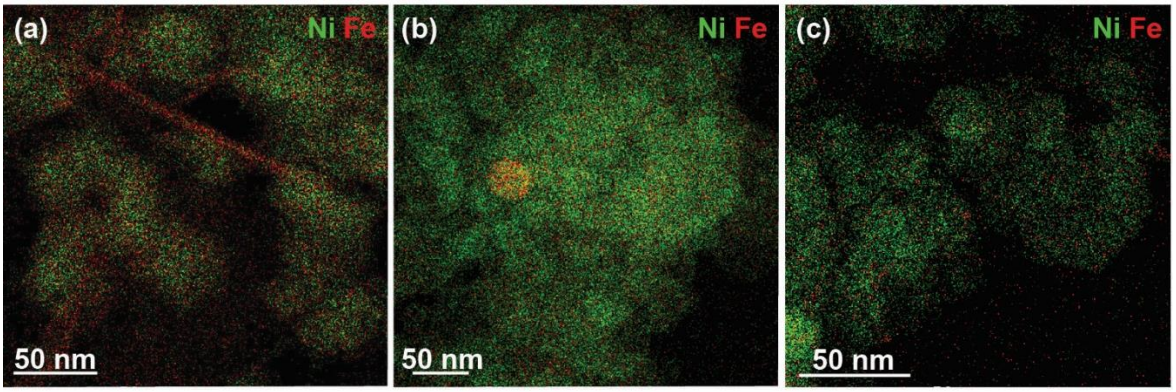

Figure 1.18. EDS elemental mapping on NiFe LDH samples. **(a)** NiFe 1:1, **(b)** NiFe 1:4, and **(c)** NiFe 1:9.

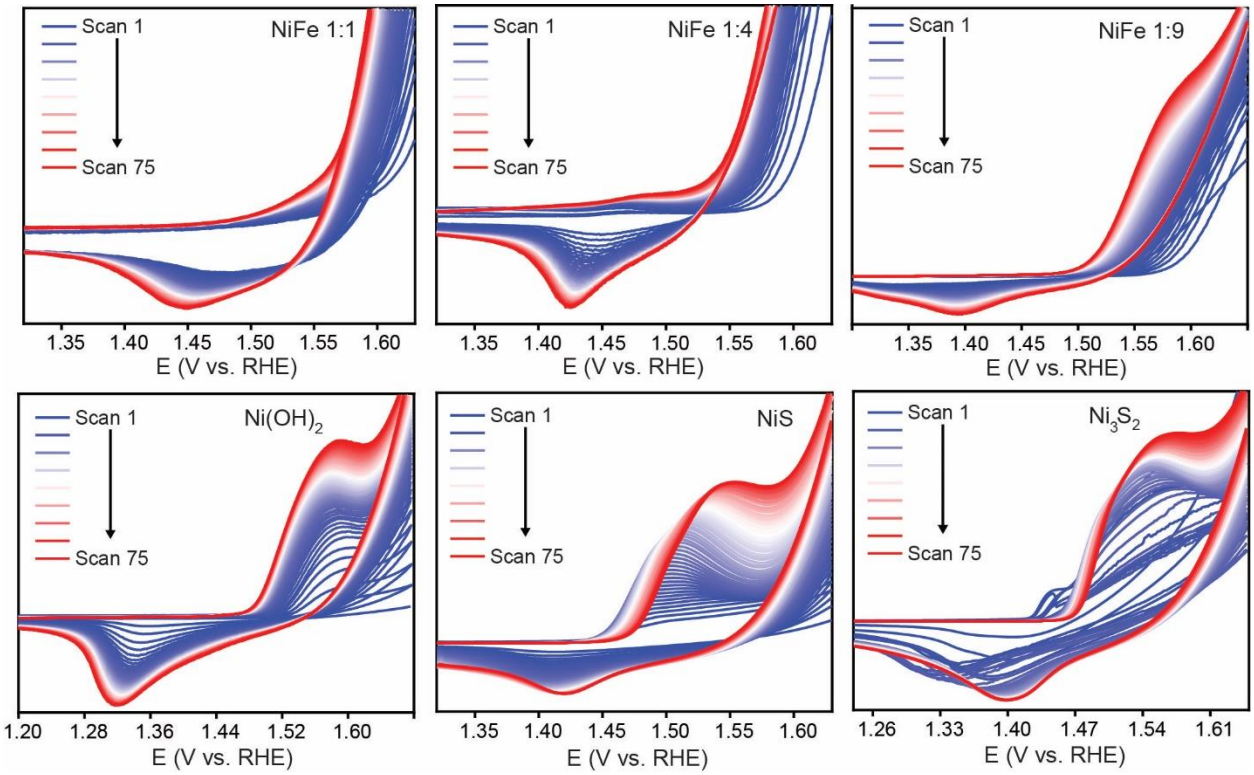

Figure 1.19. Evolution of the Ni(II/III) redox features during 75 CV scans in 0.1 M KOH at 100 mV s^{-1} for all Ni-containing control samples: $Ni(OH)_2$ sheets, NiS nanoparticles, Ni_3S_2 films, and NiFe LDHs.

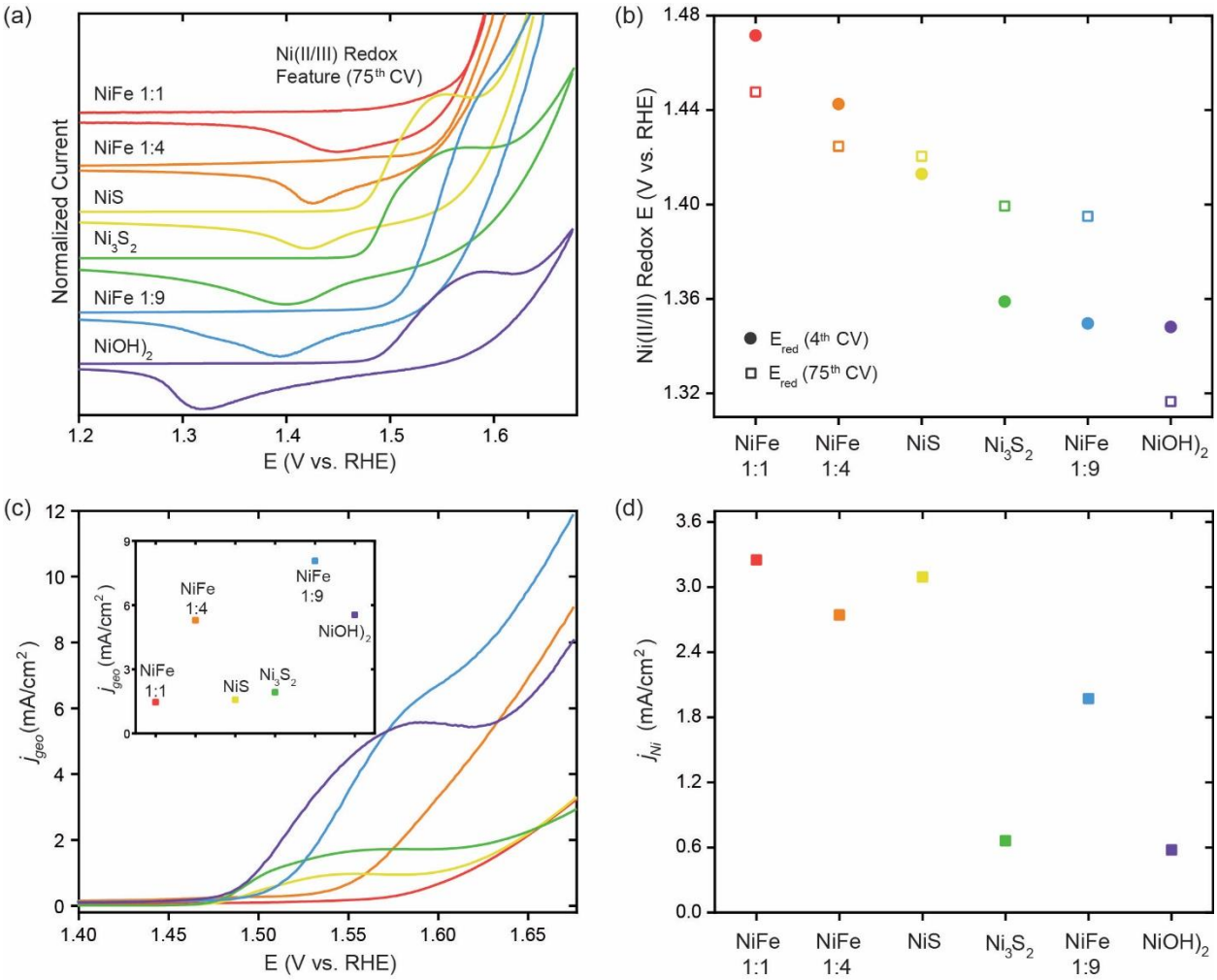

Figure 1.20. Electrochemical data all Ni control samples: NiFe LDHs, NiS, Ni_3S_2, and $Ni(OH)_2$. **(a)** CV of the Ni(II/III) redox feature in the 75th scan, **(b)** Ni(II/III) reduction potential in the 4th and 75th CV, **(c)** geometric OER current density vs. potential for the 4th scan, **(inset)** geometric OER current density at 1.63 V, **(d)** Ni-normalized OER current density at 1.63 V.

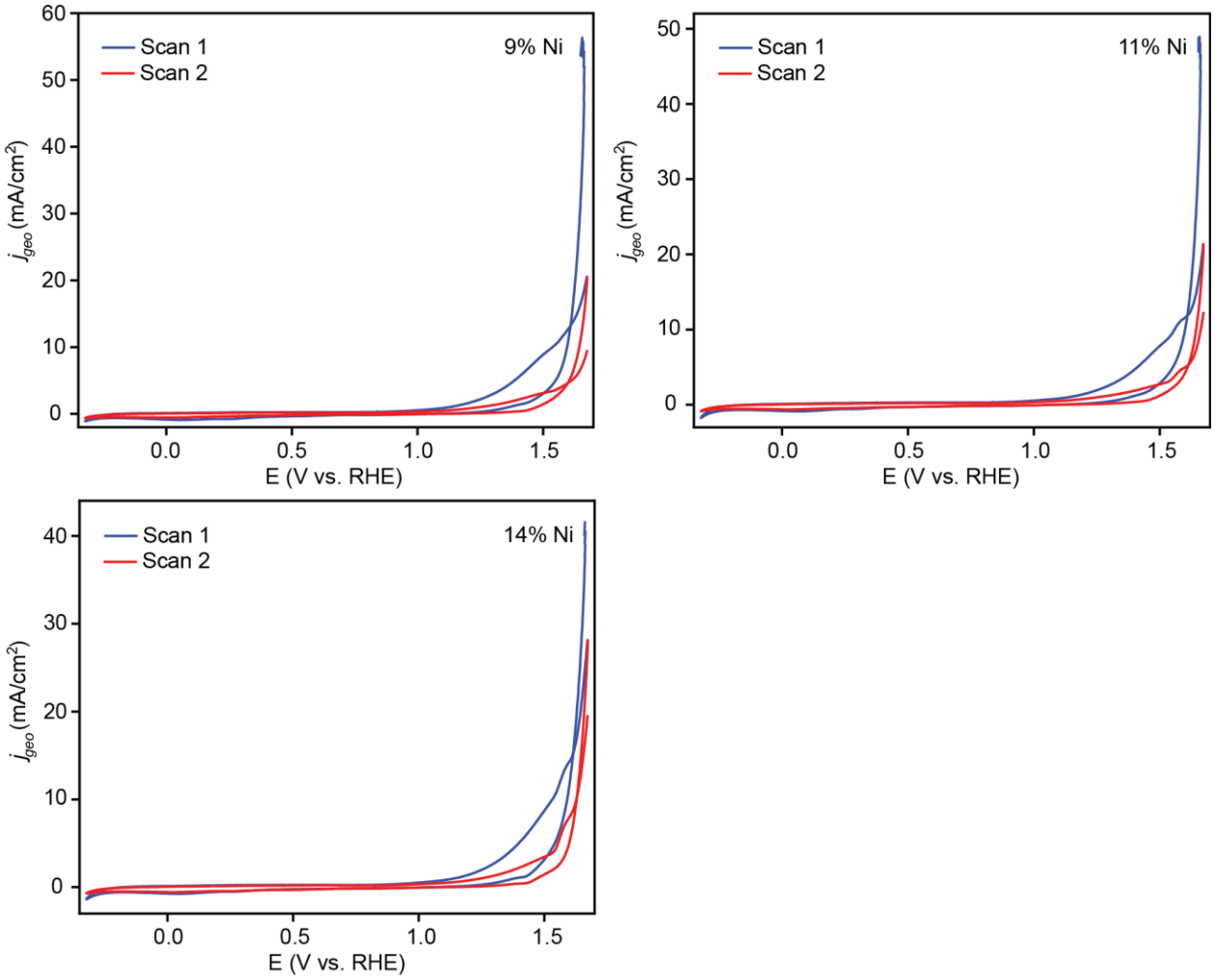

Figure 1.21. Electrochemical data showing the oxidation of WS_2 in the 1st and 2nd CV scans on selected Ni-Li_xWS_y samples.

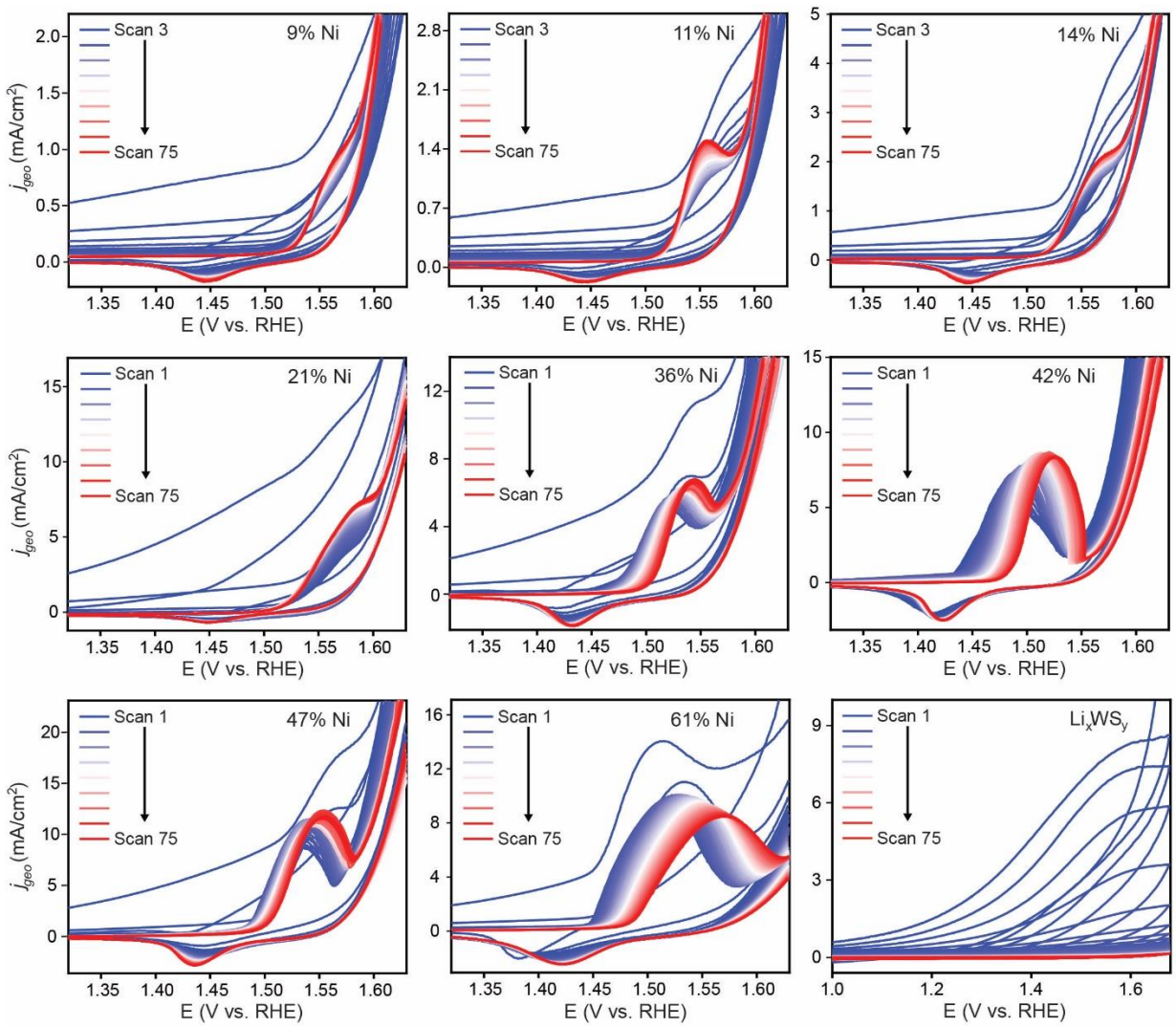

Figure 1.22. Evolution of the Ni(II/III) redox features over 75 CV scans in 0.1 M KOH at 100 mV s^{-1}. As a comparison, Li_xWS_y over the same scanning conditions is provided.

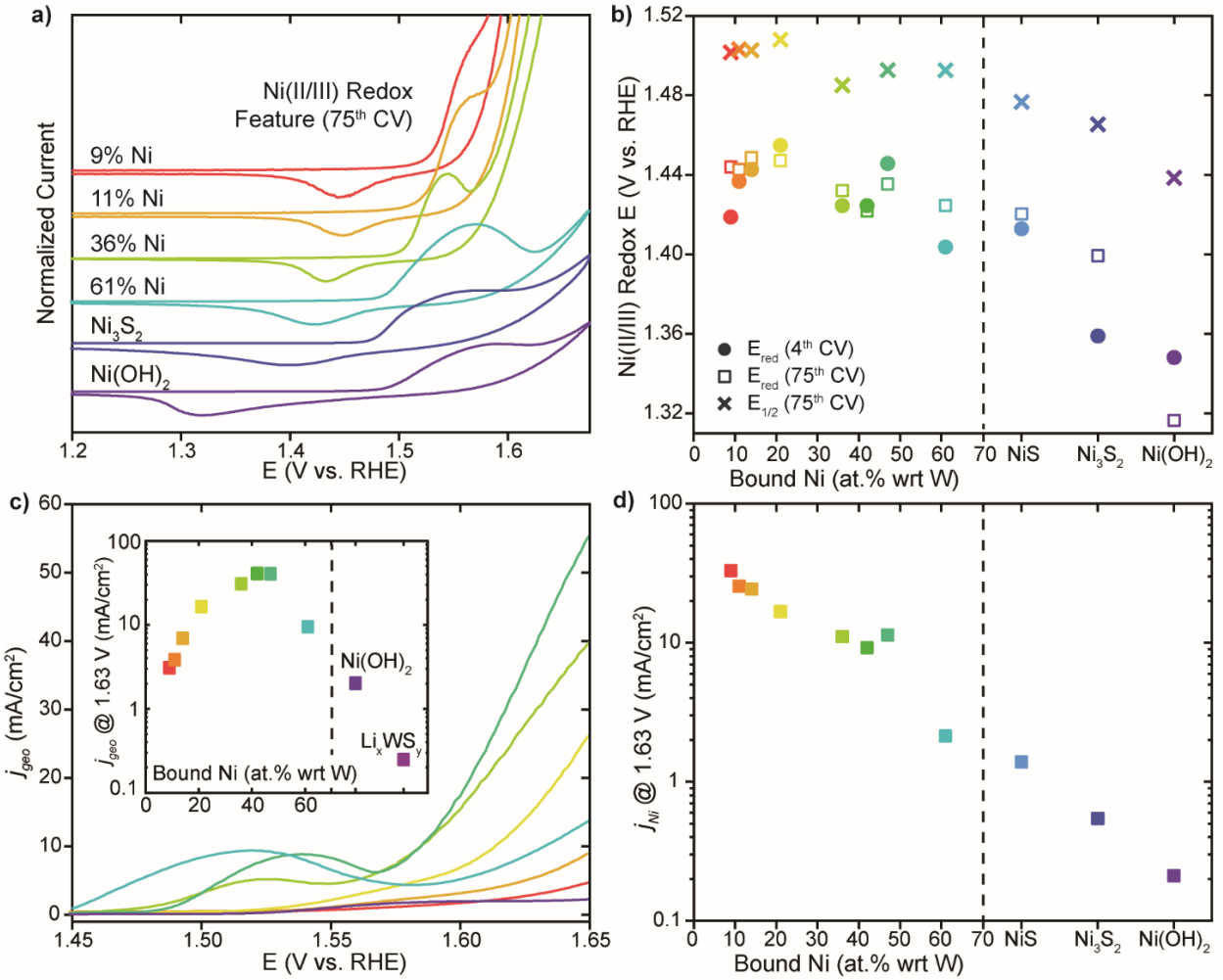

Figure 1.23. Electrochemical data for Ni-Li_xWS_y and various Ni control samples. **(a)** CV of the Ni(II/III) redox feature in the 75th scan, **(b)** Ni(II/III) redox potential as a function of Ni loading, **(c)** geometric OER current density vs. potential for the 4th scan, **(inset)** geometric OER current density at 1.63 V as a function of Ni loading, **(d)** Ni-normalized OER current density at 1.63 V as a function of Ni loading.

While the Ni(II/III) redox potentials stay relatively constant regardless of Ni loading on Li_xWS_y, we observe a clear correlation between the current density for oxygen evolution at 1.63 V vs. RHE and the Ni^{2+} loading on the WS_2 surface. In all cases, OER current density is reported in the 4th CV scan to best represent the activity of the as-synthesized Ni-Li_xWS_y sample. The geometric current density for OER increases with Ni loading up to the plateau loading of ~40% simply due to an increase in the number of accessible active sites for OER catalysis (Figure 1.23c). However, the OER activity begins to drop once secondary nucleation of $Ni(OH)_2$ occurs on the sample at 61% Ni-Li_xWS_y. Pure $Ni(OH)_2$ and undoped Li_xWS_y exhibit 20-fold and 200-fold lower

OER geometric current density, respectively, than the most active Ni-Li_xWS_y sample. All of the Ni-Li_xWS_y samples show very similar Tafel slopes for OER, ranging from 51 to 72 mV/dec, which are entirely consistent with Ni-catalyzed reactivity (Figure 1.24).[55] Together, these data suggest that the high dispersion of catalytically active Ni sites on the WS_2 nanosheet are critically important toward achieving high OER catalytic activity. In order to deconvolute the inherent activity per Ni site from the number of active sites available on the surface, we also normalize the OER activity by the electrochemical surface area for Ni, represented by the integrated charge within the Ni(II/III) reduction feature (Table 1.7). We observe that the samples with the lowest loading of Ni^{2+} have the highest intrinsic catalytic activity, likely due to the geometric isolation of Ni^{2+} sites on the surface of the WS_2 nanosheet (Figure 1.25d). As the Ni loading increases, Ni single atoms begin to aggregate into small clusters as observed in the STEM-EELS mapping and EXAFS data, thus reducing the intrinsic activity per Ni site.

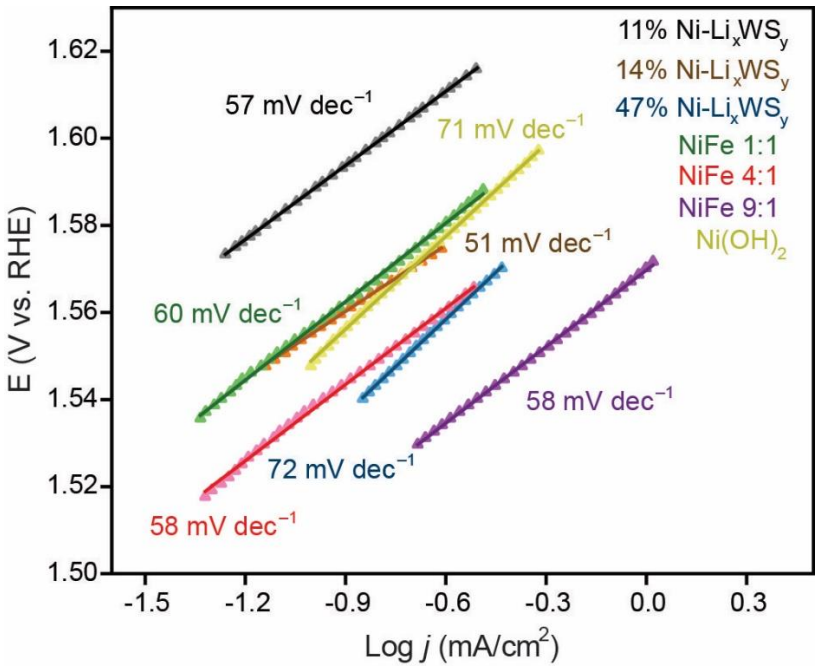

Figure 1.24. Tafel plots for 11%, 14% and 47% Ni-Li_xWS_y samples in comparison with NiFe LDHs and $Ni(OH)_2$ control samples at a scan rate of 1 mV s^{-1} in 0.1 M KOH.

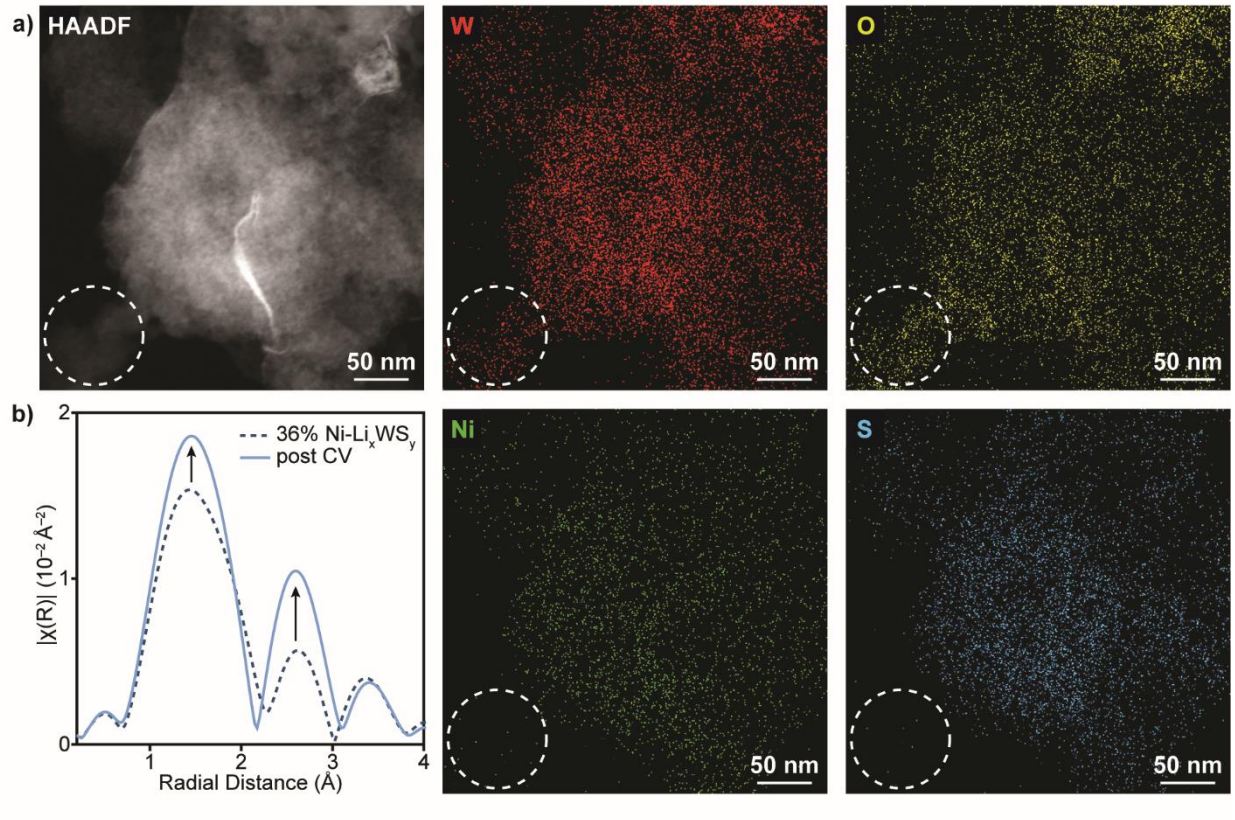

Figure 1.25. **(a)** HAADF-STEM image and EDS mapping of W, O, Ni, and S distribution for 36% Ni-Li_xWS_y after 75 CV scans under OER conditions. **(b)** Change in the EXAFS spectrum before and after CV cycling.

While the redox behavior and OER activity of Ni dopants on the as-synthesized Ni-Li_xWS_y sheets are clearly modified relative to bulk $Ni(OH)_2$, the electrochemical progression during CV cycling suggests that the structure evolves during OER catalysis (Figure 1.22). To understand the structural evolution of Ni-doped Li_xWS_y, we also characterized the sample using STEM-EDS mapping and XAS after 75 CV scans under OER conditions. Based on STEM-EDS data, the Ni dopants remain evenly distributed across the WS_2 nanosheets despite the fact that the WS_2 support itself has begun to decompose (Figure 1.25a, 1.26, 1.27). Most of the material degradation occurs due to oxidation of the WS_2 sheets themselves under the basic and oxidizing OER conditions, including dissolution of WO_4^{3-} and formation of WO_3 nanoparticles as shown in the circled region in Figure 25a. The Ni K-edge XANES data changes relatively little during electrochemical cycling, but the EXAFS scattering pathway at 2.5 Å that corresponds to Ni–Ni scattering in $Ni(OH)_2$ grows significantly in the 36% and 47% Ni-Li_xWS_y samples from CN 2.5–3 to CN 4.5–5 (Figure 1.25b, Table 1.9). In extended CV cycling tests up to 1000 scans on the 47% and 14% Ni-Li_xWS_y samples,

the geometric current density for OER declines by ~20% after an initial increase over the first 100 scans, likely due to aggregation in catalytically active Ni species. However, the activity retention for Ni-Li_xWS_y samples remains better than a pure $Ni(OH)_2$ sample, which declines by over 70% under the same cycling conditions (Figure 1.28-1.29). While these Ni-Li_xWS_y materials may not be practical OER catalysts due to their instability over extended cycling, we anticipate that the highly tunable and reproducible synthetic method demonstrated herein will have broad relevance toward introducing other first-row transition metal single atoms with catalytic, magnetic, or optical importance onto the versatile electronic platform of transition metal dichalcogenide nanomaterials.

Table 1.8. Summary of Ni reduction peak area and roughness factors after 4 and 75 CV scans in 0.1 M KOH at a scan rate of 100 mV s^{-1} for all Ni-Li_xWS_y samples as well as the control samples NiFe layered double hydroxides (LDH), $Ni(OH)_2$, NiS, and Ni_3S_2.

Sample	**Scan 4**		**Scan 75**	
	Ni Red Area ($\mu C/cm^2$)	**Ni RF**	**Ni Red Area ($\mu C/cm^2$)**	**Ni RF**
9% Ni	23	0.09	95	0.39
11% Ni	37	0.15	133	0.54
14% Ni	70	0.28	183	0.74
21% Ni	242	0.98	277	1.13
36% Ni	686	2.79	764	3.10
42% Ni	1090	4.44	928	3.77
47% Ni	881	3.58	1140	4.65
61% Ni	1090	4.45	1690	6.89
NiFe 1:1	55	0.22	111	0.45
NiFe 4:1	108	0.44	474	1.93
NiFe 9:1	357	1.45	1010	4.09
$Ni(OH)_2$	2360	9.60	2360	9.60
NiS	85	0.34	125	0.51
Ni_3S_2	579	2.35	717	2.91

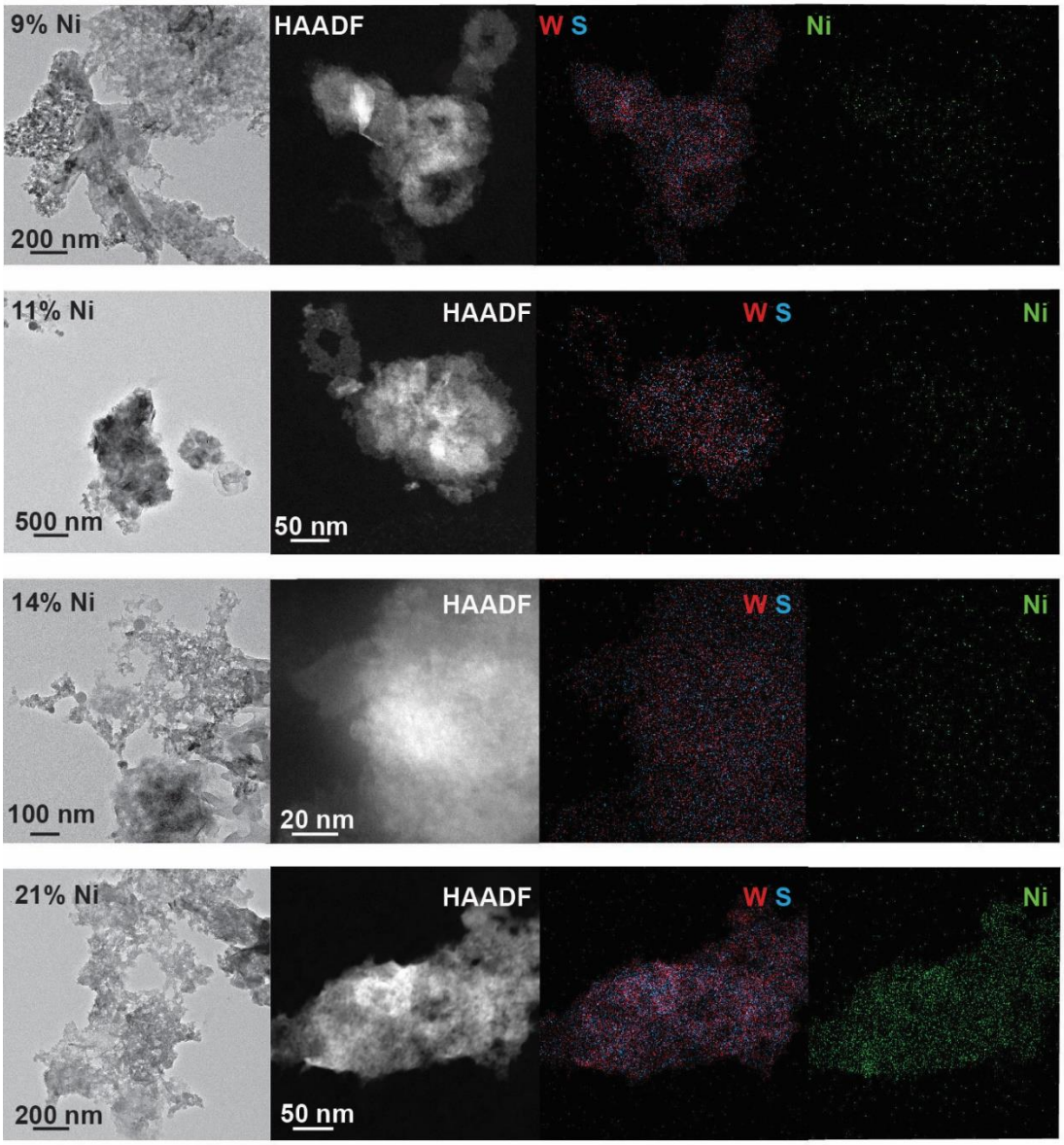

Figure 1.26. TEM, HAADF-STEM and EDS elemental mapping of 9% to 21% Ni-Li_xWS_y samples after 75 CV scans under OER conditions.

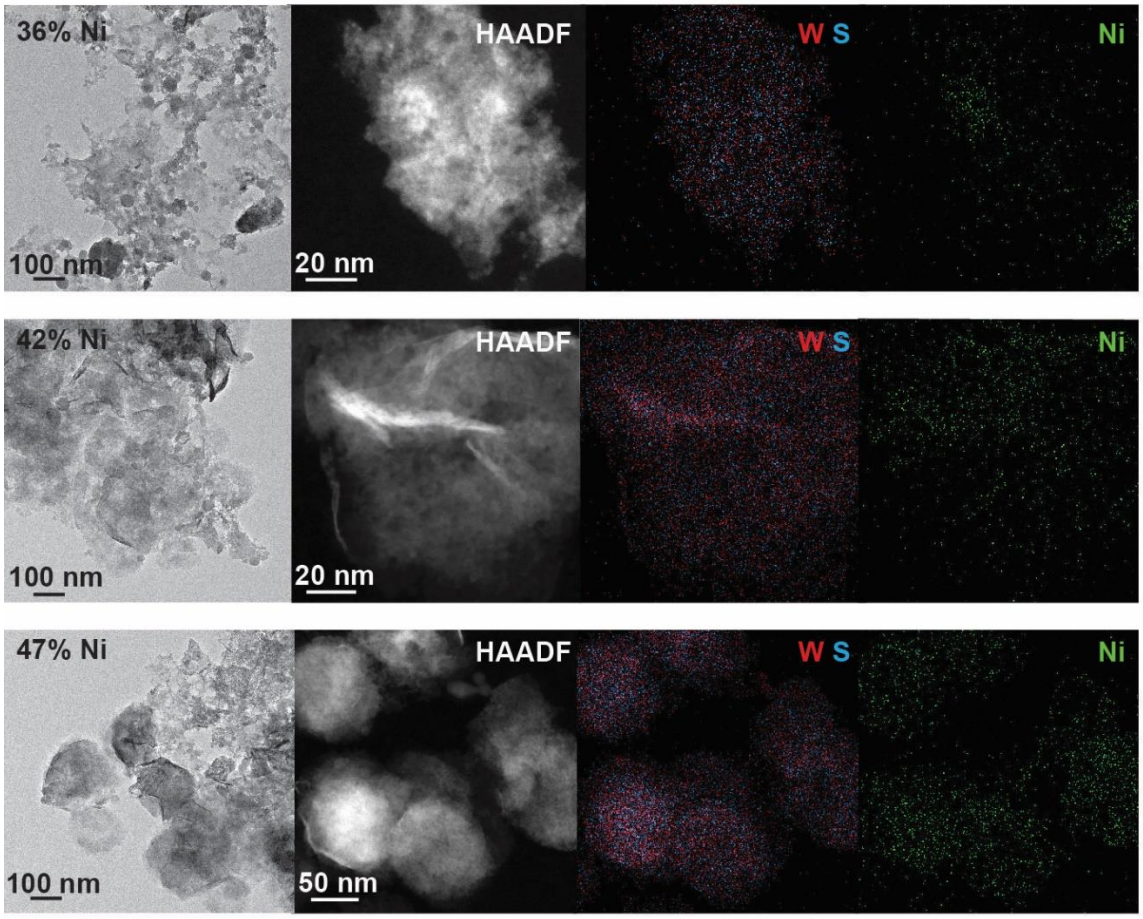

Figure 1.27. TEM, HAADF-STEM and EDS elemental mapping of 36% to 47% Ni-Li_xWS_y samples after 75 CV scans under OER conditions. Figure is continued on top of next page.

Table 1.9. Ni K edge EXAFS best fit parameters after 75 CV scans under OER conditions for 47% and 36% Ni-Li_xWS_y. The 14% Ni-Li_xWS_y sample had insufficient data quality to perform EXAFS fitting.

Sample	**XANES Energy (KeV)**	**XANES Energy (KeV) pre-edge**	**Scattering Pair**	**CN**	**R (Å)**	**$\Delta\sigma^2$(Å)^2**	**E_0 (eV)**	**Res. %**
Ni Foil	8.3328	---	Ni-Ni	12	2.492	0.000	---	---
$Ni(OH)_2$	8.3469	8.332	Ni-O	6.3	2.069	0.001	0.63	---
			Ni-Ni	6.3	3.114	0.001	-0.99	
47% Ni	8.3461	8.332	Ni-O	5.2	2.109	0.001	2.20	6.62%
			Ni-S	0.67	2.213	0.001	-0.78	
			Ni-Ni	4.9	3.109	0.003	1.35	
36% Ni	8.3462	8.333	Ni-O	5.1	2.106	0.001	1.92	6.73%
			Ni-S	0.83	2.221	0.001	-6.38	
			Ni-Ni	4.6	3.104	0.003	1.26	

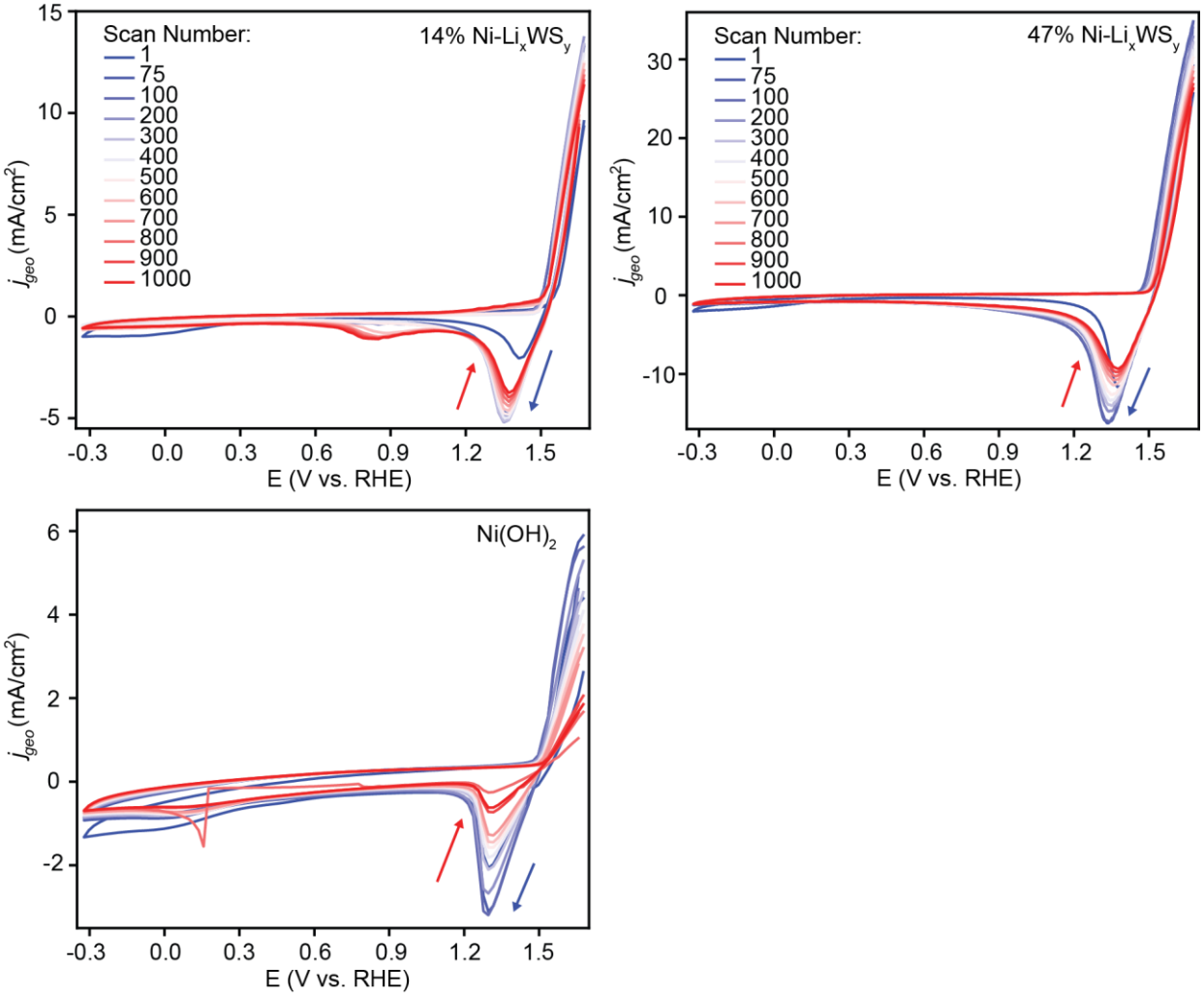

Figure 1.28. Stability test over 1000 OER cycles at a scan rate of 300 mV s^{-1} for the 14% and 47% Ni-Li_xWS_y samples and $Ni(OH)_2$ as control.

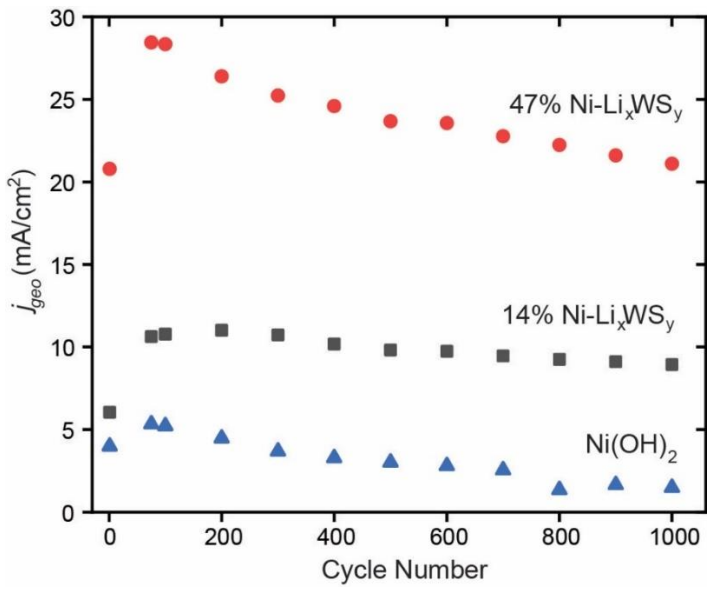

Figure 1.29. OER activity at 1.63 V vs. RHE as a function of cycle number for the 14% and 47% Ni-Li_xWS_y samples and $Ni(OH)_2$ as control.

1.5 Conclusions

We have developed a solution-phase synthetic method to activate colloidal WS_2 nanosheets using n-BuLi and introduce surface-adsorbed Ni species ranging in coverage from 9% to 47% Ni with respect to W. Atomic resolution STEM imaging coupled to EELS mapping on two high coverage Ni-Li_xWS_y samples show that both isolated Ni atoms and Ni multimetallic clusters coexist on the surface. In tandem with X-ray absorption spectroscopy, these data indicate that Ni species adsorb primarily as single atoms in the low coverage regime and as a mixture of single atoms and clusters in the high coverage regime. The electronic properties of the Ni atoms are significantly perturbed through adsorption to WS_2 as evidenced by an electron-rich Ni feature in the XPS and positively shifted Ni(II/III) redox potential relative to a $Ni(OH)_2$ control sample. Both the electronic perturbations and the speciation of Ni sites as isolated atoms play a role in enhancing the intrinsic catalytic activity of Ni-Li_xWS_y samples for the oxygen evolution reaction. We anticipate that the single atom functionalization strategy demonstrated in this work, activation of free sulfide sites on the basal plane followed by transition metal coordination, will be broadly applicable for first-row transition metals and provide a general route to introduce additional optoelectronic and catalytic functionality into TMD nanomaterials.

1.6 Experimental Methods

1.6.1 Materials

Tungsten(VI) chloride (99.9+%, trace metal basis), sulfur (99.999%, trace metal basis), and nickel acetylacetonate (96%) were purchased from ACROS Organics. Nickel(II) chloride anhydrous (98% purity), nickel(II) nitrate hexahydrate (98%), iron(III) nitrate nonahydrate (ACS, 98.0-101.0%) and anhydrous n-hexanes were purchased from Alfa Aesar. Carbon disulfide (Spectranalyzed™), hexanes (certified ACS) and 2-propanol (certified ACS plus) were purchased from Fisher Scientific. Carbon black (Vulcan XC 72R) was purchased from FuelCellStore. Oleylamine (technical grade, 70%), oleic acid (technical grade, 90%), N-methylformamide (99%), 5 wt.% Nafion solution, n-butyllithium solution (1.6 M in hexanes), cysteamine hydrochloride (≥98%), and 1,5-pentanediol (≥97.0%) were purchased from Sigma-Aldrich. Triethylamine (99.5% min) was purchased from Thomas Scientific. Ethanol (200 proof) was purchased from Decon Labs, Inc. Fluorine-doped tin oxide (FTO) electrodes (TEC 7, R: 6-8 Ω/sq) were purchased from MTI Corporation. All chemicals were used without further purification. Electrolyte solutions were prepared from Nanopure water (ASTM Type I, 18.2 MΩ), purified using a Thermo Scientific Barnstead Ultrapure Water System.

1.6.2 Synthesis of 1T-WS_2 nanosheets

The synthesis of 100 nm 1T-WS_2 nanosheets is based upon a literature procedure.1 A 3-neck round bottom flask is charged with 15 mL of oleylamine (OAm), which is degassed under vacuum at 65 ˚C for 1 hour and then heated to 320 °C under inert atmosphere. Separately, WCl_6 (50 mg, 0.125 mmol) is suspended in 300 µL of oleic acid (OA), and the suspension is sonicated until fully dissolved. The vial is purged with N_2, and CS_2 (240 µL, 3.97 mmol) and OAm (5 mL) are added. This W and S precursor solution is then injected dropwise into the hot OAm solution and aged at 320 ˚C for 20 minutes. The solution is then removed from heat and cooled to room temperature. To purify the nanosheets, hexanes (15 mL) and isopropanol (15 mL) were added and the solution was centrifuged at 8700 rpm for 10 min. After the supernatant was decanted, the solid was resuspended in hexanes with an aliquot of triethylamine (1.7 mL, 12.3 mmol) in order to fully remove adsorbed sulfur impurities. The trimethylamine addition is also critical to maintaining colloidal stability and synthetic reproducibility during the next step of the synthesis. This solution

was again precipitated with isopropanol and centrifuged. The solid was collected and dried at 120 °C under inert atmosphere for 20 minutes. The dried nanosheets were stored under inert atmosphere as a powder.

1.6.3 Synthesis of Ni-Li_xWS_y nanosheets

To the dried WS_2 nanosheets (5 mg, 0.0125 mmol), a 0.1 M solution of n-BuLi in hexanes (1 mL) was added under inert atmosphere and stirred for 2 hours. The nanosheets are completely colloidal in hexanes. The Li-treated nanosheets were rinsed with excess hexanes and redispersed in NMF. Varying volumes of a Ni precursor solution (0.04 M $NiCl_2$ in NMF) were then added and stirred for 24 hours at room temperature to achieve variable Ni surface loading. Eight different Ni loadings with respect to to W, ranging from 0.1 eq. (3.5 uL) to 2 eq. (70 uL), were synthesized. After the Ni functionalization step, the nanosheets were precipitated with ethanol (1.25 mL) and centrifuged at 13000 rpm for 7 minutes. The supernatant was decanted and the cleaning step repeated one time. The Ni-functionalized nanosheets were resuspended in NMF to achieve a nominal concentration of 0.0125 M by W at.%.

1.6.4 Synthesis of NiS

This synthesis is based on a literature procedure.[2] In a 3-neck round bottom flask, a solution of nickel nitrate (0.2908 g, 1 mmol) and oleylamine (10 ml) was heated at 100 °C for 1 hour under N_2. In another 3-neck round bottom flask, elemental sulfur (0.0321 g, 1 mmol) and oleylamine (10 ml) were heated at 70 °C for 30 minutes. The sulfur precursor solution was injected into the nickel precursor solution at 100 °C and heated rapidly to 210 °C. After 1 hour, the NiS nanoparticles were collected by centrifugation and rinsed with an excess of ethanol. These nanoparticles were redispersed in hexanes to give a solution with 12.5 mM nominal concentration.

1.6.5 Synthesis of Ni_3S_2

This synthesis is based on a literature procedure.[3] A solution of $Ni(acac)_2$ (200 mg, 0.78 mmol), cysteamine (50 mg, 0.65 mmol) and 1,5-pentanediol (20 mL) was heated to 250 °C and refluxed for 30 minutes. After the flask was cooled to room temperature, the Ni_3S_2 nanoparticles

were collected by centrifugation and rinsed with an excess of isopropanol. These nanoparticles were redispersed in in ethanol to give a solution with 12.5 mM nominal concentration.

1.6.6 Synthesis of $Ni(OH)_2$ and NiFe LDH control samples

Control samples of $Ni(OH)_2$ and $Ni_xFe_{1-x}(OH)_2$ were synthesized following a previously reported method.[4] $Ni(NO_3)_2 \cdot 6\ H_2O$ and $Fe(NO_3)_3 \cdot 9\ H_2O$ (1 mmol total) in different ratios were dissolved in water. Aliquots of a 1.0 M KOH (aq.) solution were added until the pH reached 10. The solution was then transferred to an autoclave and heated to 150 °C for 12 hours. The resulting solid was rinsed with excess H_2O and EtOH and dried at 60 °C. In order to deposit these materials uniformly onto electrodes, the metal hydroxide (5 mg) was sonicated in a Nafion and ethanol solution (1 mL, 0.25 wt.% Nafion) until a stable suspension was achieved.

1.6.7 Physical Characterization Methods

Atomic force microscopy (AFM) data were obtained using a Veeco Dimension 3100 AFM using tapping mode. Transmission electron microscopy (TEM) images were acquired using an FEI Tecnai T20 TEM equipped with a 200 kV LaB6 filament. High-angle annular dark-field scanning transmission electron microscopy (HAADF-STEM) and energy-dispersive spectroscopy (EDS) mapping were obtained on an FEI Talos F200X S/TEM with a 200 kV X-FEG field-emission source and a super X-EDS system. High resolution TEM and STEM images were collected using a Thermo Scientific Themis Z with energy of 300kV equipped with a Gatan Quantum 965 detector for EELS measurements. Zeta-potential measurements were acquired using a Malvern Instrument Zetasizer Nano-Z at room temperature. Inductively coupled plasma-optical emission spectroscopy (ICP-OES) was collected using an iCAP 7000 Plus Series ICP-OES. An average of three measurements were taken at both the tungsten (239.709 nm) and nickel (221.647 nm) wavelengths. UV-Vis data was collected using an Agilent Cary 6000i UV-Vis-NIR Spectrophotometer equipped with a PTM detector. X-ray photoelectron spectroscopy (XPS) data were obtained with a Kratos AXIS Ultra Delay-Line Detector Imaging X-ray Photoelectron Spectrometer.

X-ray absorption spectroscopy (XAS) experiments were carried out at the 10-ID beamline at the Advanced Photon Source (APS), Argonne National Laboratory at the Ni K edge (8.3328 keV) in transmission mode. Samples were supported on carbon and pressed to form a self-

supported wafer. Spectra were obtained at room temperature. During each measurement, a Ni foil was scanned simultaneously through a third ion chamber for internal energy calibration. WINXAS 3.1 software was used to analyze the collected data. EXAFS coordination parameters were obtained by a least-squares fit in R-space of the k^2-weighed Fourier transform data from 2.7 to 7.0 $Å^{-1}$. EXAFS fitting of the first and second coordination shell was carried between 0.6 and 3.2 Å in R-space. Fittings were done by refining bond distances (R), coordination numbers (CN) and energy shift (E_0). The Debye-Waller factor ($\Delta\sigma^2$) was kept constant for each sample. Phase and amplitude fitting functions were determined from Ni foil (Ni–Ni CN=12 at R=2.492 Å). FEFF6 calculations were used to obtain theoretical phase and amplitude files for Ni–O, Ni–S, and Ni–Ni.

Powder X-ray diffraction (XRD) measurements were carried out at the 11-ID-C beamline at the APS using X-rays of λ = 0.1173 Å (105.6 keV) using a PerkinElmer large-area detector to acquire data. Samples were supported on carbon and diluted with silica to obtain a self-supported pellet. Background scattering of silica, carbon and the empty cell were collected under the same conditions and subtracted from the sample XRD pattern. The powder X-ray diffraction pattern for as-synthesized WS2-OAm was acquired using a Panalytical Empyrean Powder X-ray Diffractometer with Cu K-α X-rays of λ = 1.5406 Å (8.04 keV).

Samples for TEM were prepared by drop casting from a 12.5 mM colloidal solution onto a carboncoated Cu grid. To obtain characterization data for samples post cyclic voltammetry, the electrode was immersed in ethanol and sonicated until all of the powder came off the substrate. Varying volumes of ethanol were required to remove the catalyst depending on electrode size: 200 µL for the 0.0707 cm^2 glassy carbon electrode or 3 mL for the 0.7 cm^2 fluorine-doped tin oxide electrode. The ethanol suspension was then centrifuged at 13000 rpm for 5 min, and the supernatant was removed. The solid was dried in air prior to analysis.

Samples for HR-STEM were cleaned 5 times with ethanol to ensure the complete removal of any organic residues and solvent NMF. The nanosheets were then diluted 5 times (2.5 mM) and drop casted onto a Au grid coated with an ultrathin carbon film (Ted Pella, 3 nm). The Au grid was kept under inert atmosphere and cleaned with an Ar plasma prior to imaging.

Samples for zeta-potential measurements were prepared by sonicating 1 mg of sample in 1 mL of water and then adding 1 mL of phosphate buffer (pH ~7). The solution was sonicated until a uniform dispersion was achieved, and 500 µL of this solution, transferred to a folded capillary zeta cell (Malvern), was utilized for the measurement.

Samples for ICP-OES were cleaned 5 times with ethanol to ensure the complete removal of any organic residues and solvent NMF. The samples were digested using aqua-regia (3:1) for two days and diluted with 2 wt.% aqueous HNO_3.

1.6.8 Electrochemical Methods

Electrochemical experiments were conducted on Gamry Interface 1010B potentiostat. The working electrode was prepared by drop casting 1 μL of a 12.5 mM colloidal solution. The samples were dried for 25 minutes at 60 °C. The counter electrode was a Pt mesh gauze. The electrolyte used for all electrochemical experiments was 0.1 M KOH with pH of 13 purged with N_2. Currents are reported with anodic current as positive and cathodic current as negative. Potentials were measured against a Ag/AgCl reference (3 M NaCl) and converted to the RHE reference scale using:

$$E\ (\text{vs RHE}) = E\ (\text{vs Ag/AgCl}) + 0.210\ \text{V} + 0.0591\ \text{V}*\text{pH}$$

Cyclic voltammetry was performed for all samples between 1.67 V and –0.3 V vs RHE at 100 mV s^{-1} scan rate. Linear sweep voltammetry was subsequently carried out from 1.28 V to 1.67 V vs. RHE at a scan rate of 1 mV s^{-1} to generate the Tafel plot. The solution was purged with N_2 for at least 10 minutes prior to all electrochemical experiments. To assess the stability of the Ni-Li_xWS_2 samples, CV scanning over 1000 cycles was carried out on two representative loadings of Ni-Li_xWS_2 (14% and 47%) and on $Ni(OH)_2$ as a control sample.

The activity for the oxygen evolution reaction is assessed at 1.63 V vs. RHE in the 4th and 75th anodic scans. Both geometric and Ni-normalized current densities are reported. To obtain the Ni normalized current density, the Ni(III/II) reduction peak area between 1.37 V and 1.5 V is integrated for each scan and normalized relative to a Ni single crystal.[5] The roughness factor (RF) is obtained based on the following equation:

$$RF = \frac{Area\ of\ Ni(III/II)\ Reduction}{246\ uC/cm2}$$

A number of Ni-containing reference samples were prepared for comparison to Ni-Li_xWS_y samples. NiS nanoparticles are prepared as a 12.5 mM colloidal solution in hexanes and Ni_3S_2 nanoparticles are prepared as a colloidal solution in ethanol. $Ni_xFe_{1-x}(OH)_2$ and $Ni(OH)_2$ are prepared as suspensions in an ethanol solution containing Nafion binder. In all cases, 1 μL of the catalyst solution is deposited onto a glassy carbon electrode for electrochemical experiments.

1.7 Acknowledgements

We acknowledge Dr. Mark Warren for assistance with XAS experiments and Nicole Escorcia for assistance with XAS data fitting. We acknowledge Nicole Libretto, Johnny Zhuchen, and Professor Jeffrey Miller for assistance in collecting synchrotron XRD data. We acknowledge Wei Hong for help in collecting STEM-EDS mapping data. This research was supported by Purdue University. XPS and STEM-EELS data were obtained at the Surface Analysis Facility and Electron Microscopy Facility, respectively, of the Birck Nanotechnology Center, Purdue University. Use of the Advanced Photon Source is supported by the U.S. Department of Energy, Office of Science, Office of Basic Energy Sciences, under contract DEAC02-06CH11357. MRCAT operations are supported by the Department of Energy and the MRCAT member institutions.

1.8 Supplemental Information

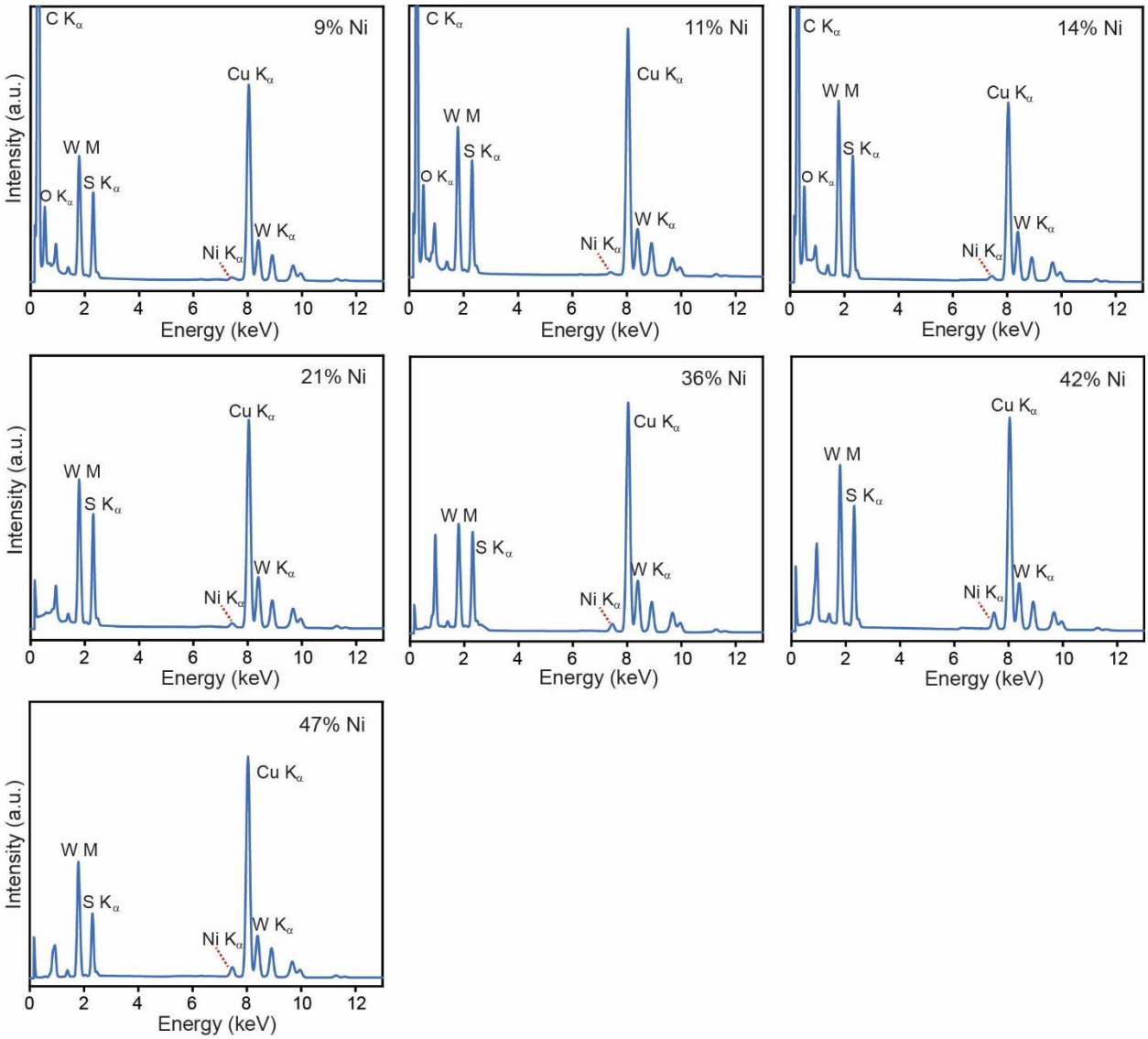

Figure 1.30. EDS spectra for all Ni-Li_xWS_y samples.

Table 1.10. Summary of elemental analysis obtained using XPS on selected Ni-Li_xWS_y samples.

Sample	**W at.%**	**S at.%**	**Ni at.%**	**W:Ni (%)**	**Ratio W:S**	**Ratio W+Ni : S**
WS_2	31	69	---	---	1 : 2	---
Li_xWS_y	30	70	---	---	1 : 2	---
14% Ni	29	69	2.0	94 : 6	1 : 2	1 : 2
47% Ni	27	65	7.0	79 : 21	1 : 2	1 : 2

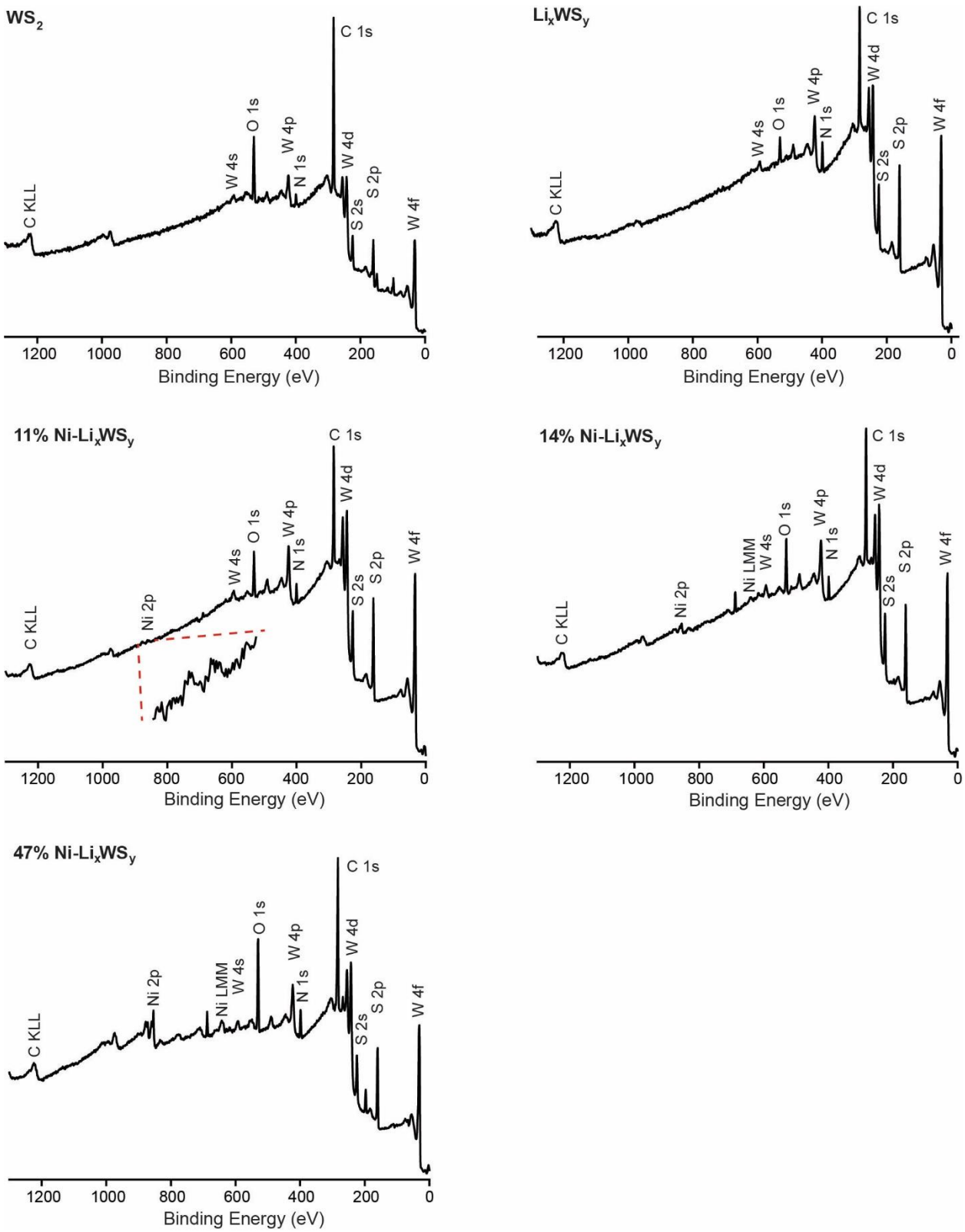

Figure 1.31. XPS survey spectra of as-synthesized WS_2-OAm, Li_xWS_y, and selected Ni-Li_xWS_y samples.

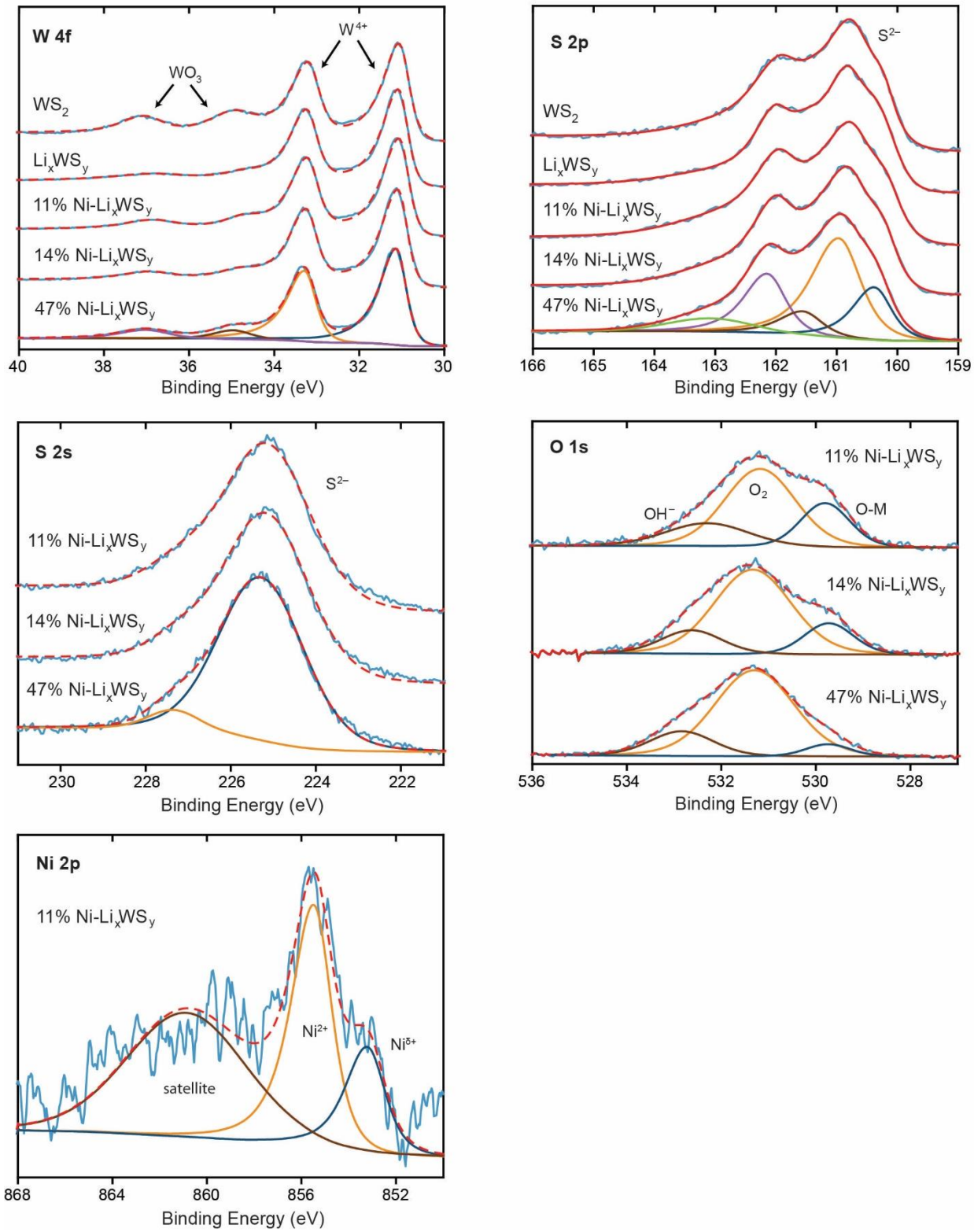

Figure 1.32. High-resolution XPS data of the W 4f, S 2p, S 2s, O 1s, and Ni 2p regions. The Ni 2p region for the 14% and 47% Ni-Li_xWS_y samples are provided in the main text.

Table 1.11. Summary of elemental analysis obtained via EDS for NiFe LDH samples.

Ratio Ni : Fe	**Ni at.%**	**Fe at.%**
1:1	47	53
4:1	79	21
9:1	90	10

Table 1.12. Summary of elemental analysis obtained via EDS after 75 CV scans under OER conditions for all Ni-Li_xWS_y samples.

Sample	**W at%**	**S at%**	**Ni at%**	**W:Ni (%)**	**W+Ni : S**
9% Ni	22	76	2.0	92 : 8	1 : 3
11% Ni	25	71	4.0	86 : 14	1 : 2
14% Ni	22	76	2.0	92 : 8	1 : 3
21% Ni	22	74	4.0	85 : 15	1 : 3
36% Ni	28	67	5.0	85 : 15	1 : 2
42% Ni	24	70	6.0	80 : 20	1 : 2
47% Ni	21	70	9.0	70 : 30	1 : 2

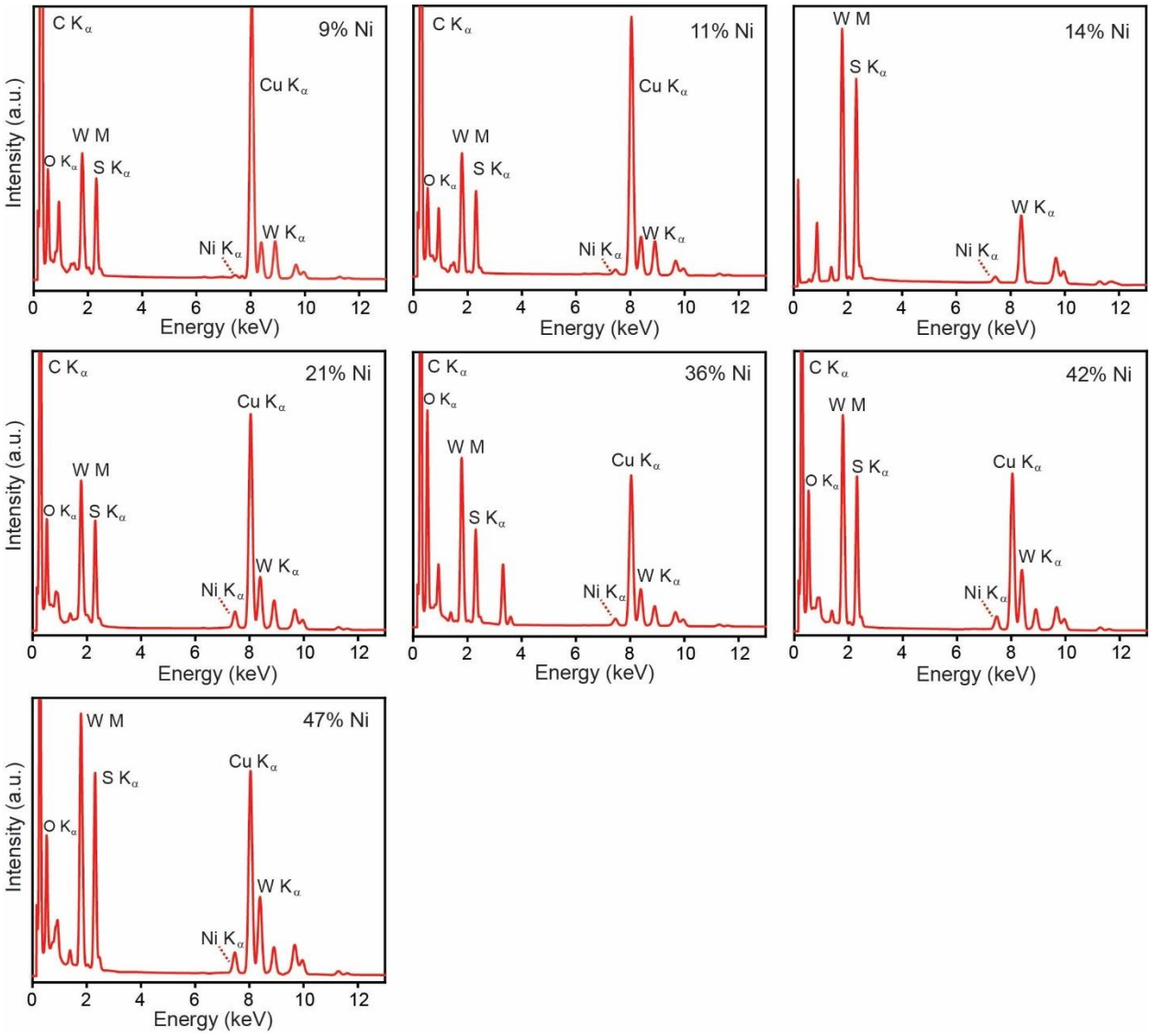

Figure 1.33. EDS spectra after 75 CV scans under OER conditions for all Ni-Li_xWS_y samples.

Table 1.13. Ni K edge EXAFS best fit parameters after 75 CV scans under OER conditions for 47% and 36% Ni-Li_xWS_y. The 14% Ni-Li_xWS_y sample had insufficient data quality to perform EXAFS fitting.

Sample	**XANES Energy (KeV)**	**XANES Energy (KeV) pre-edge**	**Scattering Pair**	**CN**	**R (Å)**	**$\Delta\sigma^2$(Å)^2**	**E_0 (eV)**	**Res. %**
Ni Foil	8.3328	---	Ni-Ni	12	2.492	0.000	---	---
$Ni(OH)_2$	8.3469	8.332	Ni-O	6.3	2.069	0.001	0.63	---
			Ni-Ni	6.3	3.114	0.001	-0.99	
47% Ni	8.3461	8.332	Ni-O	5.2	2.109	0.001	2.20	6.62%
			Ni-S	0.67	2.213	0.001	-0.78	
			Ni-Ni	4.9	3.109	0.003	1.35	
36% Ni	8.3462	8.333	Ni-O	5.1	2.106	0.001	1.92	6.73%
			Ni-S	0.83	2.221	0.001	-6.38	
			Ni-Ni	4.6	3.104	0.003	1.26	

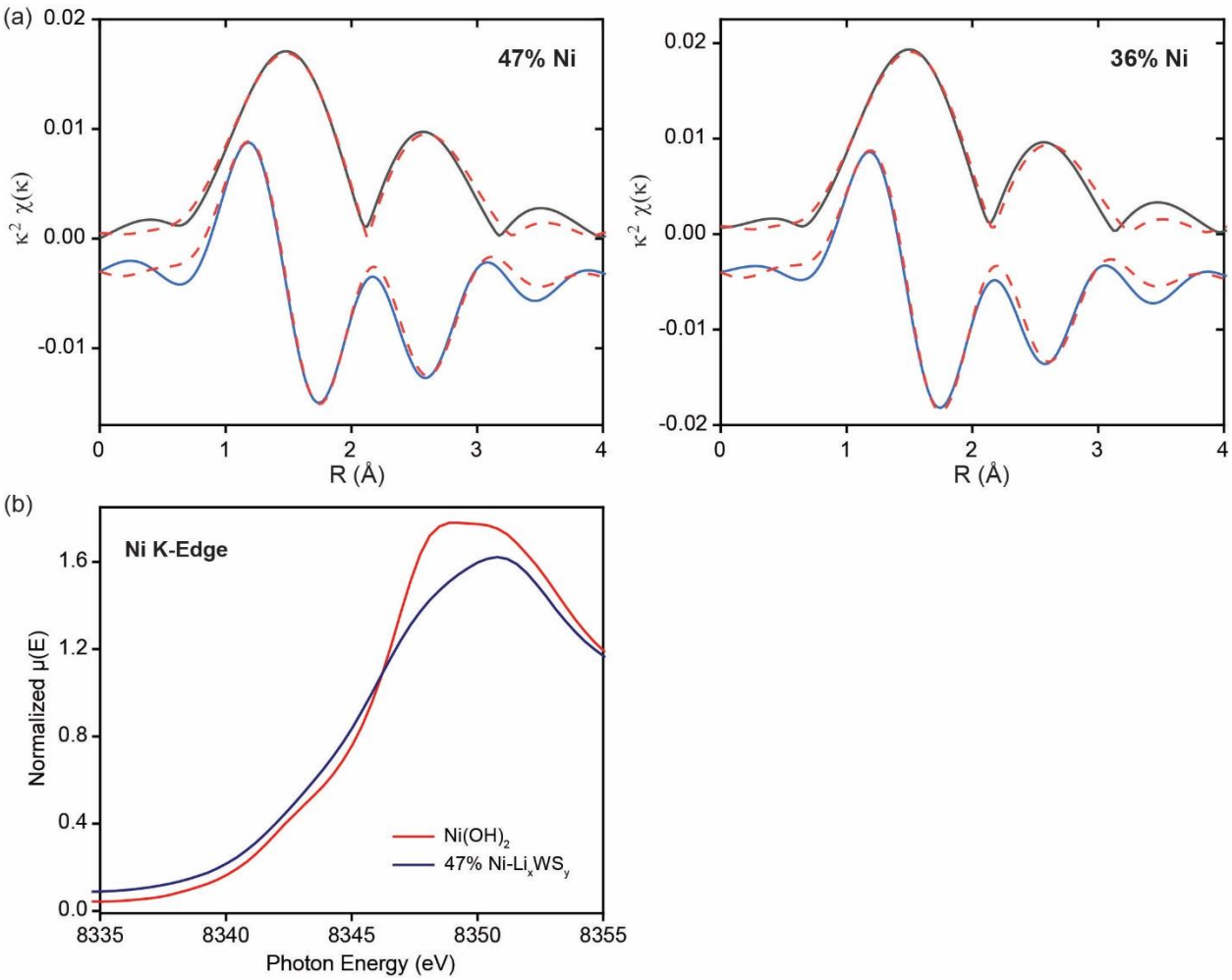

Figure 1.34. **(a)** EXAFS fits (dotted) overlaid with experimental data (solid) for the first and second coordination sphere (0.6–3.2 Å) in R-space for 47% and 36% Ni-Li_xWS_y samples after 75 CV scans under OER conditions. **(b)** XANES region for the 47% Ni-Li_xWS_y after 75 CV scans under OER conditions. The XANES region for the 36% Ni-Li_xWS_y sample is provided in the main text.

Table 1.14. Summary of elemental analysis via XPS for the 14% and 47% Ni-Li_xWS_y samples after 75 CV scans under OER conditions.

Sample	**W at.%**	**S at.%**	**Ni at.%**	**W:Ni (%)**	**Ratio W:S**	**Ratio W+Ni : S**
14% Ni	29	69	2.0	94 : 6	1 : 2	1 : 2
47% Ni	25	65	10	71 : 29	1 : 2	1 : 2

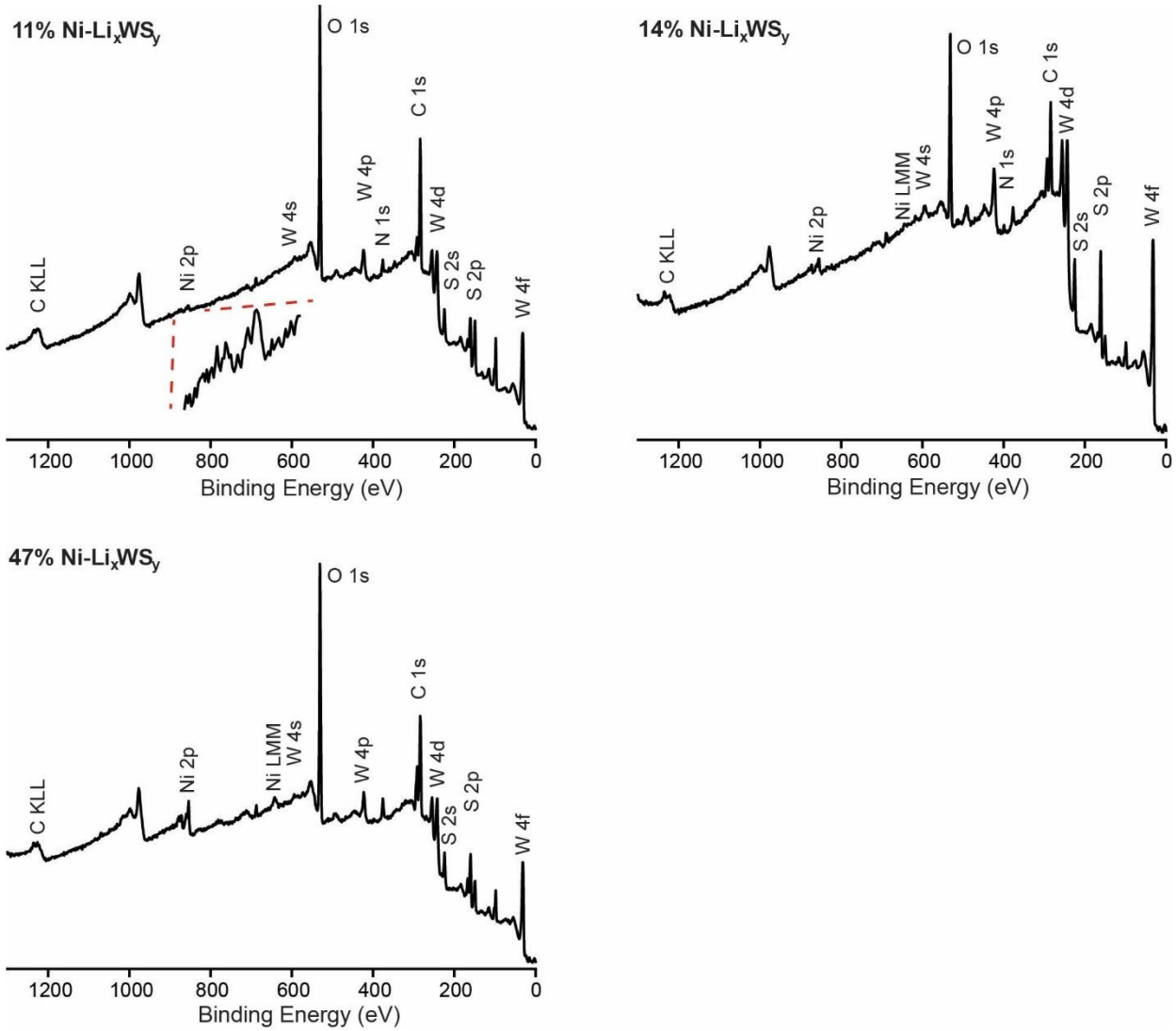

Figure 1.35. XPS survey spectra of 11%, 14% and 47% Ni-Li$_x$WS$_y$ after 75 CV scans under OER conditions.

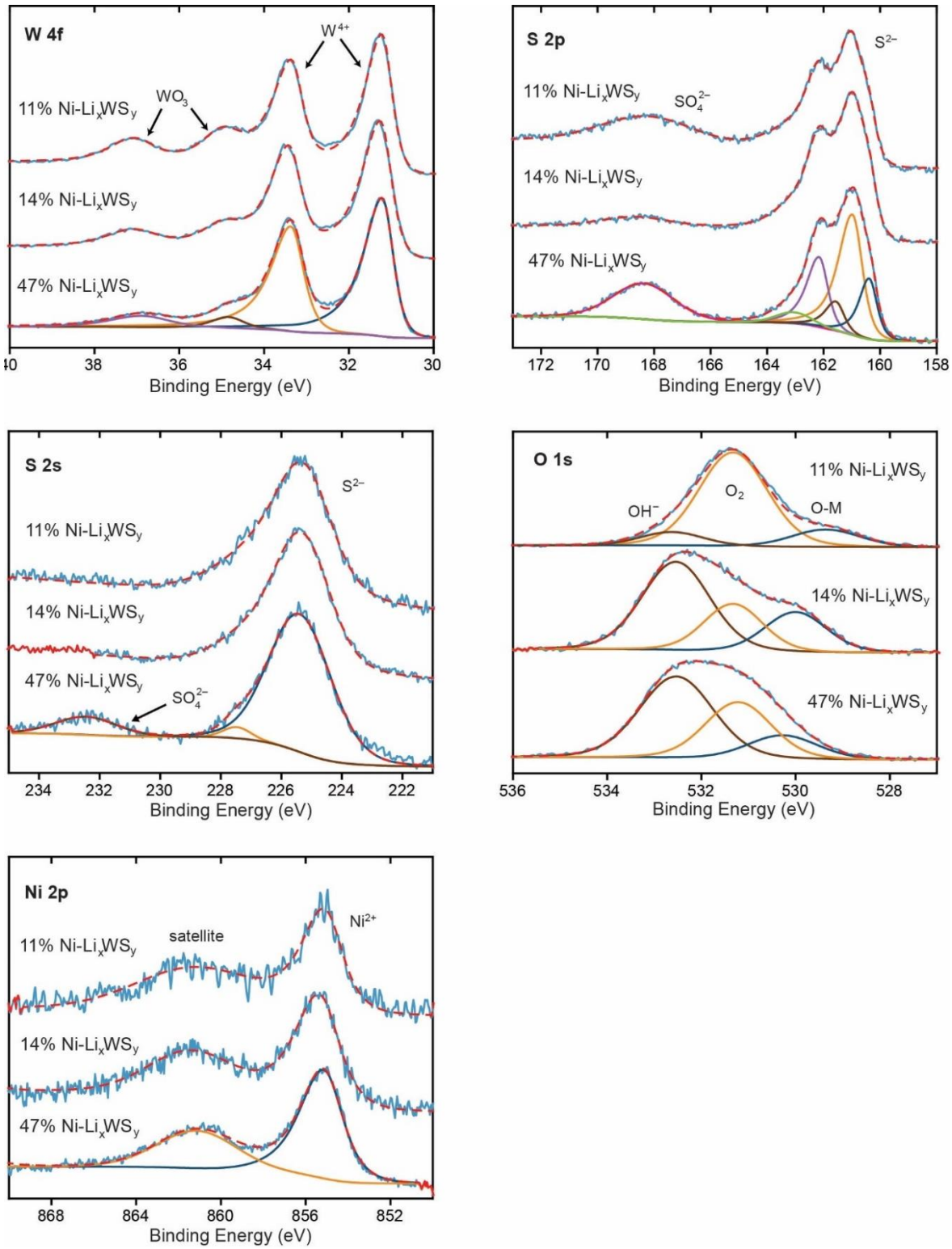

Figure 1.36. High resolution XPS spectra of the W 4f, S 2p, S 2s, O 1s and Ni 2p regions after 75 CV scans under OER conditions for the 11%, 14% and 47% Ni-Li_xWS_y samples.

Table 1.15. Electrochemical reproducibility studies on representative Ni-Li_xWS_y samples showing reproducible Ni(II/III) redox behavior and Ni RF. Averages and standard deviations are obtained from three separate electrochemical experiments for each sample.

Sample	Ni Red. E (V vs. RHE)	Avg. E_{NiRed} (V vs. RHE)	Ni Red. Area ($\mu C/cm^2$)	Ni RF	Avg. Ni RF
11% Ni	1.44	1.44 ± 0.003	133	0.54	0.56 ± 0.06
	1.44		122	0.50	
	1.43		157	0.64	
14% Ni	1.44	1.45 ± 0.001	183	0.74	0.77 ± 0.03
	1.45		187	0.76	
	1.44		200	0.81	
47% Ni	1.43	1.43 ± 0.003	1140	4.65	4.85 ± 0.3
	1.43		1130	4.57	
	1.43		1310	5.34	

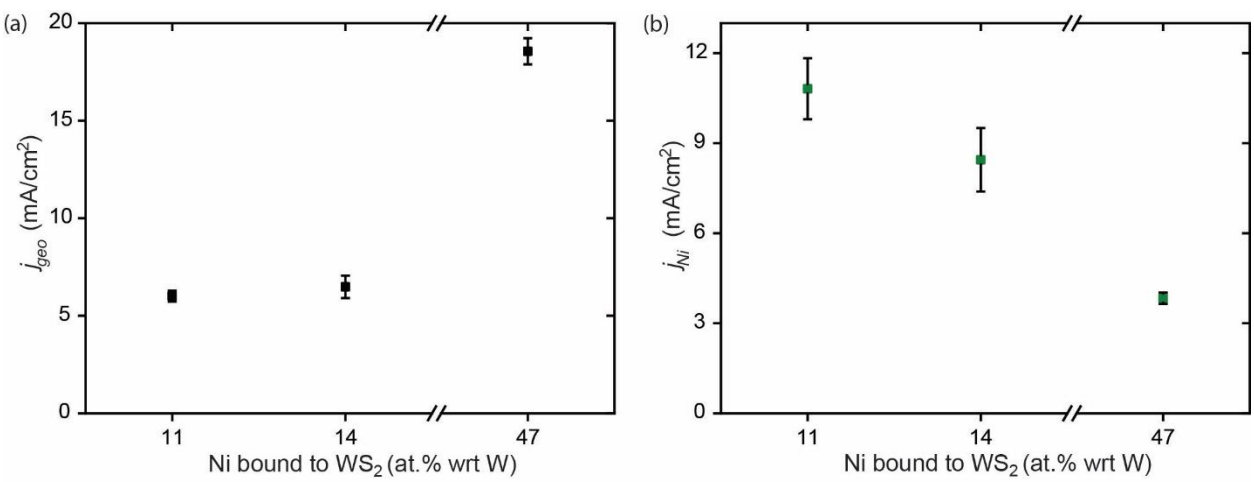

Figure 1.37. Electrochemical reproducibility studies on three representative Ni-Li_xWS_y samples. **(a)** Geometric OER current density at 1.63 V and **(b)** Ni-normalized OER current density at 1.63 V. Averages and standard deviations are obtained from three separate electrochemical experiments for each sample.

1.9 References

1. Wang, Y.; Mao, J.; Meng, X. G.; Yu, L.; Deng, D. H.; Bao, X. H. Catalysis with Two-Dimensional Materials Confining Single Atoms: Concept, Design, and Applications. *Chem. Rev.* **2019**, *119*, 1806−1854.

2. Eda, G.; Yamaguchi, H.; Voiry, D.; Fujita, T.; Chen, M. W.; Chhowalla, M. Photoluminescence from Chemically Exfoliated MoS_2. *Nano Lett*. **2011**, 11, 5111−5116.

3. Karthikeyan, J.; Komsa, H.-P.; Batzill, M.; Krasheninnikov, A. V. Which Transition Metal Atoms Can Be Embedded into Two-Dimensional Molybdenum Dichalcogenides and Add Magnetism? *Nano Lett*. **2019**, *19*, 4581−4587.

4. Tan, H.; Wang, C.; Hu, W.; Duan, H. L.; Guo, P.; Li, N.; Li, G. N.; Cai, L.; Sun, Z. H.; Hu, F. C.; Yan, W. S. Reversible Tuning of the Ferromagnetic Behavior in Mn-Doped MoS_2 Nanosheets via Interface Charge Transfer. *ACS Appl. Mater. Interfaces* **2018**, *10*, 31648−31654.

5. Vancso, P.; Popov, Z. I.; Peto, J.; Ollar, T.; Dobrik, G.; Pap, J. S.; Hwang, C. Y.; Sorokin, P. B.; Tapaszto, L. Transition Metal Chalcogenide Single Layers as an Active Platform for Single-Atom Catalysis. *ACS Energy Lett*. **2019**, *4*, 1947−1953.

6. Deng, J.; Li, H. B.; Xiao, J. P.; Tu, Y. C.; Deng, D. H.; Yang, H. X.; Tian, H. F.; Li, J. Q.; Ren, P. J.; Bao, X. H. Triggering the Electrocatalytic Hydrogen Evolution Activity of the Inert Two-Dimensional MoS_2 Surface via Single-Atom Metal Doping. *Energy Environ. Sci.* **2015**, *8*, 1594−1601.

7. Jin, Y. Y.; Zeng, Z. Y.; Xu, Z. W.; Lin, Y. C.; Bi, K. X.; Shao, G. L.; Hu, T. S.; Wang, S. S.; Li, S. S.; Suenaga, K.; Duan, H. G.; Feng, Y. X.; Liu, S. Synthesis and Transport Properties of Degenerate p-Type Nb-Doped WS_2 Monolayers. *Chem. Mater*. **2019**, *31*, 3534−3541.

8. Lin, Y. C.; Dumcenco, D. O.; Komsa, H. P.; Niimi, Y.; Krasheninnikov, A. V.; Huang, Y. S.; Suenaga, K. Properties of Individual Dopant Atoms in Single-Layer MoS_2: Atomic Structure, Migration, and Enhanced Reactivity. *Adv. Mater*. **2014**, *26*, 2857−2861.

9. Xuan, N. N.; Chen, J. H.; Shi, J. J.; Yue, Y. W.; Zhuang, P. Y.; Ba, K.; Sun, Y. Y.; Shen, J. F.; Liu, Y. Y.; Ge, B. H.; Sun, Z. Z. Single-Atom Electroplating on Two Dimensional Materials. *Chem. Mater*. **2019**, *31*, 429−435.

10. Lau, T. H. M.; Wu, S.; Kato, R.; Wu, T. S.; Kulhavy, J.; Mo, J. Y.; Zheng, J. W.; Foord, J. S.; Soo, Y. L.; Suenaga, K.; Darby, M. T.; Tsang, S. C. E. Engineering Monolayer 1T-MoS_2 into a Bifunctional Electrocatalyst via Sonochemical Doping of Isolated Transition Metal Atoms. *ACS Catal*. **2019**, *9*, 7527−7534.

11. Yeh, C. H.; Chen, H. C.; Lin, H. C.; Lin, Y. C.; Liang, Z. Y.; Chou, M. Y.; Suenaga, K.; Chiu, P. W. Ultrafast Monolayer In/Gr-WS_2-Gr Hybrid Photodetectors with High Gain. *ACS Nano* **2019**, *13*, 3269−3279.

12. Zhang, K. H.; Feng, S. M.; Wang, J. J.; Azcatl, A.; Lu, N.; Addou, R.; Wang, N.; Zhou, C. J.; Lerach, J.; Bojan, V.; Kim, M. J.; Chen, L. Q.; Wallace, R. M.; Terrones, M.; Zhu, J.; Robinson, J. A. Manganese Doping of Monolayer MoS_2: The Substrate Is Critical. *Nano Lett.* **2015**, *15*, 6586−6591.

13. Suh, J.; Park, T. E.; Lin, D. Y.; Fu, D. Y.; Park, J.; Jung, H. J.; Chen, Y. B.; Ko, C.; Jang, C.; Sun, Y. H.; Sinclair, R.; Chang, J.; Tongay, S.; Wu, J. Q. Doping against the Native Propensity of MoS_2: Degenerate Hole Doping by Cation Substitution. *Nano Lett*. **2014**, *14*, 6976−6982.

14. Xiong, Q. Z.; Wang, Y.; Liu, P. F.; Zheng, L. R.; Wang, G. Z.; Yang, H. G.; Wong, P. K.; Zhang, H. M.; Zhao, H. J. Cobalt Covalent Doping in MoS_2 to Induce Bifunctionality of Overall Water Splitting. *Adv. Mater*. **2018**, *30*, 1801450.

15. Tang, K.; Wang, X. F.; Li, Q.; Yan, C. L. High Edge Selectivity of In Situ Electrochemical Pt Deposition on Edge-Rich Layered WS_2 Nanosheets. *Adv. Mater*. **2018**, *30*, 1704779. Luo, Z. Y.; Ouyang, Y. X.; Zhang, H.; Xiao, M. L.; Ge, J. J.; Jiang, Z.; Wang, J. L.; Tang, D.

16. M.; Cao, X. Z.; Liu, C. P.; Xing, W. Chemically Activating MoS_2 via Spontaneous Atomic Palladium Interfacial Doping towards Efficient Hydrogen Evolution. *Nat. Commun.* **2018**, *9*, 2120.

17. Voiry, D.; Goswami, A.; Kappera, R.; Silva, C. D. C. E.; Kaplan, D.; Fujita, T.; Chen, M. W.; Asefa, T.; Chhowalla, M. Covalent Functionalization of Monolayered Transition Metal Dichalcogenides by Phase Engineering. *Nat. Chem.* **2015**, *7*, 45−49.

18. Knirsch, K. C.; Berner, N. C.; Nerl, H. C.; Cucinotta, C. S.; Gholamvand, Z.; McEvoy, N.; Wang, Z. X.; Abramovic, I.; Vecera, P.; Halik, M.; Sanvito, S.; Duesberg, G. S.; Nicolosi, V.; Hauke, F.; Hirsch, A.; Coleman, J. N.; Backes, C. Basal-Plane Functionalization of Chemically Exfoliated Molybdenum Disulfide by Diazonium Salts. *ACS Nano* **2015**, *9*, 6018−6030.

19. Benson, E. E.; Zhang, H. Y.; Schuman, S. A.; Nanayakkara, S. U.; Bronstein, N. D.; Ferrere, S.; Blackburn, J. L.; Miller, E. M. Balancing the Hydrogen Evolution Reaction, Surface Energetics, and Stability of Metallic MoS_2 Nanosheets via Covalent Functionalization. *J. Am. Chem. Soc*. **2018**, *140*, 441−450.

20. Tuci, G.; Mosconi, D.; Rossin, A.; Luconi, L.; Agnoli, S.; Righetto, M.; Pham-Huu, C.; Ba, H.; Cicchi, S.; Granozzi, G.; Giambastiani, G. Surface Engineering of Chemically Exfoliated MoS_2 in a ″Click″: How To Generate Versatile Multifunctional Transition Metal Dichalcogenides-Based Platforms. *Chem. Mater*. **2018**, *30*, 8257−8269.

21. Mahler, B.; Hoepfner, V.; Liao, K.; Ozin, G. A. Colloidal Synthesis of 1T-WS_2 and 2H-WS_2 Nanosheets: Applications for Photocatalytic Hydrogen Evolution. *J. Am. Chem. Soc.* **2014**, *136*, 14121−14127.

22. Liu, Z. Q.; Li, N.; Su, C.; Zhao, H. Y.; Xu, L. L.; Yin, Z. Y.; Li, J.; Du, Y. P. Colloidal Synthesis of 1T' Phase Dominated WS_2 towards Endurable Electrocatalysis. *Nano Energy* **2018**, *50*, 176−181.

23. Zong, X.; Han, J. F.; Ma, G. J.; Yan, H. J.; Wu, G. P.; Li, C. Photocatalytic H_2 Evolution on CdS Loaded with WS_2 as Cocatalyst under Visible Light Irradiation. *J. Phys. Chem. C* **2011**, *115*, 12202−12208.

24. Cheng, L.; Huang, W. J.; Gong, Q. F.; Liu, C. H.; Liu, Z.; Li, Y. G.; Dai, H. J. Ultrathin WS_2 Nanoflakes as a High-Performance Electrocatalyst for the Hydrogen Evolution Reaction. *Angew. Chem., Int. Ed*. **2014**, *53*, 7860−7863.

25. Jo, S.; Ubrig, N.; Berger, H.; Kuzmenko, A. B.; Morpurgo, A. F. Mono- and Bilayer WS_2 Light-Emitting Transistors. *Nano Lett*. **2014**, *14*, 2019−2025.

26. Lukowski, M. A.; Daniel, A. S.; English, C. R.; Meng, F.; Forticaux, A.; Hamers, R. J.; Jin, S. Highly Active Hydrogen Evolution Catalysis from Metallic WS_2 Nanosheets. *Energy Environ. Sci*. **2014**, *7*, 2608−2613.

27. Chhowalla, M.; Shin, H. S.; Eda, G.; Li, L. J.; Loh, K. P.; Zhang, H. The Chemistry of Two-Dimensional Layered Transition Metal Dichalcogenide Nanosheets. *Nat. Chem*. **2013**, *5*, 263−275.

28. Backes, C.; Berner, N. C.; Chen, X.; Lafargue, P.; LaPlace, P.; Freeley, M.; Duesberg, G. S.; Coleman, J. N.; McDonald, A. R. Functionalization of Liquid-Exfoliated Two-Dimensional 2H-MoS_2. *Angew. Chem., Int. Ed*. 2015, 54, 2638−2642.

29. Chen, X.; Berner, N. C.; Backes, C.; Duesberg, G. S.; McDonald, A. R. Functionalization of Two-Dimensional MoS2: On the Reaction between MoS_2 and Organic Thiols. *Angew. Chem., Int. Ed.* **2016**, *55*, 5803−5808.

30. Chen, X.; McDonald, A. R. Functionalization of Two- Dimensional Transition-Metal Dichalcogenides. *Adv. Mater*. **2016**, *28*, 5738−5746.

31. Chou, S. S.; De, M.; Kim, J.; Byun, S.; Dykstra, C.; Yu, J.; Huang, J. X.; Dravid, V. P. Ligand Conjugation of Chemically Exfoliated MoS_2. *J. Am. Chem. Soc.* **2013**, *135*, 4584−4587.

32. Zhou, L.; He, B. Z.; Yang, Y.; He, Y. G. Facile Approach to Surface Functionalized MoS_2 Nanosheets. *RSC Adv*. **2014**, *4*, 32570−32578.

33. Kim, J. S.; Yoo, H. W.; Choi, H. O.; Jung, H. T. Tunable Volatile Organic Compounds Sensor by Using Thiolated Ligand Conjugation on MoS_2. *Nano Lett.* **2014**, *14*, 5941−5947.

34. Robertson, A. W.; Lin, Y. C.; Wang, S. S.; Sawada, H.; Allen, C. S.; Chen, Q.; Lee, S.; Lee, G. D.; Lee, J.; Han, S.; Yoon, E.; Kirkland, A. I.; Kim, H.; Suenaga, K.; Warner, J. H. Atomic Structure and Spectroscopy of Single Metal (Cr, V) Substitutional Dopants in Monolayer MoS_2. *ACS Nano* **2016**, *10*, 10227−10236.

35. Li, H. S.; Wang, S. S.; Sawada, H.; Han, G. G. D.; Samuels, T.; Allen, C. S.; Kirkland, A. I.; Grossman, J. C.; Warner, J. H. Atomic Structure and Dynamics of Single Platinum Atom Interactions with Monolayer MoS_2. *ACS Nano* **2017**, *11*, 3392−3403.

36. Deepak, F. L.; Esparza, R.; Borges, B.; Lopez-Lozano, X.; Jose-Yacaman, M. Direct Imaging and Identification of Individual Dopant Atoms in MoS2 and WS2 Catalysts by Aberration Corrected Scanning Transmission Electron Microscopy. *ACS Catal*. **2011**, *1*, 537−543.

37. Liu, G. L.; Robertson, A. W.; Li, M. M. J.; Kuo, W. C. H.; Darby, M. T.; Muhieddine, M. H.; Lin, Y. C.; Suenaga, K.; Stamatakis, M.; Warner, J. H.; Tsang, S. C. E. MoS_2 Monolayer Catalyst Doped with Isolated Co Atoms for the Hydrodeoxygenation Reaction. *Nat. Chem.* **2017**, *9*, 810−816.

38. Liu, W. G.; Chen, Y. J.; Qi, H. F.; Zhang, L. L.; Yan, W. S.; Liu, X. Y.; Yang, X. F.; Miao, S.; Wang, W. T.; Liu, C. G.; Wang, A. Q.; Li, J.; Zhang, T. A Durable Nickel Single-Atom Catalyst for Hydrogenation Reactions and Cellulose Valorization under Harsh Conditions. *Angew. Chem., Int. Ed*. **2018**, *57*, 7071−7075.

39. Jiang, K.; Siahrostami, S.; Zheng, T. T.; Hu, Y. F.; Hwang, S.; Stavitski, E.; Peng, Y. D.; Dynes, J.; Gangisetty, M.; Su, D.; Attenkofer, K.; Wang, H. T. Isolated Ni Single Atoms in Graphene Nanosheets for High-Performance CO_2 Reduction. *Energy Environ. Sci*. **2018**, *11*, 893−903.

40. Tong, M. M.; Wang, L.; Yu, P.; Tian, C. G.; Liu, X.; Zhou, W.; Fu, H. G. Ni3S2 Nanosheets In Situ Epitaxially Grown on Nanorods as High Active and Stable Homojunction Electrocatalyst for Hydrogen Evolution Reaction. *ACS Sustainable Chem. Eng*. **2018**, *6*, 2474−2481.

41. Chen, G. F.; Ma, T. Y.; Liu, Z. Q.; Li, N.; Su, Y. Z.; Davey, K.; Qiao, S. Z. Efficient and Stable Bifunctional Electrocatalysts Ni/Ni_xM_y (M = P, S) for Overall Water Splitting. *Adv. Funct. Mater.* **2016**, *26*, 3314−3323.

42. Wang, C. Q.; Tian, B.; Wu, M.; Wang, J. H. Revelation of the Excellent Intrinsic Activity of $MoS_2|NiS|MoO_3$ Nanowires for Hydrogen Evolution Reaction in Alkaline Medium. *ACS Appl. Mater. Interfaces* **2017**, *9*, 7084−7090.

43. An, T. C.; Wang, Y.; Tang, J.; Wei, W.; Cui, X. Q.; Alenizi, A. M.; Zhang, L. J.; Zheng, G. F. Interlaced NiS_2-MoS_2 Nanoflake-Nanowires as Efficient Hydrogen Evolution Electrocatalysts in Basic Solutions. *J. Mater. Chem. A* **2016**, *4*, 13439−13443.

44. Luo, X. L.; Shao, Q.; Pi, Y. C.; Huang, X. Q. Trimetallic Molybdate Nanobelts as Active and Stable Electrocatalysts for the Oxygen Evolution Reaction. *ACS Catal*. **2019**, *9*, 1013−1018.

45. Cao, J. M.; Zhou, J.; Zhang, Y. F.; Wang, Y. X.; Liu, X. W. Dominating Role of Aligned MoS_2/Ni_3S_2 Nanoarrays Supported on Three-Dimensional Ni Foam with Hydrophilic Interface for Highly Enhanced Hydrogen Evolution Reaction. *ACS Appl. Mater. Interfaces* **2018**, *10*, 1752−1760.

46. Yang, Y. Q.; Zhang, K.; Lin, H. L.; Li, X.; Chan, H. C.; Yang, L. C.; Gao, Q. S. MoS_2-Ni_3S_2 Heteronanorods as Efficient and Stable Bifunctional Electrocatalysts for Overall Water Splitting. *ACS Catal*. **2017**, *7*, 2357−2366.

47. Xing, Z. C.; Yang, X. R.; Asiri, A. M.; Sun, X. P. Three-Dimensional Structures of MoS_2@Ni Core/Shell Nanosheets Array toward Synergetic Electrocatalytic Water Splitting. *ACS Appl. Mater. Interfaces* **2016**, *8*, 14521−14526.

48. Zhang, J.; Wang, T.; Liu, P.; Liu, S. H.; Dong, R. H.; Zhuang, X. D.; Chen, M. W.; Feng, X. L. Engineering Water Dissociation Sites in MoS_2 Nanosheets for Accelerated Electrocatalytic Hydrogen Production. *Energy Environ. Sci*. **2016**, *9*, 2789−2793.

49. Gong, M.; Li, Y. G.; Wang, H. L.; Liang, Y. Y.; Wu, J. Z.; Zhou, J. G.; Wang, J.; Regier, T.; Wei, F.; Dai, H. J. An Advanced Ni-Fe Layered Double Hydroxide Electrocatalyst for Water Oxidation. *J. Am. Chem. Soc*. **2013**, *135*, 8452−8455.

50. Lu, Z. Y.; Xu, W. W.; Zhu, W.; Yang, Q.; Lei, X. D.; Liu, J. F.; Li, Y. P.; Sun, X. M.; Duan, X. Three-Dimensional NiFe Layered Double Hydroxide Film for High-Efficiency Oxygen Evolution Reaction. *Chem. Commun*. **2014**, *50*, 6479−6482.

51. Song, F.; Hu, X. L. Exfoliation of Layered Double Hydroxides for Enhanced Oxygen Evolution Catalysis. *Nat. Commun*. **2014**, *5*, 4477.

52. Long, X.; Li, J. K.; Xiao, S.; Yan, K. Y.; Wang, Z. L.; Chen, H. N.; Yang, S. H. A Strongly Coupled Graphene and FeNi Double Hydroxide Hybrid as an Excellent Electrocatalyst for the Oxygen Evolution Reaction. *Angew. Chem., Int. Ed*. **2014**, *53*, 7584−7588.

53. Gong, M.; Dai, H. J. A Mini Review of NiFe-Based Materials as Highly Active Oxygen Evolution Reaction Electrocatalysts. *Nano Res.* **2015**, *8*, 23−39.

54. Lu, X. Y.; Zhao, C. A. Electrodeposition of Hierarchically Structured Three-Dimensional Nickel-Iron Electrodes for Efficient Oxygen Evolution at High Current Densities. *Nat. Commun*. **2015**, *6*, 6616.

55. Louie, M. W.; Bell, A. T. An Investigation of Thin-Film Ni-Fe Oxide Catalysts for the Electrochemical Evolution of Oxygen. *J. Am. Chem. Soc*. **2013**, *135*, 12329−12337.

56. Trotochaud, L.; Young, S. L.; Ranney, J. K.; Boettcher, S. W. Nickel-Iron Oxyhydroxide Oxygen-Evolution Electrocatalysts: The Role of Intentional and Incidental Iron Incorporation. *J. Am. Chem. Soc*. **2014**, *136*, 6744−6753.

57. Burke, M. S.; Enman, L. J.; Batchellor, A. S.; Zou, S. H.; Boettcher, S. W. Oxygen Evolution Reaction Electrocatalysis on Transition Metal Oxides and (Oxy)hydroxides: Activity Trends and Design Principles. *Chem. Mater*. **2015**, *27*, 7549−7558.

58. Karthikeyan, R.; Thangaraju, D.; Prakash, N.; Hayakawa, Y. Single-step synthesis and catalytic activity of structure-controlled nickel sulfide nanoparticles. *Crys. Eng. Comm.*, **2015**, *17*, 5431-5439.

59. Chi, W. S.; Han, J. W.; Yang, S.; Roh, D. K.; Lee, H.; Kim, J. H. Employing electrostatic self-assembly of tailored nickel sulfide nanoparticles for quasi-solid-state dye-sensitized solar cells with Pt-free counter electrodes. *Chem. Commun.*, **2012**, *48*, 9501-9503.

60. Sirisomboonchai, S.; Li, S. S.; Yoshida, A.; Li, X. M.; Samart, C.; Abudula, A.; Guan, G. Q. Fabrication of NiO Microflake@NiFe-LDH Nanosheet Heterostructure Electrocatalysts for Oxygen Evolution Reaction. *ACS Sustain. Chem. Eng.*, **2019**, *7*, 2327-2334.

61. Beden, B.; Floner, D.; Leger, J. M.; Lamy, C. A Voltammetric Study of the Formation of Hydroxides and Oxyhydroxides on Nickel Single-Crystal Electrodes in Contact with an Alkaline-Solution. *Surf. Sci.*, **1985**, *162*, 822-829.

62. Voiry, D.; Goswami, A.; Kappera, R.; Silva, C. D. C. E.; Kaplan, D.; Fujita, T.; Chen, M. W.; Asefa, T.; Chhowalla, M. Covalent functionalization of monolayered transition metal dichalcogenides by phase engineering. *Nat. Chem.*, **2015**, *7*, 45-49.

CHAPTER 2. CONTROLLING CO–S COORDINATION ENVIRONMENT IN CO-DOPED WS_2 NANOSHEETS FOR ELECTROCHEMICAL OXYGEN REDUCTION

Reproduced with permission from:
Meza, E.[†]; Hong, W. [†]; Li, C. W. "Controlling Co-S Coordination Environment in Co-doped WS_2 Nanosheets for Electrochemical Oxygen Reduction" *Submitted*, **2021**. [†]Authors contributed equally.

2.1 Abstract

Cobalt sulfide nanomaterials are among the most active and stable catalysts for the electrocatalytic oxygen reduction in pH 7 electrolyte. However, due to the complexity and dynamism of the catalytic surfaces in cobalt sulfide bulk materials, it is challenging to identify and tune the active site structure in order to achieve lower overpotential oxygen reduction reactivity. In this work, we synthesize Co single atoms supported on colloidal WS_2 nanosheets and develop a synthetic strategy to rationally control the first-shell coordination environment surrounding the adsorbed Co single atoms. By studying Co-WS_2 materials with a range of Co–S coordination numbers, we are able to identify the optimal active site for pH 7 oxygen reduction catalysis, which comprises cobalt atoms bound to the WS_2 support with Co-S coordination number of 3-4. The optimized Co-WS_2 material exhibits oxygen reduction onset potential of 0.798 V vs. RHE, comparable to the most active bulk phases of cobalt sulfide in neutral electrolyte conditions.

2.2 Introduction

First-row transition metal sulfides have emerged as alternatives to Pt-based catalysts in the oxygen reduction reaction (ORR) under a wide range of pH conditions due to their high activity, stability, and low cost.[1-7] Literature studies have focused primarily on tuning the structure of nickel and cobalt sulfides to understand the role that metal sulfide phase and composition play in dictating ORR reactivity.[8-14] The Co_9S_8 phase, in particular, has been identified as uniquely active amongst the first-row transition metal sulfides for alkaline and neutral ORR and has been studied in a wide range of composite nanostructures.[15-22] Computational studies have postulated that M–S coordination environment at the catalytic surface influences oxygen adsorbate binding energies and thus ORR catalytic turnover.[23,24] However, when experimentally altering the crystal structure

or composition of a bulk metal sulfide phase, it is challenging to isolate the role that coordination environment plays amidst the multiple geometries and oxidation states that exist within any given phase as well as the dynamic nature of the surface under electrocatalytic conditions.[24,25]

Supported single atom catalysts (SACs) are intriguing model systems for catalytic surface sites on bulk materials because their active site structure can be studied at the atomic level.[26-28] Previous work on single metal atoms supported on metal oxide and heteroatom-doped carbon materials has shown the importance of local coordination environment and metal-support interaction in influencing catalyst selectivity and reactivity.[29-33] Particular effort has been invested in active site characterization for metal single atoms supported on N-doped carbon.[34-38] Recent work on Co SACs have postulated that the number and chemical nature of coordinated nitrogen atoms in the first shell may have an impact on catalytic activity in the alkaline oxygen reduction reaction.[39,40] While different single atom coordination environments have been observed in these examples, it remains challenging to synthetically control the coordination environment surrounding a single atom catalyst. Single atoms supported on MoS_2 have also been studied extensively, primarily for use as electrocatalysts in the hydrogen evolution reaction (HER).[41] However, doped first-row transition metal single atoms are not themselves catalytically active sites for HER but rather serve to tune the electronic and catalytic properties of the MoS_2 surface.[42-44] In this work, we put forward a synthetic strategy to generate cobalt single atoms supported on WS_2 nanosheets, in which the Co–S coordination environment can be explicitly tuned through controlled introduction of excess sulfur. These Co-WS_2 nanosheets provide the basis for a systematic study on how the local coordination environment of surface cobalt sulfide active sites influence oxygen reduction reactivity in neutral electrolyte.

2.3 Results and Discussion

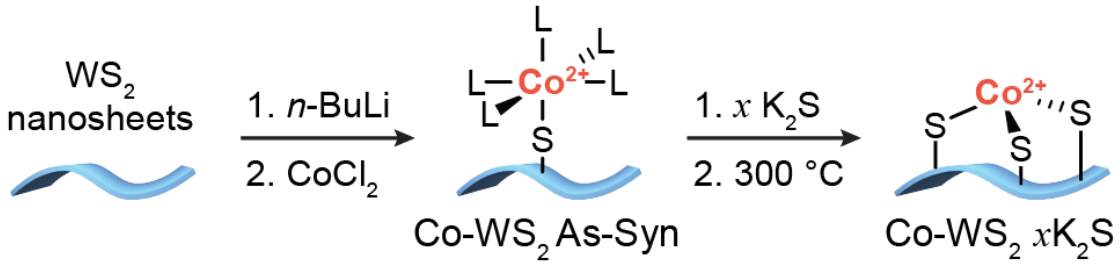

Figure 2.1. Synthetic strategy for the deposition of Co single atoms onto colloidal WS_2 nanosheets followed by controlled sulfidation and annealing steps.

2.3.1 Synthesis

The synthetic strategy to generate Co single atoms with tunable Co–S coordination environment, depicted in Figure 2.1, is based on previous work from our group on the synthesis of single atom Ni-doped WS_2 nanosheets.[45] Colloidal WS_2 nanosheets were synthesized via a literature method and activated using n-butyllithium (*n*-BuLi) to generate dangling sulfide defects on the basal planes of WS_2 (Li-WS_2).[46] A dilute solution of $CoCl_2$ (0.3 equiv. wrt W) was then introduced to the colloidal Li-WS_2 nanosheets under an inert atmosphere and permitted to passively adsorb over 24 hours. Any excess $CoCl_2$ remaining in solution was readily removed through precipitation and centrifugation of the Co-doped WS_2 nanosheets (Colloidal Co-WS_2). The loading of Co was intentionally kept at ≤0.3 equiv. in order to avoid clustering and aggregation of doped Co atoms.

In our previous work, we showed that Ni dopants adsorbed relatively weakly and in a monodentate fashion to the WS_2 surface during the colloidal synthesis. In order to tune the Co-S coordination and more strongly anchor the Co dopants to the WS_2 surface, we develop a method herein for controlled sulfidation of the adsorbed Co atoms. The colloidal Co-WS_2 nanosheets are supported on carbon black (Co-WS_2 As-Syn) and impregnated with a variable amount of potassium sulfide, ranging from 0.5 to 10 equivalents with respect to the adsorbed Co atoms. The impregnated samples are then annealed at 300 °C under an inert atmosphere and rinsed repeatedly with solvent to remove unreacted sulfides (Co-WS_2 xK_2S). The resulting nanosheets show structural and catalytic properties that are highly dependent on the amount of sulfur incorporated during the anchoring step.

2.3.2 Scanning Transmission Electron Microscopy

We utilize high-angle annular dark-field scanning transmission electron microscopy (HAADF-STEM) coupled to energy-dispersive X-ray spectroscopy (EDS) to characterize the morphology and elemental distribution of Co and W on the Co-WS_2 nanosheets. Colloidal WS_2 comprises circular nanosheets with ~100 nm diameter and 10–14 layers in thickness (Figure 2.2a).[45] After n-BuLi activation and Co adsorption, the nanosheet morphology is retained, and Co atoms are evenly distributed across the surface based on the lo-resolution HAADF-STEM image

and EDS maps (Figure 2.2b-c, 2.3a). Based on EDS, the majority of the Co introduced in solution (0.3 equiv.) is incorporated into the WS_2 nanosheets (Co:W = 0.20:1) (Table 2.1).

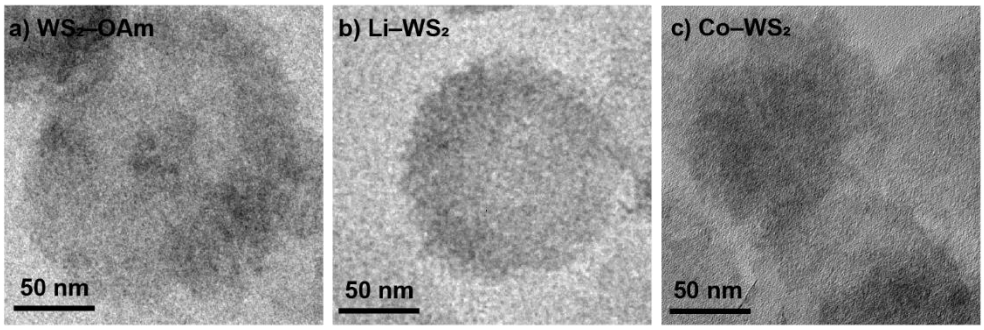

Figure 2.2. Low resolution TEM images for **(a)** colloidal WS_2-OAm nanosheets, **(b)** colloidal Li-WS_2 and **(c)** colloidal Co-WS_2.

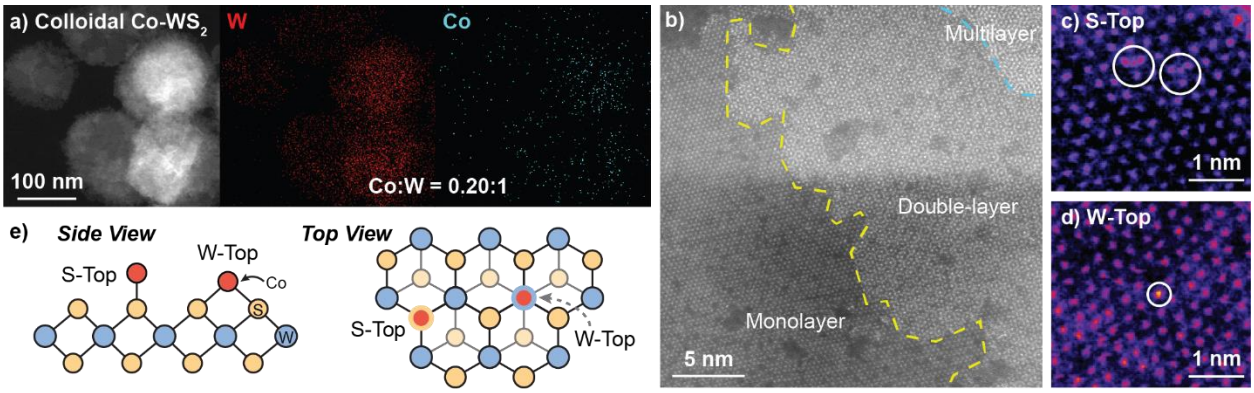

Figure 2.3. STEM imaging of colloidal Co-WS_2 samples. **(a)** Low-resolution STEM-EDS image and elemental maps of W and Co, **(b)** HR-STEM image, **(c)** HR-STEM region containing S-Top Co sites, **(d)** HR-STEM region containing W-Top sites, **(e)** schematic depicting side and top views for both S-Top and W-Top binding of Co atoms.

Table 2.1. Summary of elemental analysis obtained using EDS for Li-WS_2 and Co-WS_2 nanosheets. The tungsten M edge, sulfur K edge, and cobalt K edge were used for quantification.

Sample	***x*K_2S (Eq. wrt Co)**	**W at.%**	**S at.%**	**Co at.%**	**Co:W (X:1)**
Colloidal Li-WS_2	--	31	69	---	---
Colloidal Co-WS_2	--	22 ± 0.47	74 ± 0.61	4 ± 0.49	0.20 ± 0.02
Co-WS_2 As-Syn (Supported on C)	--	22 ± 0.56	74 ± 0.75	4 ± 0.25	0.20 ± 0.01
Co-WS_2 *x*K_2S	0	22 ± 0.60	74 ± 0.71	4 ± 0.61	0.21 ± 0.03
	0.5	23 ± 0.63	70 ± 1.0	7 ± 0.45	0.29 ± 0.01
	1.0	21 ± 0.96	73 ± 1.7	6 ± 1.1	0.29 ± 0.04
	3.0	21 ± 1.8	75 ± 1.9	4 ± 0.33	0.21 ± 0.02
	6.0	24 ± 1.4	71 ± 2.2	5 ± 0.80	0.22 ± 0.02
	10.0	18 ± 1.2	78 ± 1.4	4 ± 1.3	0.21 ± 0.02

High-resolution HAADF-STEM imaging allows us to confirm the presence of Co single atoms on the surface of the WS_2 nanosheets. Due to the n-BuLi treatment, the underlying WS_2 nanosheets exhibit variable thickness, ranging from monolayer to multilayer, and regions where W vacancies and structural disorder are present (Figure 2.3b, 2.4a). In the monolayer regions, the ordered hexagonal lattice of W atoms for the WS_2 nanosheet are clearly visible, and deviations to the hexagonal array in terms of both atomic position and contrast provide evidence for the presence of Co single atoms (Figure 2.3c-d, 2.4b-e). Atoms interstitial to the hexagonal W array, circled in Figure 2.3c, represent Co atoms bound on-top of a S atom or in a S vacancy (S-Top, Figure 2.3e). In addition, analysis of annular-dark field Z-contrast shows that Co atoms are also present on-top of W atoms in the hexagonal lattice, circled in Figure 2.3d and Figure 2.4d-e, which are likely coordinated in a bidentate or tridentate fashion to S atoms (W-Top, Figure 2.3e).

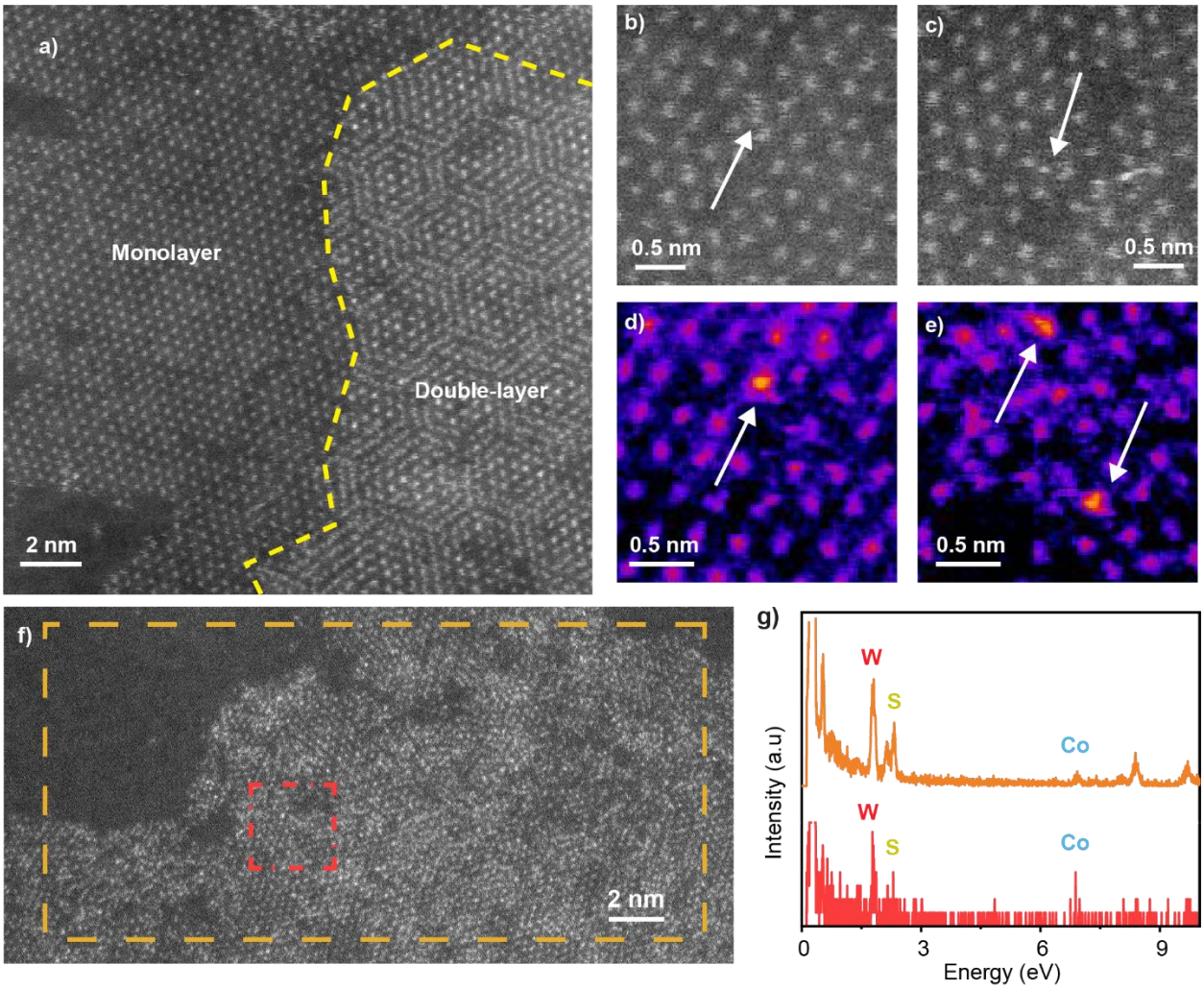

Figure 2.4. **(a)** High-resolution STEM images for the colloidal Co-WS_2 sample. Additional STEM images containing **(b-c)** S-Top Co sites and **(d-e)** W-Top Co sites. **(f, g)** STEM image and EDS spectra from boxed areas spectroscopically confirm the presence of Co.

In addition to ADF Z-contrast analysis, we also obtained EDS spectra in small regions throughout the high-resolution STEM image to ascertain that Co atoms can be spectroscopically detected. While the EDS intensity is quite weak when focused on 3 x 3 nm square regions of the monolayer Co-WS_2 nanosheets, we can clearly distinguish peaks associated with the W M, S Kα, and Co Kα transitions (Figure 2.4f-g). In addition, when the EDS spectra is obtained over a larger slightly larger region, the atomic ratio of Co:W is ~0.3:1, similar to the elemental ratios obtained in the lower resolution EDS data in Table 2.1.

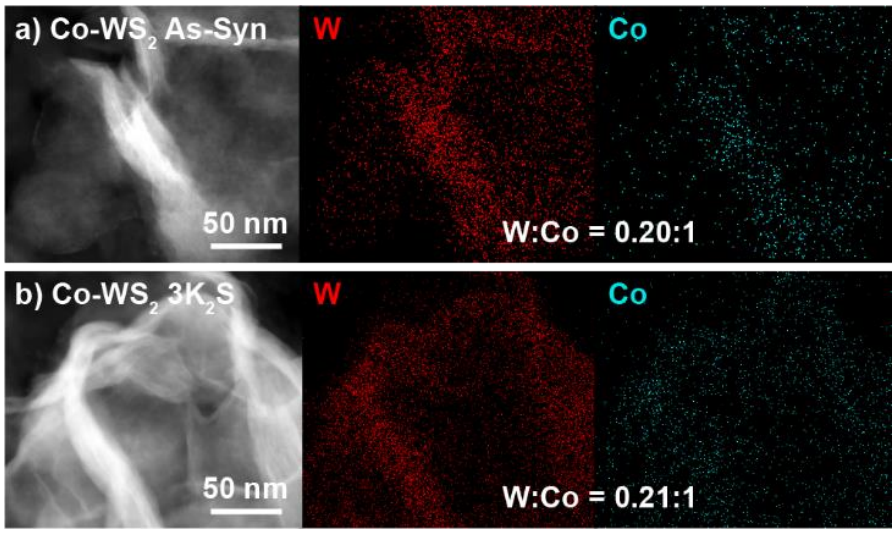

Figure 2.5. STEM-EDS image and elemental maps of W and Co for **(a)** as-synthesized Co-WS_2 and **(b)** Co-WS_2 after annealing with 3 equiv. K_2S.

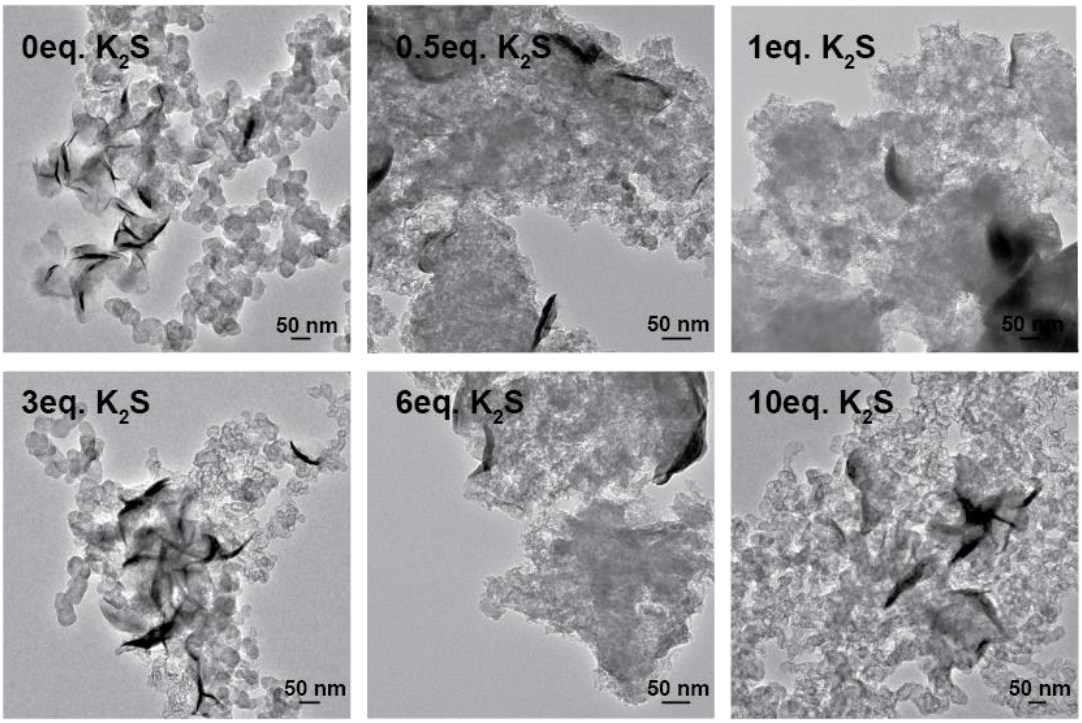

Figure 2.6. TEM images of Co-WS_2 samples annealed in the presence of varying amounts of impregnated K_2S.

Prior to sulfur addition, colloidal Co-WS_2 sample is supported on carbon black, which causes the circular nanosheets to fold onto themselves rather than lie flat on the hydrophobic carbon surface (Figure 2.5a). The Co loading and distribution remain unchanged (Table 2.1).

Impregnation of K_2S and annealing at 300 °C under N_2 does not alter the morphology or the average loading of Co relative to W (Table 2.1, Figure 2.5b, 2.6, 2.7). STEM-EDS elemental maps of K_2S-treated Co-WS_2 show that W and Co atoms remain colocalized in the sample, and Co species are evenly distributed across the WS_2 nanosheets. No evidence of CoS_x nanoparticle formation is observed. Powder X-ray diffraction (XRD) reveals a WS_2 phase transition from 1T to 2H after annealing and no Co-containing crystalline phases (Figure 2.8, 2.9).[45-48]

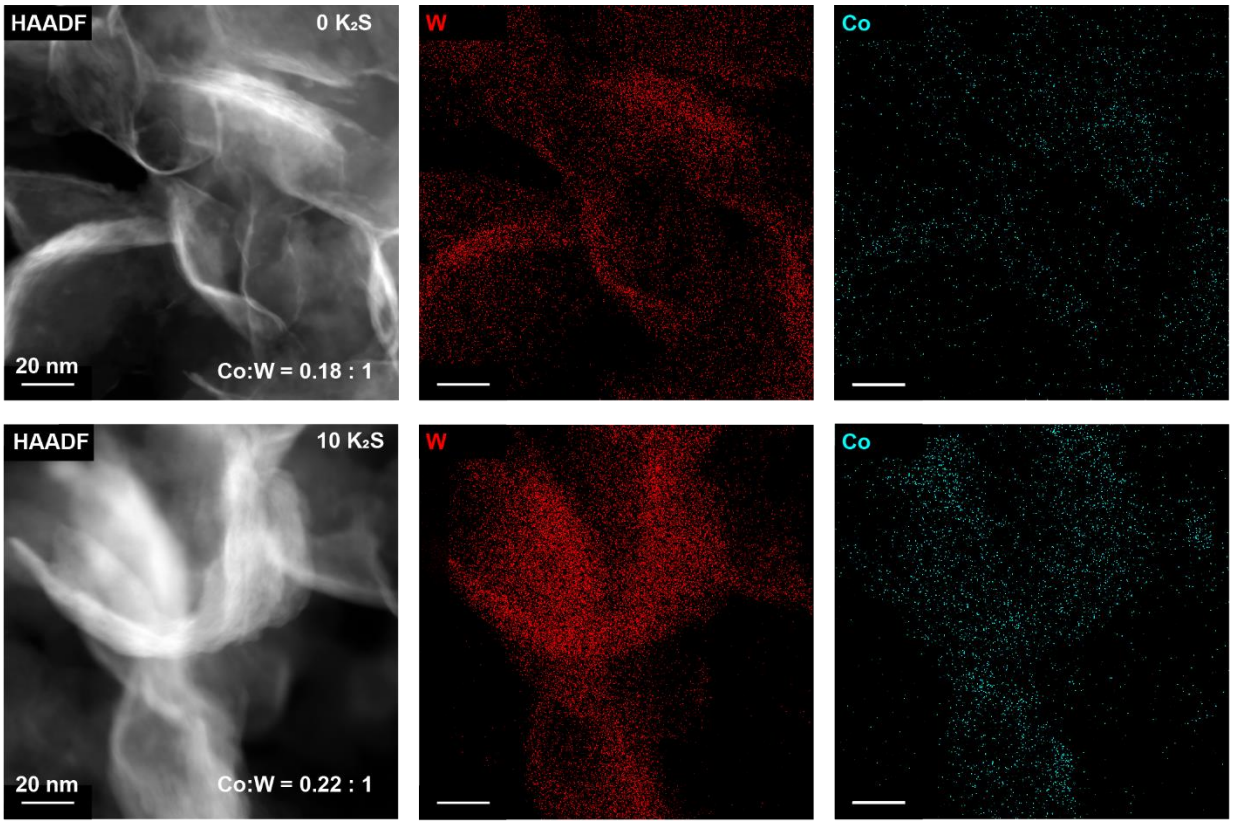

Figure 2.7. HAADF-STEM images and EDS elemental maps of W and Co for selected Co-WS_2 $x$$K_2S$ samples.

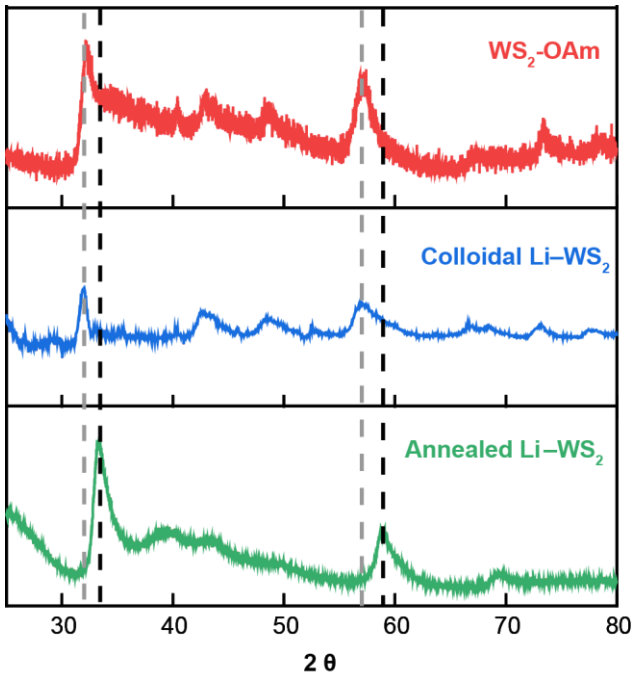

Figure 2.8. Powder X-ray diffraction patterns for WS_2 samples at various stages of the synthetic process. Reference peak positions for the 1T WS_2 (dotted grey) and 2H WS_2 (dotted black) provided based on the literature.

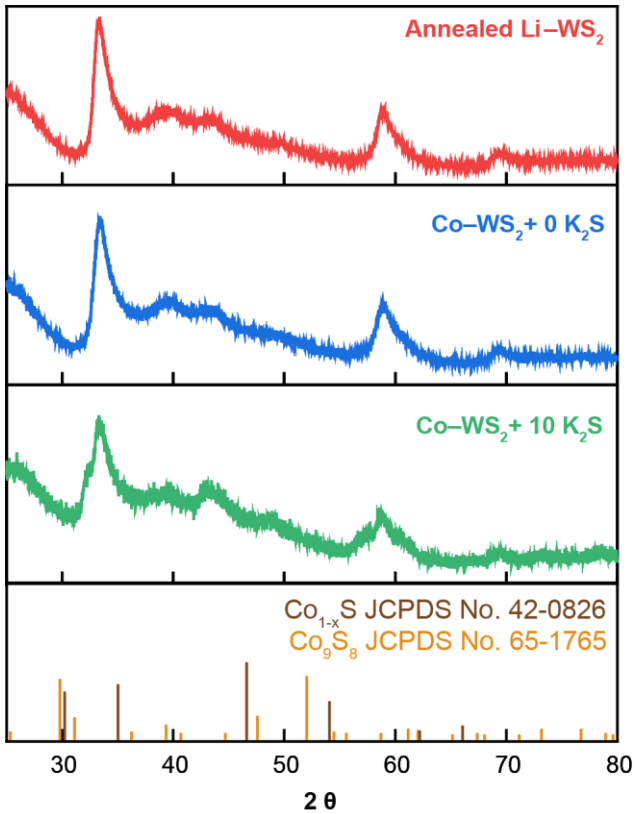

Figure 2.9. Powder X-ray diffraction patterns for annealed Li-WS_2, Co-WS_2 annealed with 0 eq. and 10 eq. K_2S. No peaks corresponding to crystalline cobalt sulfide phases are observed.

2.3.3 X-ray Absorption Spectroscopy

Using Co K-edge X-ray absorption spectroscopy (XAS), we are able to characterize both the electronic state and coordination environment of the adsorbed Co atoms in the as-synthesized and K_2S-treated Co-WS_2 samples. These spectra were compared to the precursor molecular complex, $Co(NMF)_xCl_2$, as well as a control sample of amorphous cobalt sulfide (CoS_x) with an approximate composition of $CoS_{1.2}$ (Figure 2.10, 2.11).[23,24] Fitting of the Fourier-transformed X-ray absorption fine structure (EXAFS) data was carried out on a subset of samples that showed sufficient Co K-edge absorption, and coordination numbers (CN) and bond distances (R) for both Co-O and Co-S scattering were obtained. Full fitted parameters and fitted data are provided in Table 2.2.

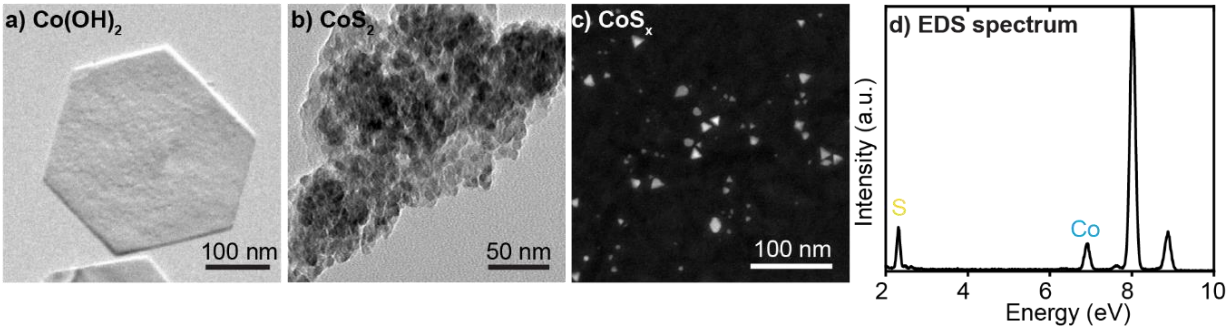

Figure 2.10. TEM images for Co control samples: **(a)** $Co(OH)_2$ nanosheets (150-300 nm); **(b)** CoS_2 nanoparticles (100-220 nm); **(c)** amorphous CoS_x nanoparticles (5-50 nm); **(d)** EDS spectrum for CoS_x showing a Co:S ratio of 1:1.2.

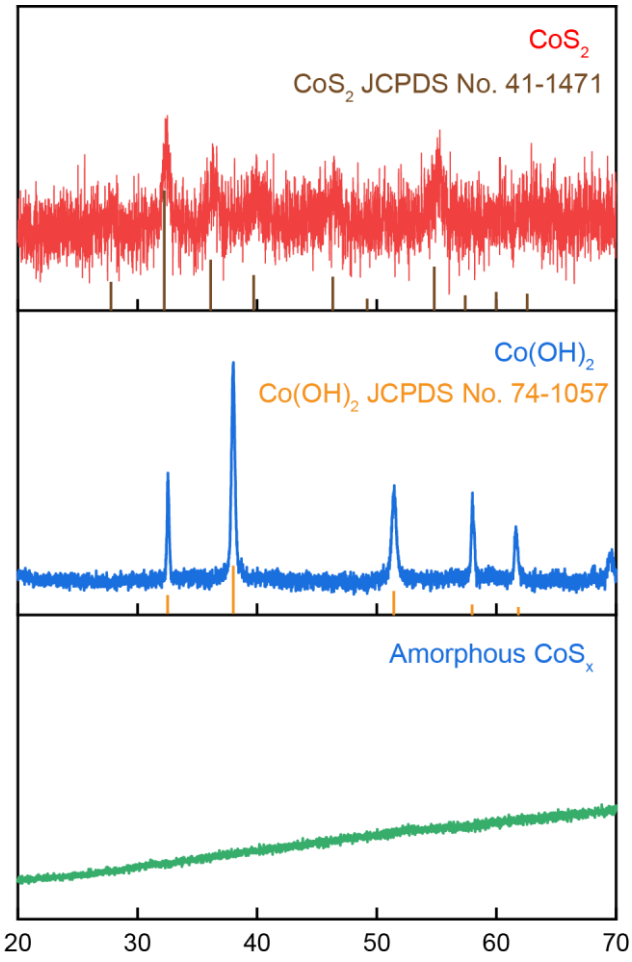

Figure 2.11. Powder X-ray diffraction patterns for control samples CoS_2 (red), $Co(OH)_2$ (blue), and amorphous CoS_x (green).

Table 2.2. Summary of EXAFS best fit parameters at the Co K-edge on Co-WS_2 samples and Co reference samples.

Sample	**XANES Energy (eV)**	**Scattering Pair**	**CN**	**R (Å)**	**E_0 (eV)**	**σ^2 (Å^2)**
Co Foil	7709	Co–Co	12.0 ± 0.057	2.50 ± 0.003	8.7 ± 0.437	0.007 ± 0.0003
$Co(OH)_2$	7722	Co–O	6.4 ± 0.42	2.10 ± 0.006	–2.7 ± 0.50	0.004 ± 0.001
		Co–O–Co	5.9 ± 0.57	3.17 ± 0.007		
$Co(NMF)_xCl_2$	7721	Co–O	6.0 ± 0.46	2.08 ± 0.007	–2.3 ± 0.86	0.004 ± 0.001
Co-WS_2 0.5K_2S	7718	Co–O	3.8 ± 0.15	2.10 ± 0.004	7.4 ± 0.28	0.004 ± 0.0004
		Co–S	2.5 ± 0.11	2.25 ± 0.004		
Co-WS_2 3K_2S	7718	Co–O	1.7 ± 0.36	2.10 ± 0.022	3.3 ± 0.59	0.004 ± 0.001
		Co–S	3.9 ± 0.27	2.25 ± 0.006		
1.1Co-WS_2 3K_2S Post-PBS	7717	Co–S	4.6 ± 0.27	2.25 ± 0.005	–4.9 ± 0.60	0.004 ± 0.001

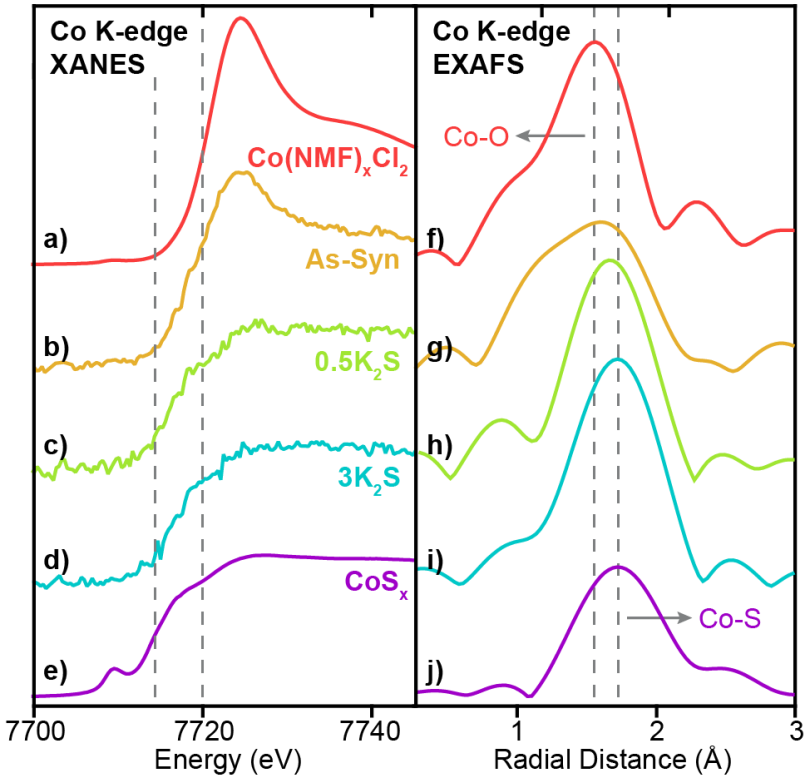

Figure 2.12. Co K-edge XANES and EXAFS spectra for **(a, f)** $Co(NMF)_xCl_2$, **(b, g)** As-synthesized Co-WS_2, **(c, h)** Co-WS_2 annealed with 0.5 equiv. of K_2S, **(d, i)** Co-WS_2 annealed with 3.0 equiv. of K_2S, **(e, j)** amorphous CoS_x. Dotted lines indicate the edge energies or scattering peaks for Co-O and Co-S coordination.

The X-ray absorption near edge spectroscopy (XANES) data for the precursor $Co(NMF)_xCl_2$ complex exhibits Co K-edge energy of 7721 eV and high white line intensity, consistent with a Co^{2+} ion primarily coordinated to oxygen atoms, as anticipated for a $CoCl_2$ precursor dissolved in the coordinating solvent N-methylformamide (NMF) (Figure 2.12a).[49] Likewise, the EXAFS shows a scattering peak at a short radial distance due to pure Co-O coordination (Figure 2.12f). Fitting of the EXAFS data shows a Co–O bond length of 2.08 Å with CN ~6, consistent with an octahedral molecular complex (Table 2.2). On the opposite end of the spectrum, amorphous CoS_x exhibits a completely suppressed XANES white line and a significantly lower Co K-edge energy of 7714 eV with a strong pre-edge feature at 7710 eV, indicative of mixed tetrahedral and octahedral coordination (Figure 2.12e).[50] Compared to Co–O coordination, Co-S coordination generates a scattering pathway at higher radial distance due to the longer average bond length, which range from 2.18 to 2.45 Å in known bulk phases of cobalt

sulfide (Figure 2.12j, Table 2.3). The XANES and EXAFS of these two control samples serve as bookends for the Co-WS_2 samples treated with varying amounts of sulfur because we expect the first-shell coordination environment to transform from oxygen-rich to sulfur-rich with increasing K_2S loading.

Table 2.3. Summary of theoretical bond lengths and coordination numbers for CoO and CoS_x phases based on known crystal structures. The .cif files used to generate these parameters were obtained from the database ICSD.[51-56]

Sample	Scattering Pair	CN	R (Å)
CoO	Co-Co	6	2.13
$CoCl_2$	Co-Cl	6	2.45
CoS	Co-S	6	2.34
CoS_2	Co-S	6	2.32
Co_3S_4	Co-S (T_d)	4	2.18
	Co-S (O_h)	6	2.27
Co_9S_8	Co-S (T_d)	4	2.21
	Co-S (O_h)	6	2.39

In the as-synthesized Co-WS_2 sample, we observe small perturbations to the adsorbed Co coordination environment relative to the free $Co(NMF)_xCl_2$ complex. A drop in white line intensity in the XANES and a small shift to longer radial distance for the first Co–X (X = O or S) scattering pathway relative to the free complex are both indicative of an increase in the number of sulfur atoms relative to oxygen atoms in the first coordination sphere (Figure 2.12b, g). However, the persistence of the peak in the white line intensity indicates that Co atoms remain primarily oxygen-bound in this form when passively-adsorbed to the Li-WS_2 nanosheet in the solution phase. These data are consistent with the observation of Co atoms bound in S-Top sites and W-Top sites adjacent to vacancies in the high-resolution STEM images. We postulate that the complex likely binds in a mono- or bidentate fashion to dangling sulfur sites on the lithiated WS_2 surface, and the remaining coordination sites remain occupied by NMF ligands.

Upon K_2S impregnation and annealing, the XAS data shows a significant increase in the Co–S coordination to the WS_2 surface. Treatment with 0.5 equiv. or 3 equiv. of K_2S completely suppresses the sharp white line feature diagnostic of Co^{2+}–O binding and shifts the Co K-edge energy downwards by 3 eV, approaching the edge energy of the CoS_x control sample (Figure 2.12c-d). The EXAFS scattering peak also shifts to longer radial distance, and the sample treated with 3 equiv. K_2S essentially matches the peak position of CoS_x (Figure 2.12h-j). Fitting of the EXAFS data indicates that the Co–S CN increases steadily from 2.5 at 0.5 equiv. K_2S up to 3.9 at 3 equiv. K_2S while the Co-O CN drops correspondingly (Table 2.2). In all of these samples, no scattering density is observed beyond 3.0 Å, indicating that Co atoms remain relatively isolated on the WS_2 surface even after thermal annealing (Figure 2.13). Together, these data show that Co atomic coordination to the WS_2 surface can be readily controlled in the doped Co-WS_2 system simply by varying the amount of impregnated K_2S, providing an ideal model system to understand the role of Co–S coordination environment in catalysis.

2.3.4 Oxygen Reduction Reaction

Literature studies have shown that first-row transition metal sulfides are uniquely suitable catalysts for the ORR in neutral media due to their greater resistance to electrolyte poisoning and dissolution compared to noble metals and base metal oxides, respectively.[57-59] Recent DFT studies have revealed that the ORR activity of nickel sulfide catalysts of varying phase and composition is closely tied to the Ni–S coordination number at the surface of the bulk phase.[24] We hypothesized that our Co-doped WS_2 samples, with systematically variable Co–S coordination number, would be an ideal materials platform to probe the role that metal-sulfur coordination environment plays in pH 7 ORR reactivity.

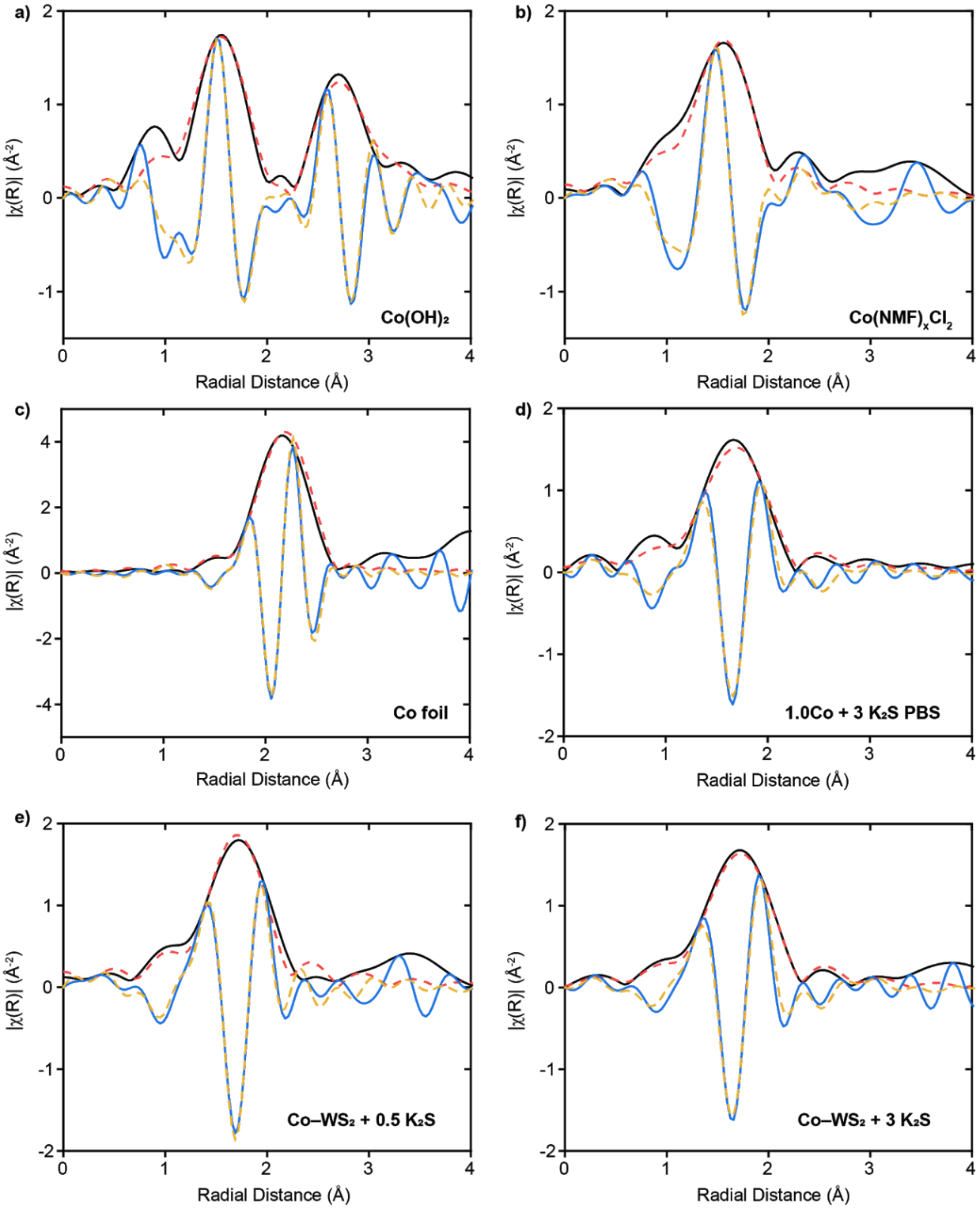

Figure 2.13. Co K-edge EXAFS fits (dotted) overlaid with experimental data (solid) in R-space for the k^2-weighted Fourier transform data including both the FT-magnitude and real portion. **(a)** bulk $Co(OH)_2$, **(b)** $Co(NMF)_xCl_2$ molecular complex, **(c)** cobalt foil, **(d)** 1.0Co-WS_2 + 3 eq. K_2S treated with PBS, **(e)** Co-WS_2 annealed with 0.5 eq. K_2S, and **(f)** Co-WS_2 annealed with 3 eq. K_2S.

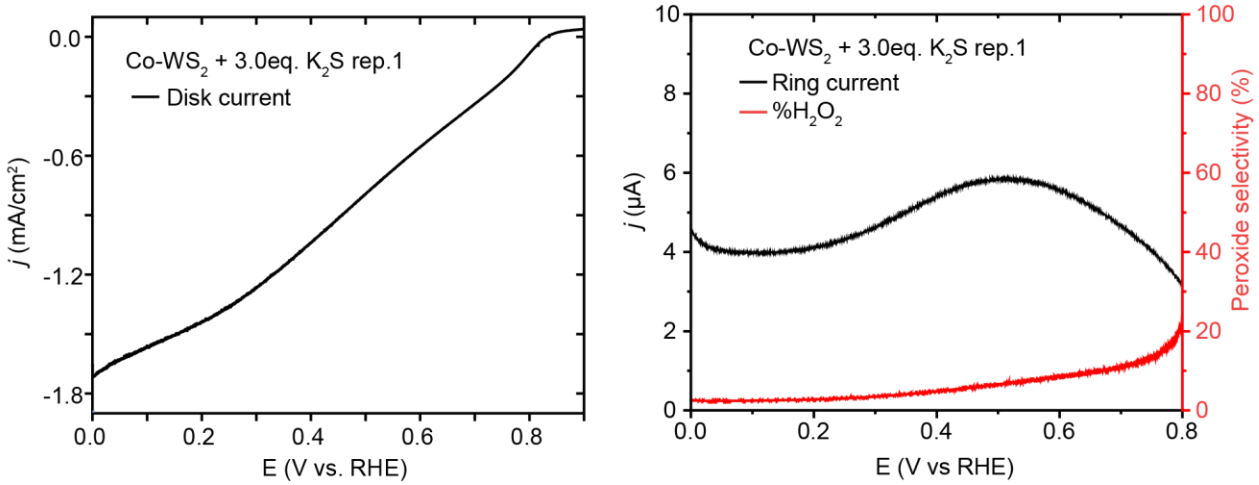

Figure 2.14. ORR LSV data showing the disk current density (left) and ring current and peroxide selectivity (right) for the Co-WS_2 $3K_2S$ catalyst.

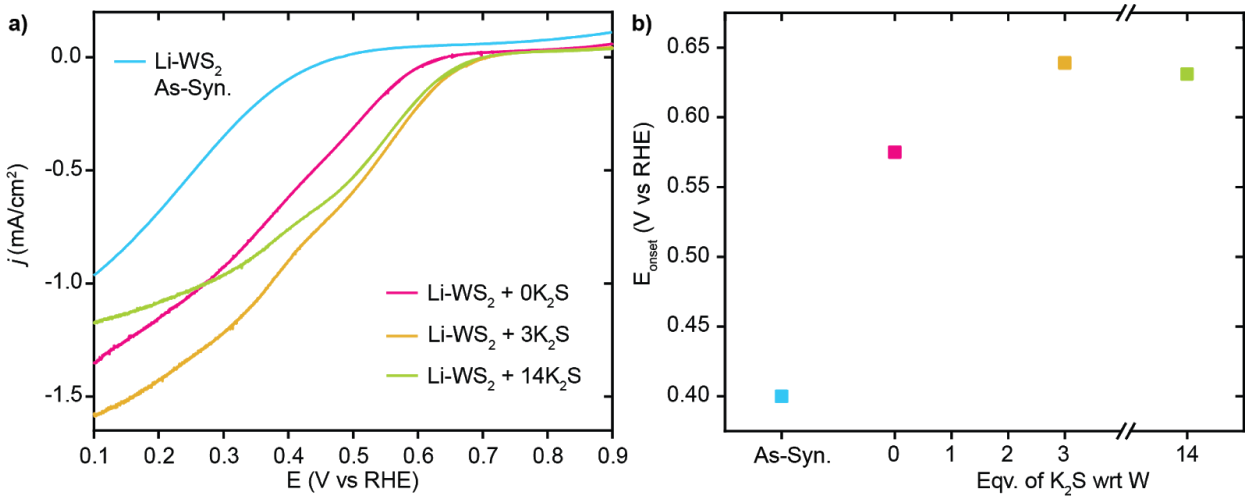

Figure 2.15. ORR data for Li-WS_2 as-synthesized and sulfur annealed variants. **(a)** 1st scan LSV data and **(b)** E_{onset} vs. as-synthesized equivalents of impregnated K_2S.

Table 2.4. Summary of ORR onset potentials (E_{onset}) for Co-WS_2 samples treated with varying equivalents of K_2S as well as control samples.

Sample	***x*K_2S (Eq. wrt Co)**	**[a]E_{onset} (V) @ -0.1 mA cm^{-2} 1st scan**	**Onset (V) @ -0.1 mA cm^{-2} 5th scan**
Li-WS_2	0	0.575 ± 0.011	0.571
	3.0	0.639 ± 0.005	0.634
	14.0	0.631	0.596
Co-WS_2 + *x*K_2S	0	0.614 ± 0.011	0.581
	0.5	0.668 ± 0.003	0.634
	1.0	0.698 ± 0.006	0.663
	3.0	0.798 ± 0.003	0.794
	6.0	0.770 ± 0.003	0.752
	10.0	0.731 ± 0.004	0.709
$Co(OH)_2$/C	0	0.516	---
	0.4	0.615	---
	0.8	0.554	---
CoS_x/C	n/a	0.767	---
CoS_x + WS_2 (physical mixture)	n/a	0.574	---
$CoCl_2$ + WS_2 (physical mixture)	n/a	0.414	---

[a]Average values and standard deviations obtained from three independent runs.

The ORR catalytic activity of all samples was measured using linear scan voltammetry (LSV) on a rotating ring-disk electrode in O_2-saturated 1 M phosphate buffer solution (PBS, pH = 7). Negligible ring current is detected using any of the Co-WS_2 catalysts, which indicates quantitative selectivity toward the 4 e^- reduction of O_2 to H_2O under these conditions (Figure 2.14). In order to compare the reactivity of various Co-WS_2 and bulk control samples to one another, we utilize the ORR onset potential (E_{onset}), the potential at which the catalyst attains –0.1 mA/cm^2 of ORR current density, as the primary catalytic metric due to differences in sample mass-transport properties at higher current densities.

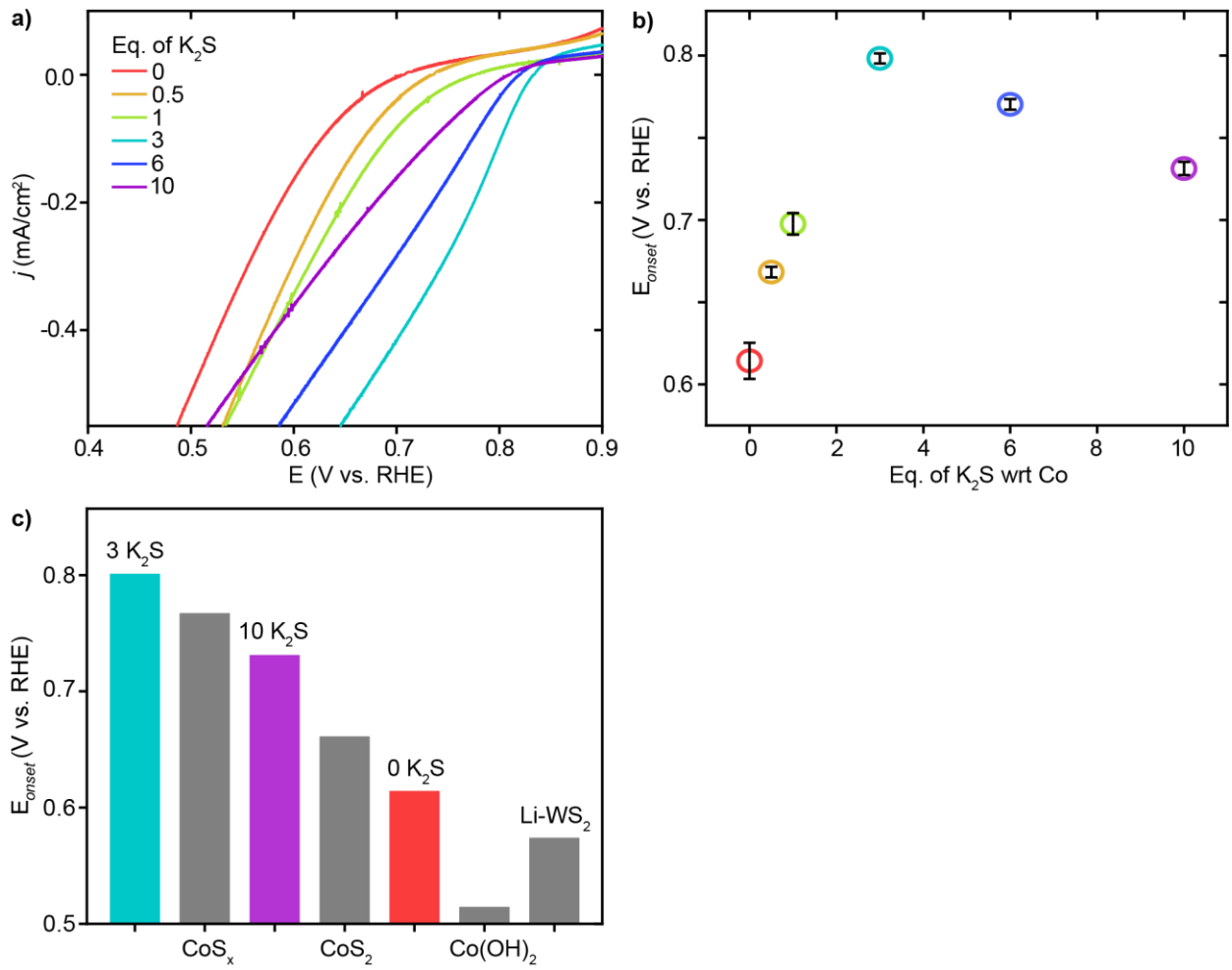

Figure 2.16. Oxygen reduction reaction activity in O_2-saturated 1 M PBS (pH = 7) electrolyte. **(a)** ORR LSVs for the full series of Co-WS_2 samples treated with K2S, **(b)** Co-WS_2 E_{onset} vs. equivalents of K_2S, **(c)** E_{onset} for annealed Li-WS_2, bulk Co phases, and Co-WS_2 at varying degrees of sulfidation.

The annealed Li-WS_2 nanosheets alone show poor ORR activity with an onset potential (E_{onset}) of 0.575 V vs. RHE (Figure 2.15, Table 2.4). The addition of Co to the WS_2 sample in the absence of K_2S (0 K_2S) induces a modest increase in ORR onset potential to 0.614 V vs RHE (Figure 2.16a-b, 2.17, Table 2.4). Introduction of varying equivalents of K_2S to the Co-WS_2 sample has a dramatic effect on ORR catalysis. Upon mild sulfidation at 0.5 equiv. K_2S, the onset potential for ORR immediately increases by 54 mV to 0.668 V vs. RHE. From 0.5 to 3.0 equiv. of K_2S relative to Co, a steady increase in ORR onset potential is observed with the highest E_{onset} of 0.798 V vs. RHE occurring at 3.0 equiv. K_2S. Further increase in K_2S loading causes a decay in the ORR activity, dropping back down to 0.731 V vs. RHE at 10 equiv. K_2S. A modest improvement in

catalytic activity is also observed when Li-WS_2 alone is annealed in the presence of excess sulfur (Figure 2.15, Table 2.4). However, the onset potential of Li-WS_2 peaks at 0.639 V vs. RHE in the absence of doped Co atoms.

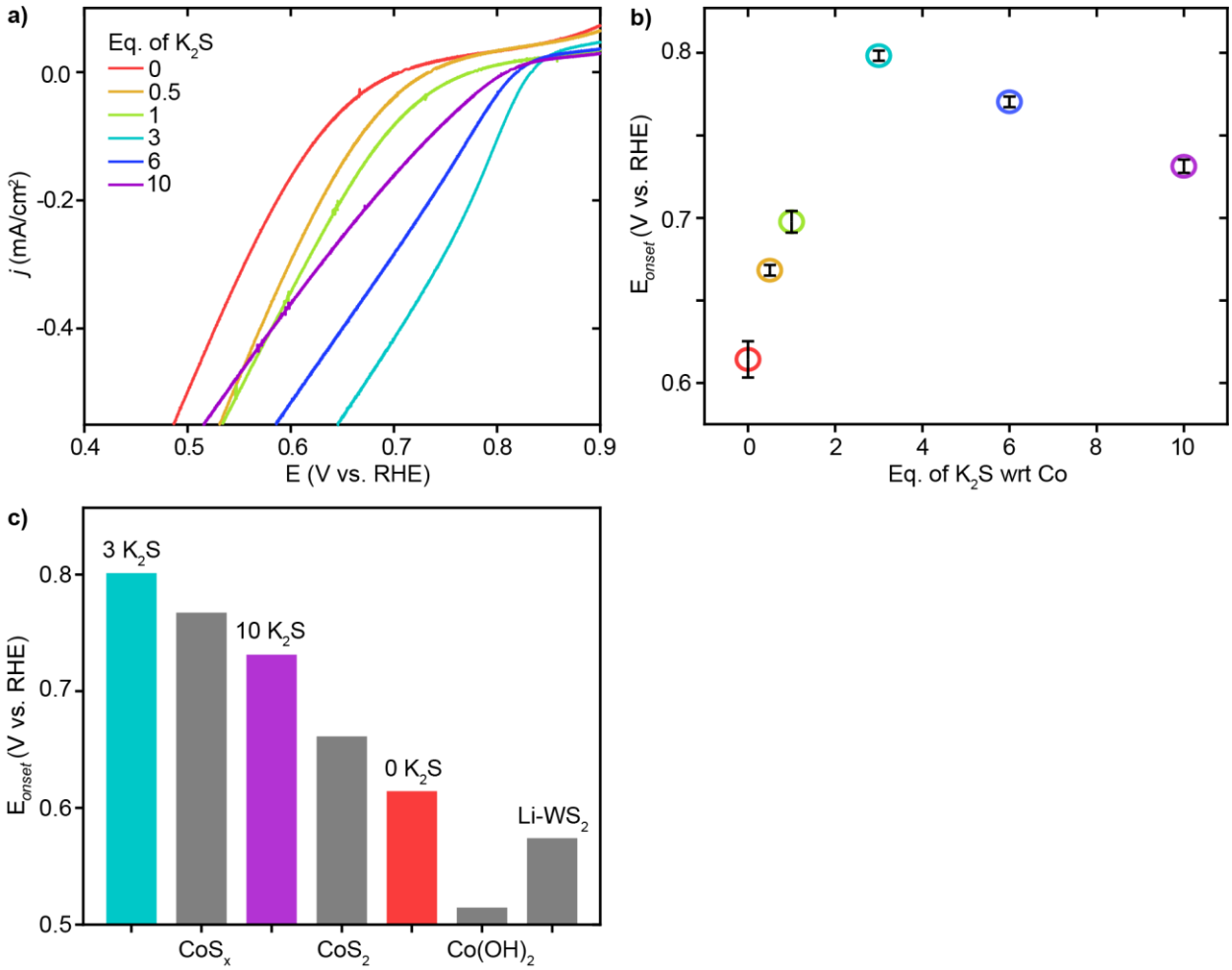

Figure 2.17. Oxygen reduction reaction activity in O_2-saturated 1 M PBS (pH = 7) electrolyte. **(a)** ORR LSVs for the full series of Co-WS_2 samples treated with K2S, **(b)** Co-WS_2 E_{onset} vs. equivalents of K_2S, **(c)** E_{onset} for annealed Li-WS_2, bulk Co phases, and Co-WS_2 at varying degrees of sulfidation.

As a comparison to our doped materials, we also obtained ORR catalytic data on three Co-containing phases with very different bulk composition and local Co coordination environment: $Co(OH)_2$, amorphous CoS_x (~$CoS_{1.2}$), and CoS_2 (Figure 2.10, 2.11). The $Co(OH)_2$ nanosheets with pure Co-O coordination show the poorest ORR onset potential of 0.514 V vs. RHE (Figure 2.16c, 2.17, Table 2.4). Even the Co-WS_2 sample treated with 0 equiv. K_2S is substantially more active

due to the interaction with and contribution of the underlying WS_2 nanosheets. The amorphous CoS_x sample with an intermediate S:Co ratio of ~1:1 shows the highest E_{onset} among the bulk phases at 0.767 V vs. RHE, nearly matching the onset potential of the optimal Co-WS_2 3K_2S catalyst. The most sulfur-rich sample, comprising CoS_2 nanoparticles, exhibits lower ORR activity with an onset potential of 0.661 V vs. RHE, which mirrors the drop in activity of Co-WS_2 when it becomes over-coordinated to sulfur. The similar trends in onset potential as a function of cobalt sulfidation between Co-WS_2 and bulk Co-containing phases provides an initial indication that the local coordination environment identified for isolated Co atoms supported on WS_2 may also apply to the active sites formed *in-situ* on the surface of bulk cobalt sulfide species during ORR catalysis.

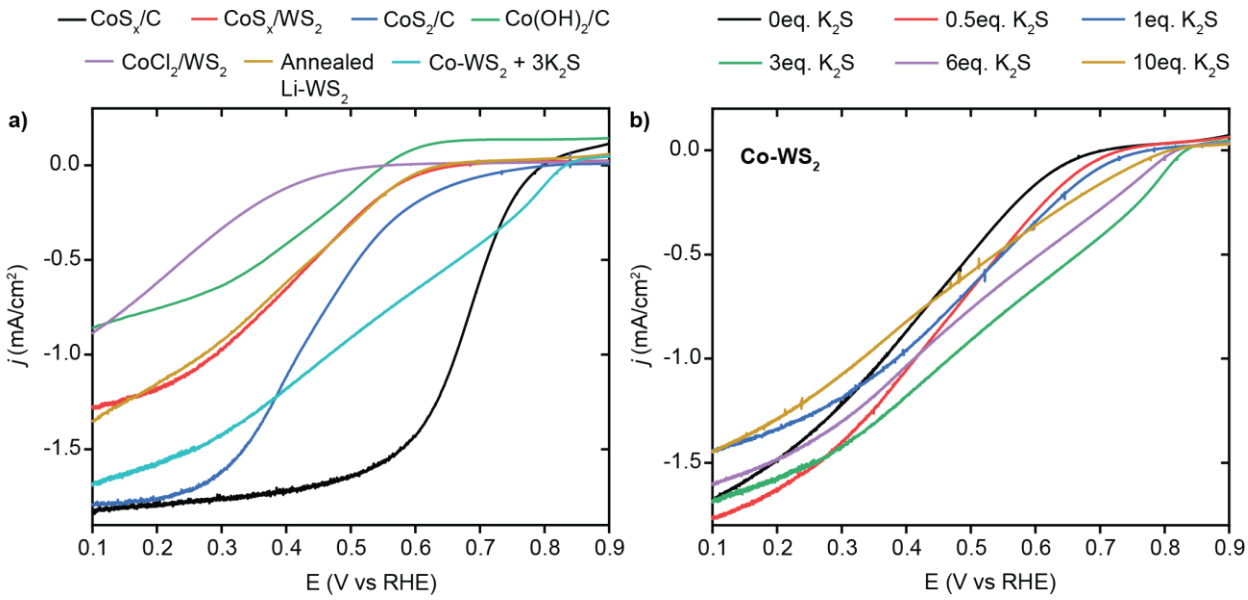

Figure 2.18. **(a)** 1st scan ORR LSV data for Co-WS_2 3K_2S and control samples including: CoS_x/C, CoS_2/C, $Co(OH)_2$/C, physical mixtures of WS_2 + CoS_x or $CoCl_2$, and annealed Li-WS_2. **(b)** Full 1st scan ORR LSV data for all Co-WS_2 *x*K_2S samples.

We can correlate the initial ORR activity on the single-atom Co-WS_2 samples back to the pre-catalysis XAS structural characterization presented above because, unlike in bulk or nanoparticle cobalt sulfide materials, all Co atoms in Co-WS_2 are available on the surface for catalysis. We find that Co-WS2 treated with 3 equiv. K_2S, exhibiting three- to four-fold coordination of Co to sulfur atoms on the WS_2 surface, provides an optimal electronic and geometric environment for pH 7 ORR catalysis. We hypothesize that the activation of adsorbed Co atoms with K_2S up to 3.0 equiv. stems from the necessity for a more electron-rich metal center,

enabled by Co–S coordination, in order to reductively activate O_2. Further increasing K_2S, however, likely causes over-coordination with sulfur and therefore loss of available coordination sites for O_2 binding and activation.

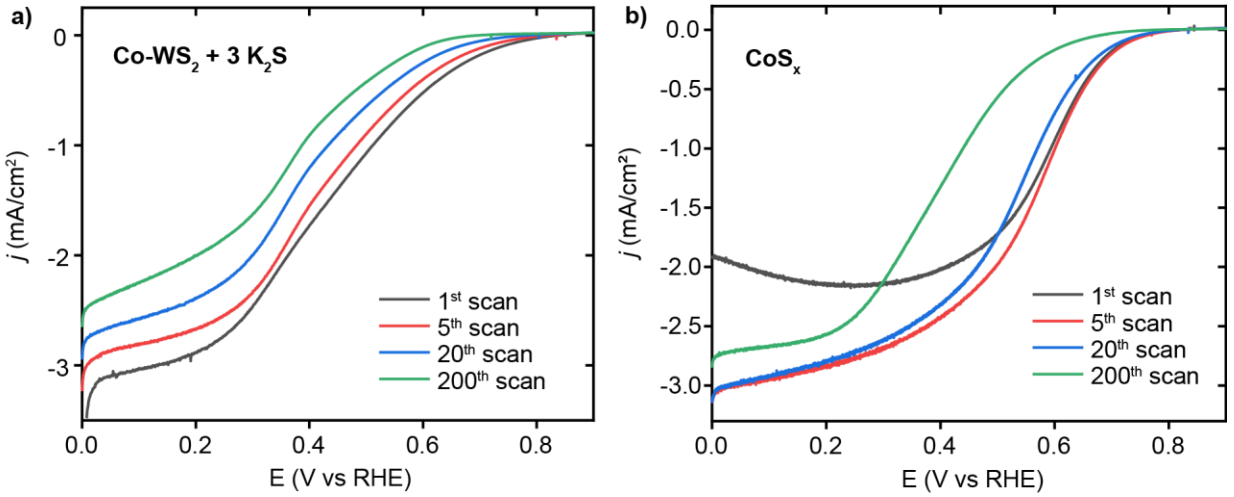

Figure 2.19. ORR stability test for **(a)** Co-WS_2 3K_2S and **(b)** amorphous CoS_x.

We also perform extended CV scanning on the Co-WS_2 3 K_2S sample and CoS_x control to better understand the structural evolution of cobalt sulfide sites during pH 7 ORR catalysis. In both cases, a small drop in onset potential is observed after 20 CV scans, and a much larger deactivation of both onset potential and mass-transport limited current density occurs after 200 CV scans (Figure 2.19). As a result, we characterized the Co-WS_2 samples after 1 hour immersion in phosphate buffer solution, catalytically equivalent to the post-catalysis material after 5-20 CV scans, to understand how the adsorbed Co sites evolve in aqueous electrolyte (Figure 2.20, Table 2.5). Elemental analysis after electrolyte treatment shows that Co loading and spatial distribution remain unchanged relative to the pre-catalysis samples (Figure 2.21a, 2.22, Table 2.6). Co K-edge XANES data on the Co-WS_2 3K_2S Post sample shows a similar edge energy but a slight increase in white line intensity relative to the pre-catalysis material (Figure 2.21b). The EXAFS spectrum also shows a small shift in the first-shell scattering peak to lower radial distance (Figure 2.21c). These data indicate that the Co–S bonds that anchor the dopants to the WS_2 surface hydrolyze slightly in the presence of aqueous electrolyte, likely causing the decay in catalytic activity. However, Co surface sites remain isolated on the WS_2 surface after the electrolyte treatment, as

evidenced by the continued absence of a second coordination sphere Co–S–Co scattering feature (Figure 2.21c).

Table 2.5. Summary of ORR onset potentials (E_{onset}) for Co-WS_2 + xK_2S samples treated in 1 M phosphate buffer solution (PBS). These onset potentials closely match those observed for the 5th LSV scan under ORR conditions.

Sample	***x*K$_2$S (Eq. wrt Co)**	**Onset (V) @ -0.1 mA cm^{-2} 1st Scan 1hr PBS**
Co-WS_2 + xK_2S + PBS	0	0.555
	1.0	0.665
	10.0	0.630

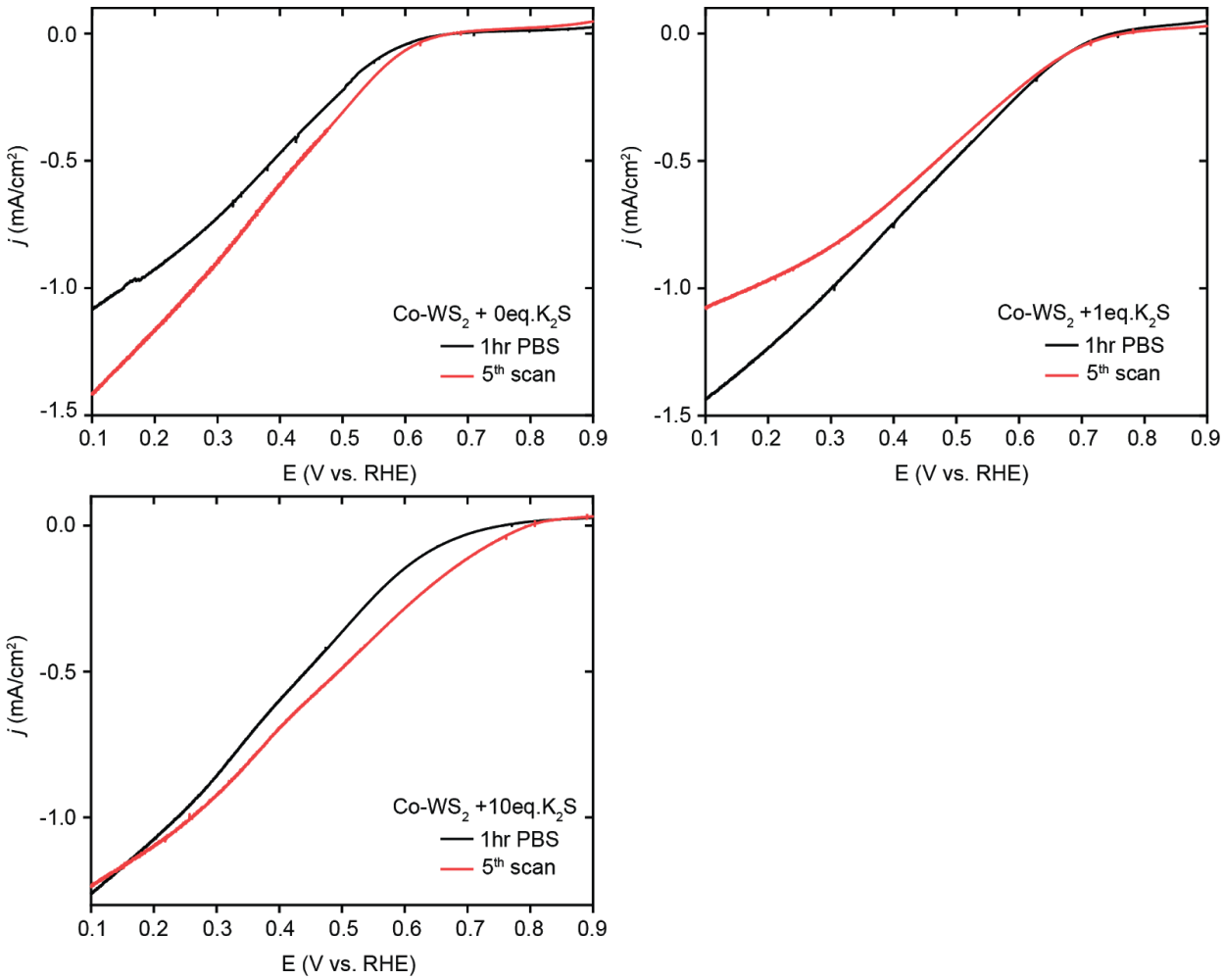

Figure 2.20. ORR 1st scan LSV data for Co-WS_2 samples + xK_2S treated in PBS compared to 5th scan LSV data for untreated samples.

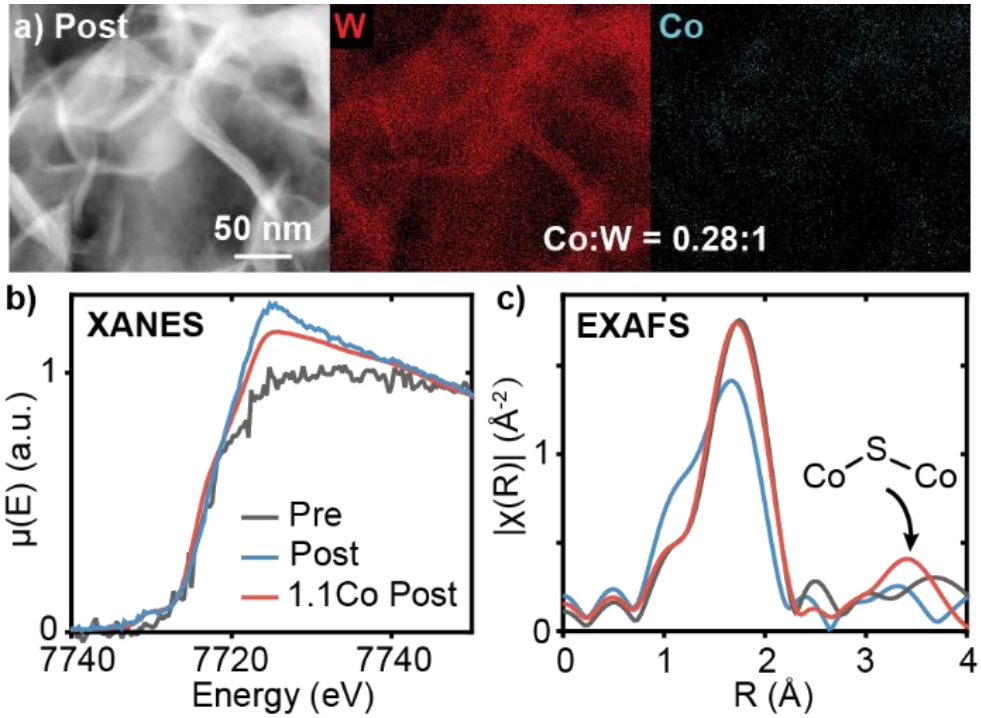

Figure 2.21. Characterization of Co-WS_2 after treatment with PBS electrolyte. **(a)** STEM images and elemental maps of W and Co, **(b)** XANES, and **(c)** EXAFS spectra. XAS data on Co-WS_2 prior to catalysis (Pre) and a high concentration Co-WS_2 (1Co-WS_2 PBS) are provided for comparison.

As a final comparison, we synthesized a Co-WS_2 sample with much higher Co loading (Co:W = 1.1:1) to intentionally generate CoS_x clusters supported on WS_2 (Figure 2.23, Table 2.7). This high loading Co-WS_2 sample (1Co-WS_2) was similarly treated with 3.0 equiv. of K_2S, annealed at 300 °C, and soaked in PBS for 1 hour. Both the Co K-edge XANES and EXAFS spectra in the first coordination sphere are quite similar to the isolated Co atoms in the lower loading Co-WS_2 sample (Figure 2.21b-c). The primary difference between the high and low-loading Co-WS_2 is in the presence of a second coordination sphere Co–S–Co scattering feature in the EXAFS due CoS_x cluster formation at the high Co loading. Intriguingly, the 1.1Co-WS_2 sample shows almost identical onset potential for ORR to the lower loading, suggesting that sulfur binding to Co in the first coordination sphere is primarily responsible for determining oxygen reduction activity (Figure 2.24).

Table 2.6. Summary of elemental analysis obtained using XRF and EDS for Co-WS_2 + xK_2S samples after PBS treatment. The tungsten M-edge and cobalt K-edge were used for both XRF and EDS quantification.

Sample	***x*K$_2$S (Eq. wrt Co)**	**XRF Co:W (X:1)**	**EDS Co:W (X:1)**
Co As-Syn	n/a	0.33	0.20 ± 0.02
Co-WS_2 + xK_2S + PBS	0	0.29	0.12 ± 0.03
	0.5	0.29	0.14 ± 0.01
	1	0.31	0.14 ± 0.02
	3	0.28	0.07 ± 0.01
	6	0.17	0.08 ± 0.03
	10	0.21	0.12 ± 0.01

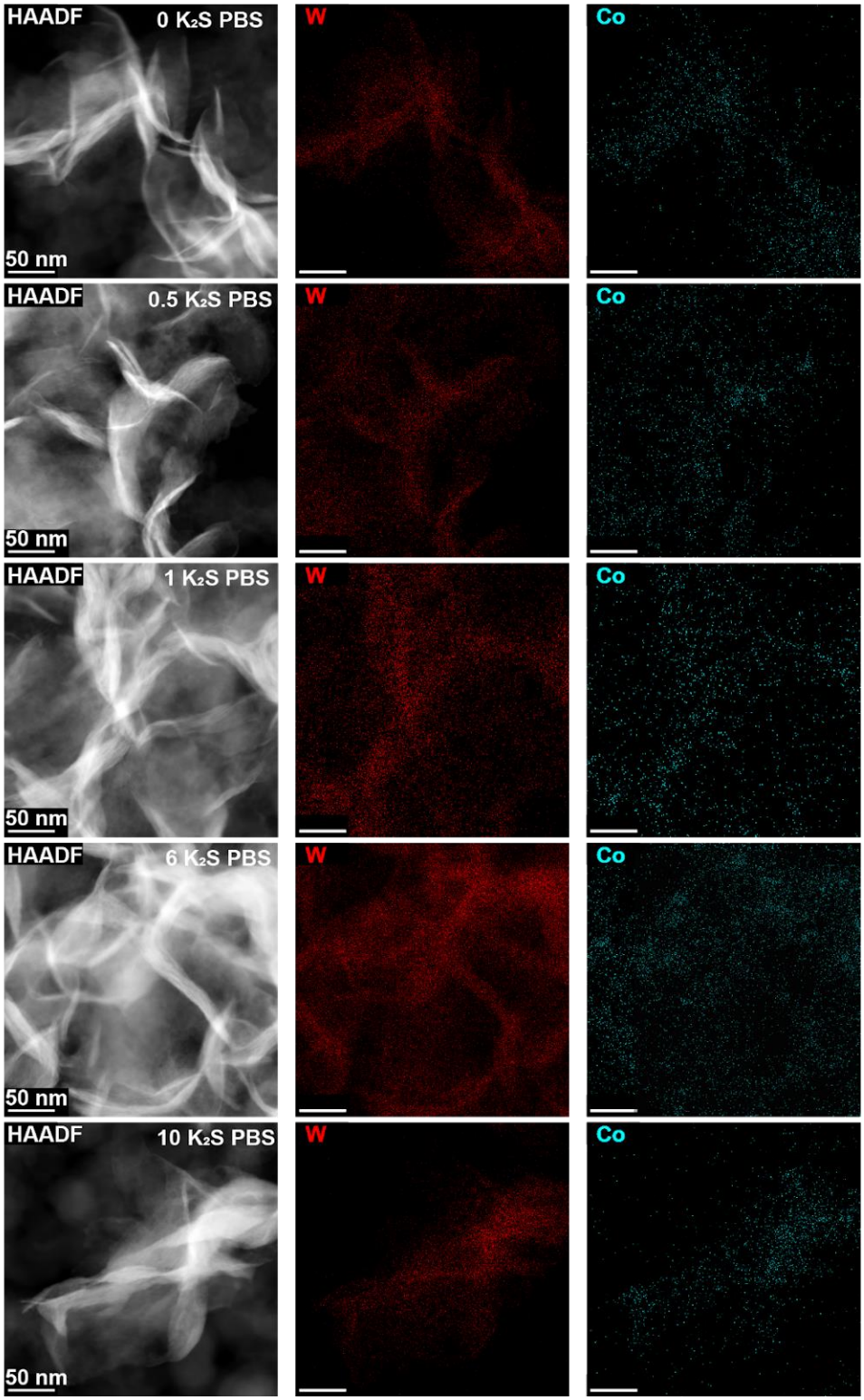

Figure 2.22. EDS mapping images of Co-WS_2 + $x$$K_2S$ samples after PBS treatment.

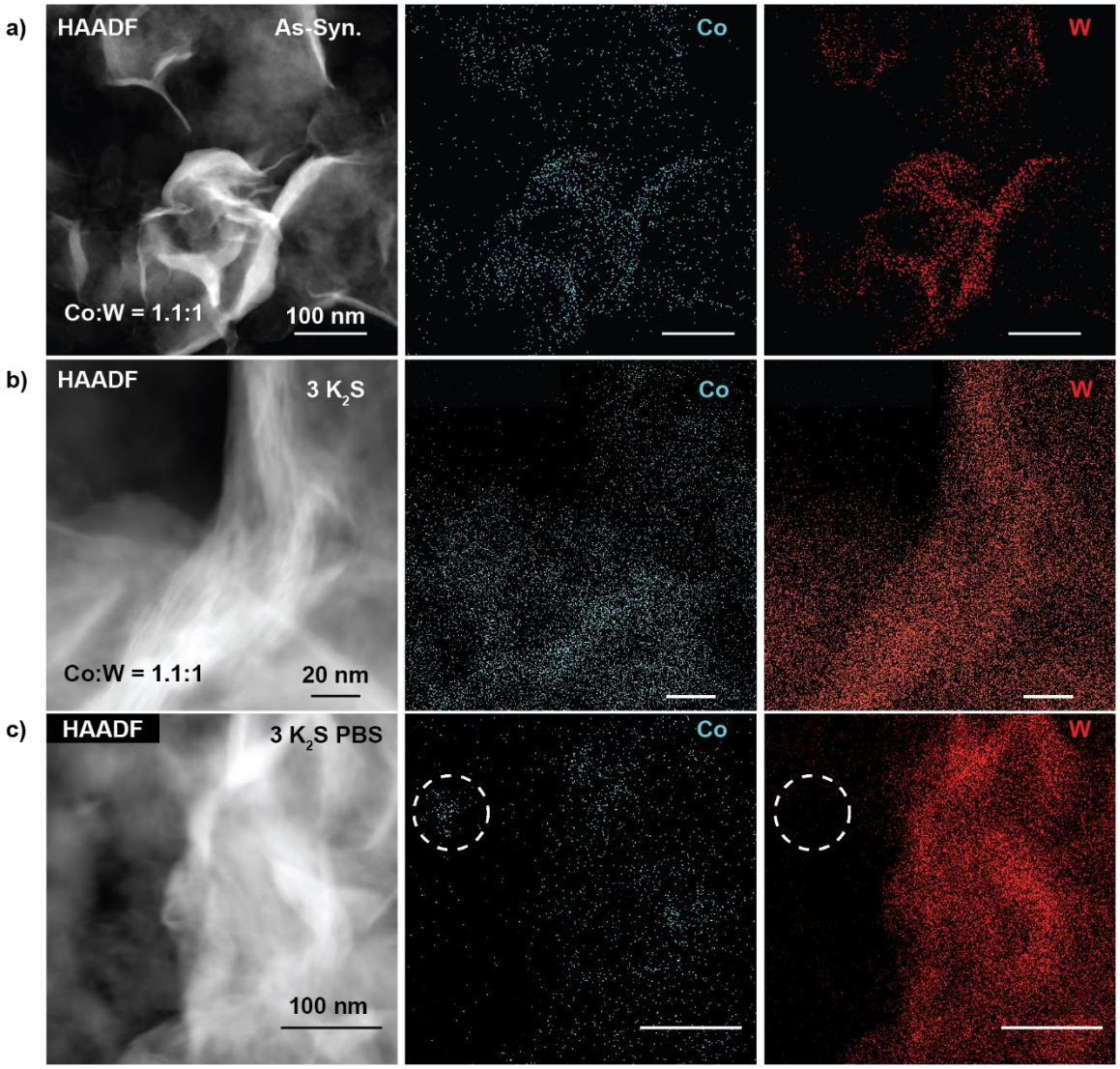

Figure 2.23. **(a)** STEM images and EDS elemental maps of **(a)** as-synthesized 1.1Co-WS_2, **(b)** 1.1Co-WS_2 after annealing with 3 eq. K_2S, **(b)** 1.1Co-WS_2 3K_2S after PBS treatment. Circled area shows a Co aggregate that is not co-localized with the underlying W.

Table 2.7. Elemental analysis obtained using EDS for the high loading 1.1Co-WS_2 samples. The tungsten M, sulfur K, and cobalt K peaks were used for quantification. EDS spectra were taken in three distinct locations for each sample.

Sample	**W at.%**	**S at.%**	**Co at.%**	**Average Co:W (X:1)**
1.1Co-WS_2 As-Syn	18	62	20	1.1 ± 0.01
	17	65	18	
	17	65	18	
1.1Co-WS_2 3K_2S*	9	80	11	1.2 ± 0.19
	13	70	17	
	13	74	13	
1.1Co-WS_2 3K_2S* Post-PBS	21	76	3	2.3 ± 3.1
	12	77	11	
	4	72	24	

*Significant heterogeneity in Co:W atomic ratio is observed in different locations on this sample.

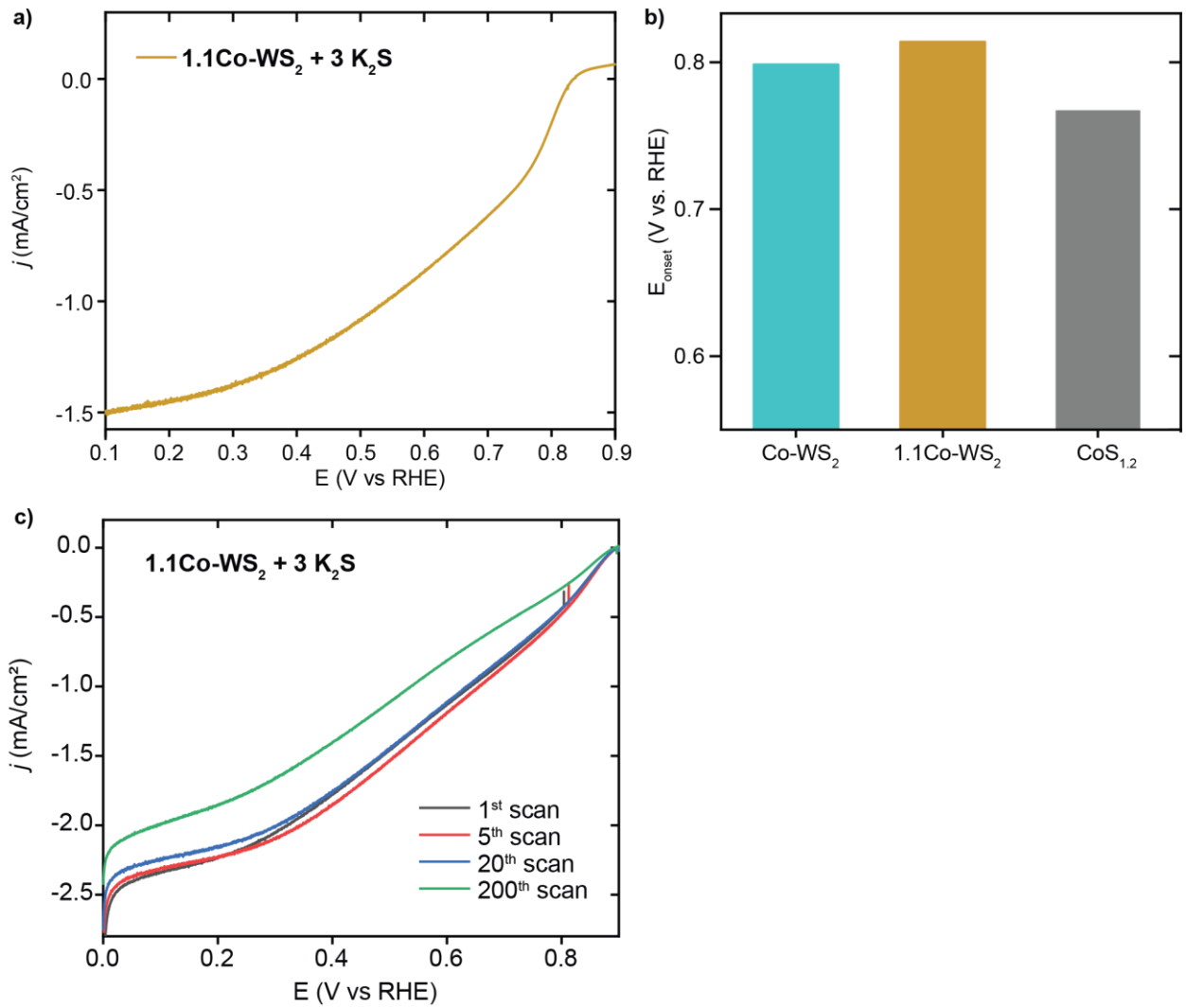

Figure 2.24. **(a)** ORR 1st scan LSV data for 1.1Co-WS_2 3K_2S. **(b)** E_{onset} for low-loading Co-WS_2 compared to high-loading 1.1Co-WS_2 and bulk CoS_x. **(c)** ORR stability test for 1.1Co-WS_2 3K_2S.

2.4 Conclusions

In conclusion, we find that Co atoms supported on WS_2 show high activity for the pH 7 ORR reaction when partially coordinated to sulfur ligands. Both undercoordination and overcoordination to sulfur prove detrimental to catalysis. The optimal Co active site comprises approximate 3-4-fold coordination to the sulfur atoms on the surface of WS_2 and two labile coordination sites occupied by oxygen-based solvent ligands. These dilute Co-WS_2 catalysts show similar catalytic activity to the most active bulk phases of cobalt sulfide with an onset potential for ORR of 0.798 V vs. RHE in phosphate buffer electrolyte. Unlike bulk CoS_x systems, however, the majority of Co atoms in dilute Co-WS_2 are available for catalysis, and the Co coordination

environment obtained by XAS is representative of catalytically active sites. As a result, we postulate that the optimal coordination environment ascertained herein may be representative of the dynamic surface sites present *in situ* on the surfaces of bulk cobalt sulfide systems. The activity of single atom Co-WS_2 clearly illustrates that the electronic and geometric environment created by Co-S bonds in the first coordination sphere provides a key descriptor for ORR catalysis in cobalt sulfide materials.

2.5 Experimental Methods

2.5.1 Materials

Tungsten(VI) chloride (99.9+%, trace metal basis) and cobalt(II) chloride hexahydrate (98%) were purchased from ACROS Organics. Cobalt(II) chloride anhydrous (97%) and anhydrous n-hexanes were purchased from Alfa Aesar. Carbon disulfide (Spectranalyzed™), hexanes (certified ACS), 2-propanol (certified ACS plus), cobalt(II) nitrate hexahydrate (99%), tungsten disulfide (99.8%, metal basis), thiourea (99+%, for analysis), butanol and diethyl ether were purchased from Fisher Scientific. Carbon black (Ketjenblack EC-300J) was purchased from FuelCellStore. Sodium phosphate dibasic (analytical reagent, 99%) and sodium phosphate monobasic (analytical reagent, 99%) were purchased from Mallinckrodt Chemicals. Oleylamine (technical grade, 70%), oleic acid (technical grade, 90%), N-methylformamide (99%), trioctylphosphine (97%), 5 wt.% Nafion solution, *n*-butyllithium solution (1.6 M in hexanes), potassium polysulfide (≥42% K_2S basis), sodium hydroxide (ACS reagent, 97%), sodium hydroxide pellets (semiconductor grade, 99.99% trace metal basis), and 1-dodecanethiol (98%) were purchased from Sigma-Aldrich. Sodium dihydrogen phosphate monohydrate (99.9%-Na) was purchased from Strem Chemicals, Inc. Triethylamine (99.5% min) was purchased from Thomas Scientific. Ethanol (200 proof) was purchased from Decon Labs, Inc. All chemicals were used without further purification. Electrolyte solutions were prepared from Nanopure water (ASTM Type I, 18.2 MΩ), purified using a Thermo Scientific Barnstead Ultrapure Water System.

2.5.2 Synthesis of 1T-WS_2 nanosheets

The synthesis of 100 nm 1T-WS_2 nanosheets is based upon a literature procedure.[46] A 3-neck round bottom flask was charged with 60 mL of oleylamine (OAm), which was degassed

under vacuum at 65 °C for 1 hour and then heated to 320 °C under inert atmosphere. Separately, four vials, each containing WCl_6 (50 mg, 0.125 mmol) suspended in 300 µL of oleic acid (OA), were sonicated until fully dissolved. The vials were purged with N_2, and CS_2 (240 µL, 3.97 mmol) and OAm (5 mL) were added to each solution. The WCl_6 and CS_2 precursor solutions were then injected dropwise (10 mL/hr) into the hot OAm solution at 320 °C. The reaction medium was then removed from heat and cooled to room temperature. To purify the nanosheets, hexanes (60 mL) and isopropanol (60 mL) were added, and the solution was centrifuged at 8700 rpm for 10 min. After the supernatant was decanted, the solid was resuspended in hexanes with triethylamine (6.8 mL, 49.2 mmol) in order to fully remove adsorbed sulfur impurities. The triethylamine addition is also critical to maintaining colloidal stability and synthetic reproducibility during the next step of the synthesis. The nanosheets were again precipitated with isopropanol and centrifuged. The solid was collected and dried under vacuum for 15 minutes, and the dried nanosheets were stored under inert atmosphere as a powder.

2.5.3 Synthesis of Co-doped WS_2 nanosheets (Co-WS_2):

The n-BuLi activation and solution-phase Co adsorption methods are adapted from our previous report on Ni-doped WS_2.[2] To the dried WS_2 nanosheets (26.2 mg, 0.007 mmol), a 0.1 M solution of *n*-BuLi in hexanes (10 mL) was added under inert atmosphere and stirred for 2 hours. The Li-treated nanosheets (Li-WS_2) were then rinsed with excess hexanes and redispersed in NMF. To a 1 mL solution of Li-WS_2, a Co precursor solution (30 uL of 70 mM $CoCl_2$ in NMF) was then added and stirred for 24 hours at room temperature under nitrogen. After the Co functionalization step, the nanosheets were precipitated with ethanol (10 mL) and hexanes (20 mL) followed by centrifugation at 8700 rpm for 10 minutes. The supernatant was decanted and the cleaning step was repeated one time.

2.5.4 K_2S Impregnation and Annealing Treatment for Co-WS_2.

The nanosheets were first supported on carbon black by mixing 1 mL of a 7 mM solution of Co-WS_2 nanosheets with 11.6 mg carbon in 4 mL ethanol at room temperature. The supported Co-WS_2 samples were centrifuged at 8700 rpm for 10 min. and resuspended in 2 mL of ethanol:IPA (v:v; 1:3) solution. Next, varying amounts of K_2S solution (70 mM K_2S in EtOH) was

added, ranging from 0.5 eq. (15 uL) to 10 eq. (300 uL) with respect to Co. The mixture was left stirring in air at room temperature for 24-36 hours until the solvent fully evaporated. The dried powder was then annealed at 300 °C for 2 hours under N_2. After annealing, the sample was successively rinsed with ethanol, water, and IPA to remove unincorporated K_2S.

2.5.5 Synthesis of Co_9S_8

Synthesis of Co_9S_8 nanocrystals was carried out following a previously reported procedure.[60] To a 50 mL three-neck flask, $CoCl_2$ (32.8 mg, 0.25 mmol) and trioctylphosphine (5 mL) were added. Next, dodecanethiol (5 mL) and OAm (5 mL) were injected into the three-neck flask with vigorous stirring. The three-neck flask was purged with nitrogen for 35 min. The reaction temperature was raised to 250 °C and held at temperature for 10 min. The flask was then cooled quickly to room temperature using a cold-water bath. Hexanes (5 mL) and ethanol (15 mL) were added to precipitate and clean the material, and the solid was collected through centrifugation at 8000 rpm for 10 min.

2.5.6 Synthesis of CoS_2

Synthesis of CoS_2 was carried out following a previously reported procedure.[61] In a typical synthesis, $Co(NO_3)_2 \cdot 6H_2O$ (2.91 g, 0.01 mol) was dissolved in hot butanol (25 mL). Thiourea (3.04 g, 9.04 mol) was added and the mixture was heated to boiling until all solids were dissolved. The color of the solution changed from red to blue with a blue solid precipitating over time, indicating the formation of $Co(thiourea)_4(NO_3)_2$. The blue solid, cobalt thiourea complex, was collected through filtration, washed with diethyl ether, and dried under vacuum. The blue solid was annealed at 400 °C for 2 hours under inert atmosphere to obtain the CoS_2 phase.

2.5.7 Synthesis of $Co(OH)_2$

The synthesis of $Co(OH)_2$ nanoplatelets was carried out following a previously reported procedure.[62] Cobalt(II) nitrate hexahydrate (1.83 g, 10.0 mmol) was dissolved in 40 mL of Nanopure water and degassed at 70 °C for 30 min. Then, 10 mL of 2 mM NaOH was added and the solution was aged for 1 hour at 70 °C. After cooling to room temperature, the pink suspension was centrifuged at 8500 rpm for 10 minutes. The supernatant was decanted and the remaining solid

was rinsed thrice using 10 mL of H_2O and once with 10 mL of EtOH. After decanting the solvent, the pink solid was dried under vacuum at 60 °C for 18 hours.

2.5.8 Physical Characterization Methods

Low-resolution transmission electron microscopy (TEM) images were acquired using an FEI Tecnai T20 TEM equipped with a 200 kV LaB_6 filament. Low-resolution high-angle annular dark-field scanning transmission electron microscopy (HAADF-STEM) and energy-dispersive spectroscopy (EDS) mapping were obtained on an FEI Talos F200X S/TEM with a 200 kV X-FEG field-emission source and a super X-EDS system. High-resolution HAADF-STEM images were collected using a Thermo Scientific Themis Z, a spherical aberration corrected S/TEM with a 300 kV X-FEG field-emission source. Associated EDS spectra were obtained with a quad-silicon FEI Super X drift detector.

In order to obtain atomic-resolution HAADF-STEM images, it is critical to remove all organic ligand and solvent residue from the TEM sample. Colloidal Co-WS_2 samples for HR-STEM were cleaned four additional times with ethanol and hexanes prior to drop casting onto a Au grid coated with an ultrathin carbon film (Ted Pella). The Au grid was then submerged in a suspension of carbon black in hexanes, and N_2 gas was bubbled into the solution for 1 min to agitate the suspension.[63] The Au grid was air-dried and stored under inert atmosphere prior to imaging.

Powder X-ray diffraction (XRD) measurements were acquired using a Panalytical Empyrean Powder X-ray Diffractometer. A Panalytical Epsilon 4 X-ray fluorescence spectrometer (XRF) was used for metal quantification. Commercial WS_2 powder and $CoCl_2 \cdot 6\ H_2O$ were used to create a calibration curve for XRF measurements.

X-ray absorption spectroscopy (XAS) experiments were carried out at the 10-ID and 10-BM beamlines at the Advanced Photon Source, Argonne National Laboratory. Samples were pressed into a self-supporting pellet, and spectra were obtained in transmission mode at room temperature. The Demeter software package was used to analyze the collected data.[64] Data was collected at the Co K-edge (7.7089 keV) using metallic Co foil for energy calibration. EXAFS

coordination parameters were obtained by a least-squares fit in R-space of the k^2-weighted Fourier transform data from 2.5 to 8.5 $Å^{-1}$ for Co-WS_2 samples and 2.5 to 9.0 $Å^{-1}$ for control samples. A Co foil reference sample was first fit to its known crystallographic parameters to obtain an amplitude reduction factor (S_0^2) for the Co K-edge. EXAFS fitting of the first coordination shell was carried out between 1.1 and 2.3 Å in R-space. Fittings were done by refining bond distances (R), coordination numbers (CN) and energy shift (E_0). The Debye-Waller factor ($\Delta\sigma^2$) was kept constant for each sample.

2.5.9 Electrochemical Measurements.

Electrochemical experiments were conducted on a Pine WaveDriver 20 Bipotentiostat. A catalyst ink was obtained by sonicating the catalyst powder in a solution containing 75.6% water, 24% IPA, and 0.4% Nafion (v/v) to obtain a nominal concentration of 7 mM by WS_2. The working electrode was prepared by drop casting 10 μL of 7 mM solution onto a polished glassy carbon electrode with 5 mm diameter. The catalyst film was air dried for 25 minutes at a rotation speed of 700 rpm. The counter electrode was a graphite rod. The electrolyte used for all electrochemical experiments besides the stability testing was 1.0 M sodium phosphate buffer solution (PBS, pH 7, 99%). Currents are reported with anodic current as positive and cathodic current as negative. Potentials were measured against a Ag/AgCl reference electrode (3 M NaCl) and converted to the RHE reference scale using:

$$E\ (\text{vs RHE}) = E\ (\text{vs Ag/AgCl}) + 0.210\ \text{V} + 0.0591\ \text{V}*\text{pH}$$

Oxygen reduction reaction (ORR) voltammetry was carried out using a rotating ring-disk electrode (RRDE) in a single-compartment glass cell (Pine) containing 150 mL of 1.0 M PBS electrolyte. The solution was purged with O_2 for at least 30 min prior to the start of the experiment. For all ORR experiments, a rotation rate of 1600 rpm is utilized. One cathodic linear sweep voltammetry (LSV) scan is collected at 10 mV/s prior to the reported anodic LSV, obtained by scanning at 1 mV/s from 0.0 V to 0.9 V vs. RHE. The onset potential (E_{onset}) for ORR is defined to be the potential at which the ORR current density reaches –0.1 mA/cm^2. All E_{onset} values are obtained from an average of three sample runs to account for variability in the electrode drop-drying process, and the error bar reflects the standard deviation.

The Pt ring in the rotating-ring disk electrode was held at 1.26 V vs. RHE during ORR linear sweep voltammetry. From the ring current, the peroxide selectivity is calculated based on the following equations:

$$mol\ H_2O_2 = \frac{I_R}{2N}$$

$$\%\ H_2O_2 = \frac{\frac{2I_R}{N}}{\frac{I_R}{N} + I_D}$$

where I_R = ring current
I_D = disk current
N = 0.249, the collection efficiency of the Pt ring

Collection efficiency, N, was experimentally measured on our RRDE setup. LSV scans were performed in 0.1 M KOH containing 10 mM potassium ferricyanide ($K_3Fe(CN)_6$). The Pt ring was held at 1.57 V vs. RHE and the glassy carbon disk was scanned from 1.432 V to 0.632 V vs. RHE. The collection efficiency was calculated by taking a ratio of the limiting ring and disk current densities. Over six rotation rates, the average value for N was calculated to be 0.249 ± 0.0080.

Uncompensated resistances were measured for a set of Co-WS_2 samples, which ranged from 20-36 Ω in 1 M PBS electrolyte. Catalytic measurements are reported without *i*R compensation. To assess the stability of Co-WS_2 and CoS_x catalysts in ORR, accelerated CV scanning at 200 mV/s was performed in a high-purity 1.0 M sodium phosphate electrolyte (pH 7, 99.9%). During the stability test, anodic LSV scans at 1 mV/s were obtained in the 1st, 5th, 20th, and 200th scan while all intervening CV scans were collected at 200 mV/s.

2.6 Acknowledgements

This research was supported by Purdue University and the National Science Foundation under Grant No. CHE-2045013. EM and WH acknowledge support from the Purdue Research Foundation. We acknowledge Dr. Rosa E. Diaz for assistance in collecting high resolution HAADF-STEM images. We thank Dr. Yujia Ding, Dr. Kamil Kucuk, Dr. Mark Warren, and Dr. Joshua Wright for their help with XAS experiments. Use of the Advanced Photon Source is supported by the U.S. Department of Energy, Office of Science, Office of Basic Energy Sciences,

under Contract DE-AC02-06CH11357. MCRAT operations are supported by the Department of Energy and MRCAT member institutions.

2.7 Supplemental Information

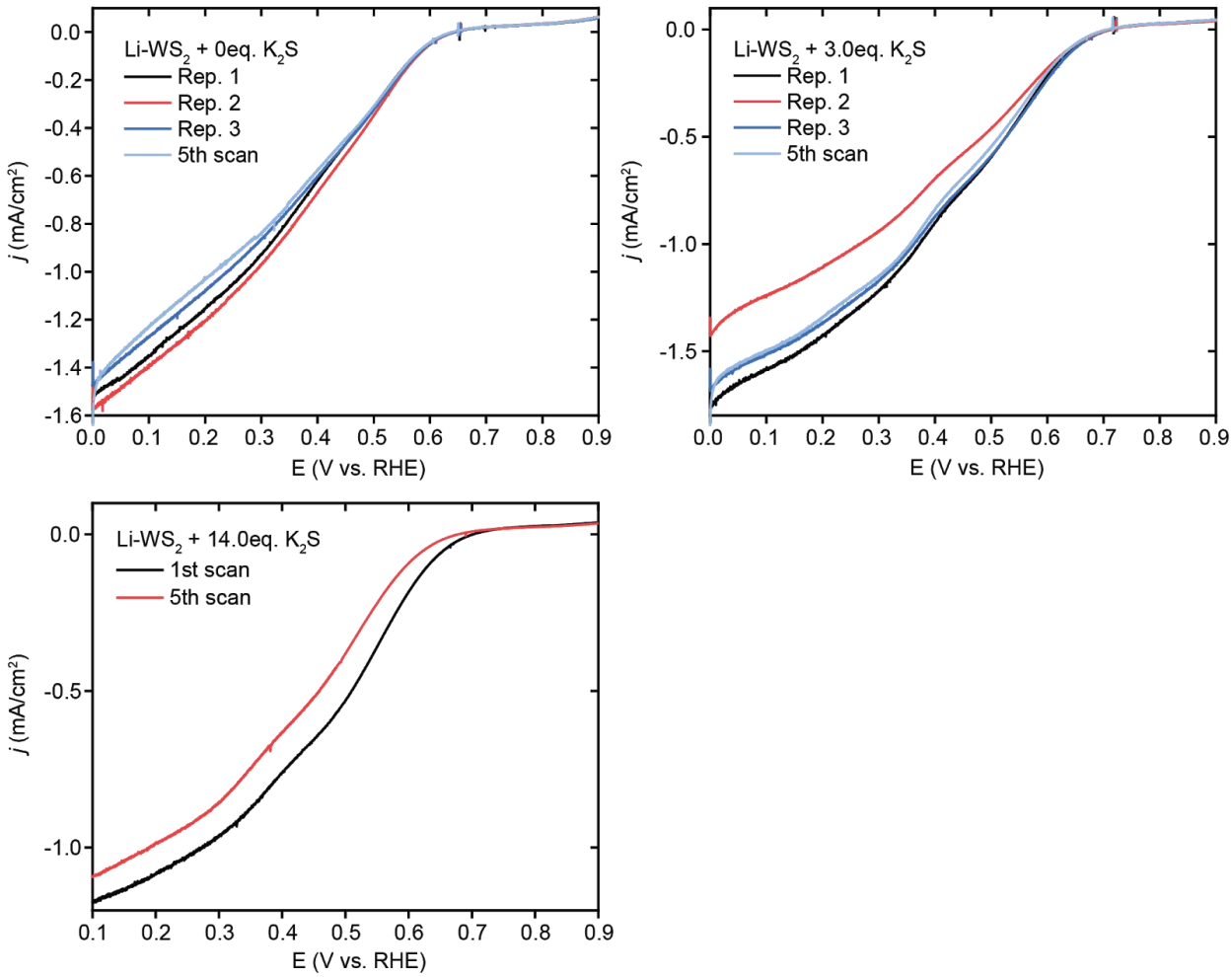

Figure 2.25. ORR data on Li-WS_2 and sulfur annealed variants showing the 1st LSV scan for three independent runs (Rep. 1-3) and 5th LSV scan.

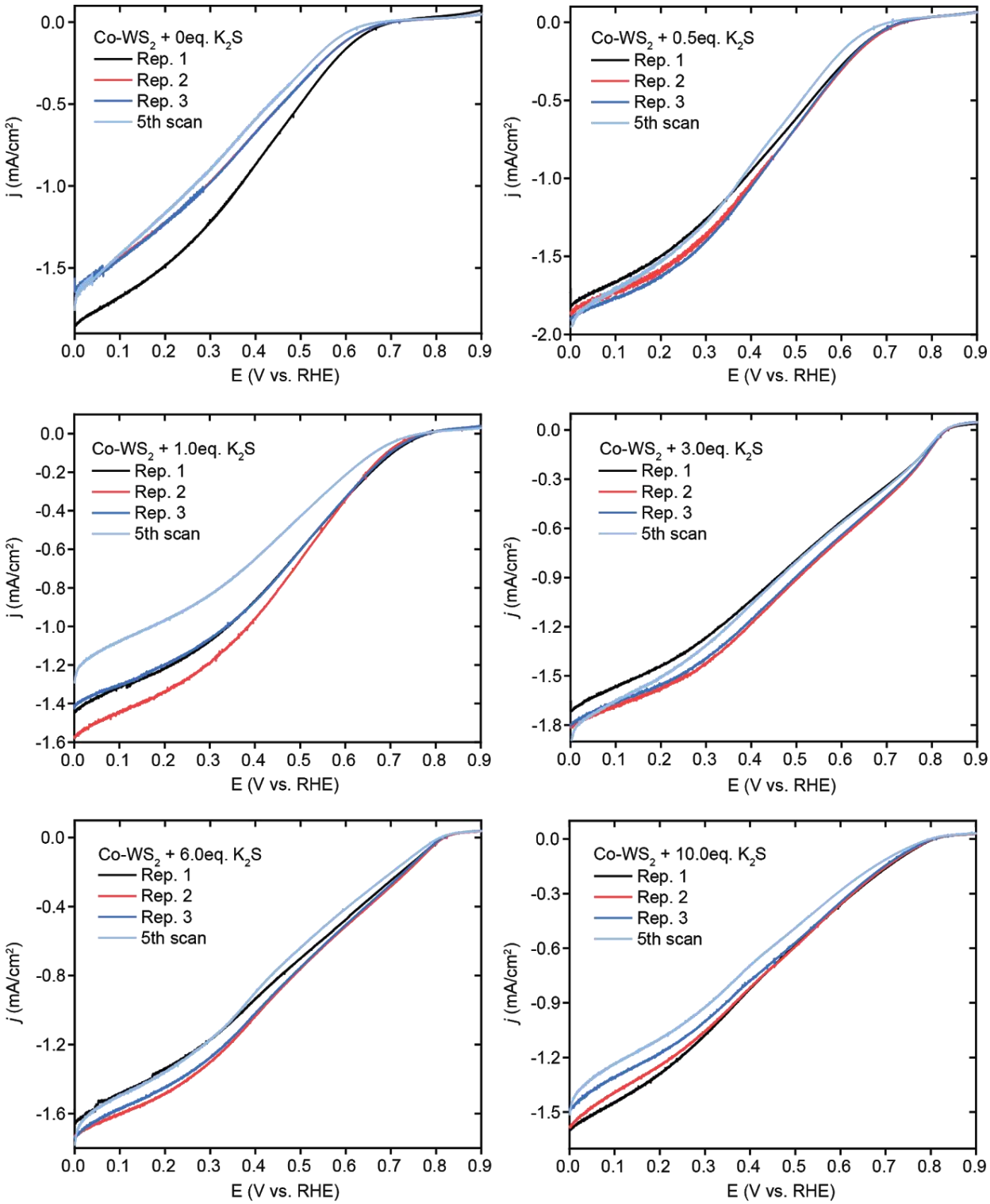

Figure 2.26. ORR data on Co-WS_2 + xK_2S samples showing the 1st LSV scan for three independent runs (Rep. 1-3) and 5th LSV scan.

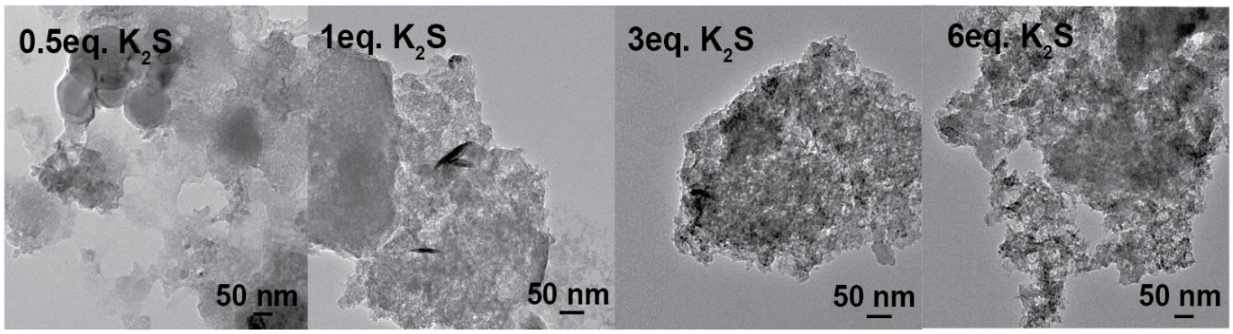

Figure 2.27. TEM images of Co-WS_2 + xK_2S samples after PBS treatment.

2.8 References

1. Behret, H.; Binder, H.; Sandstede, G. Electrocatalytic Oxygen Reduction with Thiospinels and Other Sulfides of Transition-Metals. *Electrochim. Acta* **1975**, *20*, 111-117.

2. Behret, H.; Binder, H.; Clauberg, W.; Sandstede, G. Comparison of Reaction-Mechanisms of Electrocatalytic Oxygen Reduction Using Transition-Metal Thiospinels and Chelates. *Electrochim. Acta* **1978**, *23*, 1023-1029.

3. Feng, Y. J.; Gago, A.; Timperman, L.; Alonso-Vante, N. Chalcogenide metal centers for oxygen reduction reaction: Activity and tolerance. *Electrochim. Acta* **2011**, *56*, 1009-1022.

4. Gao, M. R.; Jiang, J.; Yu, S. H. Solution-Based Synthesis and Design of Late Transition Metal Chalcogenide Materials for Oxygen Reduction Reaction (ORR). *Small* **2012**, *8*, 13-27.

5. Vij, V.; Sultan, S.; Harzandi, A. M.; Meena, A.; Tiwari, J. N.; Lee, W. G.; Yoon, T.; Kim, K. S. Nickel-Based Electrocatalysts for Energy-Related Applications: Oxygen Reduction, Oxygen Evolution, and Hydrogen Evolution Reactions. *ACS Catal.* **2017**, *7*, 7196-7225.

6. Yan, B.; Concannon, N. M.; Milshtein, J. D.; Brushett, F. R.; Surendranath, Y. A Membrane-Free Neutral pH Formate Fuel Cell Enabled by a Selective Nickel Sulfide Oxygen Reduction Catalyst. *Angew. Chem. Int. Ed*. **2017**, *56*, 7496-7499.

7. Wang, H. L.; Liang, Y. Y.; Li, Y. G.; Dai, H. J. Co1-xS-Graphene Hybrid: A High-Performance Metal Chalcogenide Electrocatalyst for Oxygen Reduction. *Angew. Chem. Int. Ed.* **2011**, *50*, 10969-10972.

8. Zhu, L.; Susac, D.; Teo, M.; Wong, K. C.; Wong, P. C.; Parsons, R. R.; Bizzotto, D.; Mitchell, K. A. R.; Campbell, S. A. Investigation of CoS_2-based thin films as model catalysts for the oxygen reduction reaction. *J. Catal.* **2008**, *258*, 235-242.

9. Susac, D.; Zhu, L.; Teo, M.; Sode, A.; Wong, K. C.; Wong, P. C.; Parsons, R. R.; Bizzotto, D.; Mitchell, K. A. R.; Campbell, S. A. Characterization of FeS_2-based thin films as model catalysts for the oxygen reduction reaction. *J. Phys. Chem. C* **2007**, *111*, 18715-18723.

10. Arunchander, A.; Peera, S. G.; Sahu, A. K. Self-Assembled Manganese Sulfide Nanostructures on Graphene as an Oxygen Reduction Catalyst for Anion Exchange Membrane Fuel Cells. *ChemElectroChem* **2017**, *4*, 1544-1553.

11. Falkowski, J. M.; Surendranath, Y. Metal Chalcogenide Nanofilms: Platforms for Mechanistic Studies of Electrocatalysis. *ACS Catal*. **2015**, *5*, 3411-3416.

12. Cao, Y. F.; Meng, Y. Y.; Huang, S. C.; He, S. M.; Li, X. H.; Tong, S. F.; Wu, M. M. Nitrogen-, Oxygen-and Sulfur-Doped Carbon-Encapsulated Ni_3S_2 and NiS Core Shell Architectures: Bifunctional Electrocatalysts for Hydrogen Evolution and Oxygen Reduction Reactions. *ACS Sustain. Chem. Eng.* **2018**, *6*, 15582-15590.

13. Ganesan, P.; Prabu, M.; Sanetuntikul, J.; Shanmugam, S. Cobalt Sulfide Nanoparticles Grown on Nitrogen and Sulfur Codoped Graphene Oxide: An Efficient Electrocatalyst for Oxygen Reduction and Evolution Reactions. *ACS Catal*. **2015**, *5*, 3625-3637.

14. Chen, B. L.; Li, R.; Ma, G. P.; Gou, X. L.; Zhu, Y. Q.; Xia, Y. D. Cobalt sulfide/N,S codoped porous carbon core-shell nanocomposites as superior bifunctional electrocatalysts for oxygen reduction and evolution reactions. *Nanoscale* **2015**, *7*, 20674-20684.

15. Zhu, Q. L.; Xia, W.; Akita, T.; Zou, R. Q.; Xu, Q. Metal-Organic Framework-Derived Honeycomb-Like Open Porous Nanostructures as Precious-Metal-Free Catalysts for Highly Efficient Oxygen Electroreduction. *Adv. Mater.* **2016**, *28*, 6391-6398.

16. Wu, Z. X.; Wang, J.; Song, M.; Zhao, G. M.; Zhu, Y.; Fu, G. T.; Liu, X. E. Boosting Oxygen Reduction Catalysis with N-doped Carbon Coated Co_9S_8 Microtubes. *ACS Appl. Mater. Interfaces* **2018**, *10*, 25415-25421.

17. Zhou, Y. X.; Yao, H. B.; Wang, Y.; Liu, H. L.; Gao, M. R.; Shen, P. K.; Yu, S. H. Hierarchical Hollow Co_9S_8 Microspheres: Solvothermal Synthesis, Magnetic, Electrochemical, and Electrocatalytic Properties. *Chem-Eur. J.* **2010**, *16*, 12000-12007.

18. Tang, Y. P.; Jing, F.; Xu, Z. X.; Zhang, F.; Mai, Y. Y.; Wu, D. Q. Highly Crumpled Hybrids of Nitrogen/Sulfur Dual-Doped Graphene and Co_9S_8 Nanoplates as Efficient Bifunctional Oxygen Electrocatalysts. *ACS Appl. Mater. Interfaces* **2017**, *9*, 12340-12347.

19. Fu, S. F.; Zhu, C. Z.; Song, J. H.; Feng, S.; Du, D.; Engelhard, M. H.; Xiao, D. D.; Li, D. S.; Lin, Y. H. Two-Dimensional N,S-Codoped Carbon/Co_9S_8 Catalysts Derived from $Co(OH)_2$ Nanosheets for Oxygen Reduction Reaction. *ACS Appl. Mater. Interfaces* **2017**, *9*, 36755-36761.

20. Xiao, Z.; Xiao, G. Z.; Shi, M. H.; Zhu, Y. Homogeneously Dispersed Co_9S_8 Anchored on Nitrogen and Sulfur Co-Doped Carbon Derived from Soybean as Bifunctional Oxygen Electrocatalysts and Supercapacitors. *ACS Appl. Mater. Interfaces* **2018**, *10*, 16436-16448.

21. Zhang, S. L.; Zhai, D.; Sun, T. T.; Han, A. J.; Zhai, Y. L.; Cheong, W. C.; Liu, Y.; Su, C. L.; Wang, D. S.; Li, Y. D. In situ embedding Co_9S_8 into nitrogen and sulfur codoped hollow porous carbon as a bifunctional electrocatalyst for oxygen reduction and hydrogen evolution reactions. *Appl. Catal., B* **2019**, *254*, 186-193.

22. Bai, F.; Qu, X.; Wang, J.; Chen, X.; Yang, W. S. Confinement Catalyst of Co_9S_8@N-Doped Carbon Derived from Intercalated $Co(OH)_2$ Precursor and Enhanced Electrocatalytic Oxygen Reduction Performance. *ACS Appl. Mater. Interfaces* **2020**, *12*, 33740-33750.

23. Sidik, R. A.; Anderson, A. B. Co_9S_8 as a catalyst for electroreduction of O^{-2}: Quantum chemistry predictions. *J. Phys. Chem. B* **2006**, *110*, 936-941.

24. Yan, B.; Krishnamurthy, D.; Hendon, C. H.; Deshpande, S.; Surendranath, Y.; Viswanathan, V. Surface Restructuring of Nickel Sulfide Generates Optimally Coordinated Active Sites for Oxygen Reduction Catalysis. *Joule* **2017**, *1*, 600-612.

25. Susac, D.; Sode, A.; Zhu, L.; Wong, P. C.; Teo, M.; Bizzotto, D.; Mitchell, K. A. R.; Parsons, R. R.; Campbell, S. A. A methodology for investigating new nonprecious metal catalysts for PEM fuel cells. *J. Phys. Chem. B* **2006**, *110*, 10762-10770.

26. Yang, X. F.; Wang, A. Q.; Qiao, B. T.; Li, J.; Liu, J. Y.; Zhang, T. Single-Atom Catalysts: A New Frontier in Heterogeneous Catalysis. *Acc. Chem. Res*. **2013**, *46*, 1740-1748.

27. Wang, A. Q.; Li, J.; Zhang, T. Heterogeneous single-atom catalysis. *Nat. Rev. Chem*. **2018**, *2*, 65-81.

28. Giannakakis, G.; Flytzani-Stephanopoulos, M.; Sykes, E. C. H. Single-Atom Alloys as a Reductionist Approach to the Rational Design of Heterogeneous Catalysts. *Acc. Chem. Res*. **2019**, *52*, 237-247.

29. Xin, Y.; Zhang, N. N.; Li, Q.; Zhang, Z. L.; Cao, X. M.; Zheng, L. R.; Zeng, Y. W.; Anderson, J. A. Active Site Identification and Modification of Electronic States by Atomic-Scale Doping To Enhance Oxide Catalyst Innovation. *ACS Catal*. **2018**, *8*, 1399-1404.

30. Gan, G. Q.; Li, X. Y.; Wang, L.; Fan, S. Y.; Mu, J. C.; Wang, P. L.; Chen, G. H. Active Sites in Single-Atom Fe-N_x-C Nanosheets for Selective Electrochemical Dechlorination of 1,2-Dichloroethane to Ethylene. *ACS Nano* **2020**, *14*, 9929-9937.

31. Xu, Y.; Chu, M. Y.; Liu, F. F.; Wang, X. C.; Liu, Y.; Cao, M. H.; Gong, J.; Luo, J.; Lin, H. P.; Li, Y. Y.; Zhang, Q. Revealing the Correlation between Catalytic Selectivity and the Local Coordination Environment of Pt Single Atom. *Nano Lett*. **2020**, *20*, 6865-6872.

32. Zhang, J. Q.; Zhao, Y. F.; Chen, C.; Huang, Y. C.; Dong, C. L.; Chen, C. J.; Liu, R. S.; Wang, C. Y.; Yan, K.; Li, Y. D.; Wang, G. X. Tuning the Coordination Environment in Single-Atom Catalysts to Achieve Highly Efficient Oxygen Reduction Reactions. *J. Am. Chem. Soc*. **2019**, *141*, 20118-20126.

33. Wang, Q.; Huang, X.; Zhao, Z. L.; Wang, M. Y.; Xiang, B.; Li, J.; Feng, Z. X.; Xu, H.; Gu, M. Ultrahigh-Loading of Ir Single Atoms on NiO Matrix to Dramatically Enhance Oxygen Evolution Reaction. *J. Am. Chem. Soc.* **2020**, *142*, 7425-7433.

34. Zitolo, A.; Goellner, V.; Armel, V.; Sougrati, M. T.; Mineva, T.; Stievano, L.; Fonda, E.; Jaouen, F. Identification of catalytic sites for oxygen reduction in iron- and nitrogen-doped graphene materials. *Nat. Mater*. **2015**, *14*, 937-942.

35. Zhang, L. L.; Wang, A. Q.; Wang, W. T.; Huang, Y. Q.; Liu, X. Y.; Miao, S.; Liu, J. Y.; Zhang, T. Co-N-C Catalyst for C-C Coupling Reactions: On the Catalytic Performance and Active Sites. *ACS Catal*. **2015**, *5*, 6563-6572.

36. Hu, M. Y.; Li, S. N.; Zheng, S. S.; Liang, X. H.; Zheng, J. X.; Pan, F. Tuning Single-Atom Catalysts of Nitrogen-Coordinated Transition Metals for Optimizing Oxygen Evolution and Reduction Reactions. *J. Phys. Chem. C* **2020**, *124*, 13168-13176.

37. Liu, W. G.; Zhang, L. L.; Yan, W. S.; Liu, X. Y.; Yang, X. F.; Miao, S.; Wang, W. T.; Wang, A. Q.; Zhang, T. Single-atom dispersed Co-N-C catalyst: structure identification and performance for hydrogenative coupling of nitroarenes. *Chem. Sci*. **2016**, *7*, 5758-5764.

38. Liu, W. G.; Zhang, L. L.; Liu, X.; Liu, X. Y.; Yang, X. F.; Miao, S.; Wang, W. T.; Wang, A. Q.; Zhang, T. Discriminating Catalytically Active FeN_x Species of Atomically Dispersed Fe-N-C Catalyst for Selective Oxidation of the C-H Bond. *J. Am. Chem. Soc*. **2017**, *139*, 10790-10798.

39. Zitolo, A.; Ranjbar-Sahraie, N.; Mineva, T.; Li, J. K.; Jia, Q. Y.; Stamatin, S.; Harrington, G. F.; Lyth, S. M.; Krtil, P.; Mukerjee, S.; Fonda, E.; Jaouen, F. Identification of catalytic sites in cobalt-nitrogen-carbon materials for the oxygen reduction reaction. *Nat. Commun.*, **2017**, *8*.

40. Yin, P. Q.; Yao, T.; Wu, Y.; Zheng, L. R.; Lin, Y.; Liu, W.; Ju, H. X.; Zhu, J. F.; Hong, X.; Deng, Z. X.; Zhou, G.; Wei, S. Q.; Li, Y. D. Single Cobalt Atoms with Precise N-Coordination as Superior Oxygen Reduction Reaction Catalysts. *Angew. Chem. Int. Ed.*, **2016**, *55*, 10800-10805.

41. Vancso, P.; Popov, Z. I.; Peto, J.; Ollar, T.; Dobrik, G.; Pap, J. S.; Hwang, C. Y.; Sorokin, P. B.; Tapaszto, L. Transition Metal Chalcogenide Single Layers as an Active Platform for Single-Atom Catalysis. *ACS Energy Lett*. **2019**, *4*, 1947-1953.

42. Ji, L.; Yan, P. F.; Zhu, C. H.; Ma, C. Y.; Wu, W. Z.; Wei, C.; Shen, Y. L.; Chu, S. Q.; Wang, J. O.; Du, Y.; Chen, J.; Yang, X. A.; Xu, Q. One-pot synthesis of porous 1T-phase MoS_2 integrated with single-atom Cu doping for enhancing electrocatalytic hydrogen evolution reaction. *Appl. Catal., B* **2019**, *251*, 87-93.

43. Qi, K.; Cui, X. Q.; Gu, L.; Yu, S. S.; Fan, X. F.; Luo, M. C.; Xu, S.; Li, N. B.; Zheng, L. R.; Zhang, Q. H.; Ma, J. Y.; Gong, Y.; Lv, F.; Wang, K.; Huang, H. H.; Zhang, W.; Guo, S. J.; Zheng, W. T.; Liu, P. Single-atom cobalt array bound to distorted 1T MoS_2 with ensemble effect for hydrogen evolution catalysis. *Nat. Commun*. **2019**, *10*, 5231.

44. Wang, Q.; Zhao, Z. L.; Dong, S.; He, D. S.; Lawrence, M. J.; Han, S. B.; Cai, C.; Xiang, S. H.; Rodriguez, P.; Xiang, B.; Wang, Z. G.; Liang, Y. Y.; Gu, M. Design of active nickel single-atom decorated MoS_2 as a pH-universal catalyst for hydrogen evolution reaction. *Nano Energy* **2018**, *53*, 458-467.

45. Meza, E.; Diaz, R. E.; Li, C. W. Solution-Phase Activation and Functionalization of Colloidal WS_2 Nanosheets with Ni Single Atoms. *ACS Nano* **2020**, *14*, 2238-2247.

46. Mahler, B.; Hoepfner, V.; Liao, K.; Ozin, G. A. Colloidal Synthesis of 1T-WS_2 and 2H-WS_2 Nanosheets: Applications for Photocatalytic Hydrogen Evolution. *J. Am. Chem. Soc*. **2014**, *136*, 14121-14127.

47. Tsai, H. L.; Heising, J.; Schindler, J. L.; Kannewurf, C. R.; Kanatzidis, M. G. Exfoliated-restacked phase of WS_2. *Chem. Mater.*, **1997**, *9*, 879-882.

48. Chou, S. S.; Huang, Y. K.; Kim, J.; Kaehr, B.; Foley, B. M.; Lu, P.; Dykstra, C.; Hopkins, P. E.; Brinker, C. J.; Huang, J. X.; Dravid, V. P. Controlling the Metal to Semiconductor Transition of MoS_2 and WS_2 in Solution. *J. Am. Chem. Soc.*, **2015**, *137*, 1742-1745.

49. Uchikoshi1, M.; Shinoda1, K. Determination of structures of cobalt(II)-chloro complexes in hydrochloric acid solutions by X-ray absorption spectroscopy at 298 K. *Struct. Chem*. **2019**, *30*, 945-954.

50. van Haandel, L.; Smolentsev, G.; van Bokhoven, J. A.; Hensen, E. J. M.; Weber, T. Evidence of Octahedral Co-Mo-S Sites in Hydrodesulfurization Catalysts as Determined by Resonant Inelastic X-ray Scattering and X-ray Absorption Spectroscopy. *ACS Catal*. **2020**, *10*, 10978-10988.

51. Sasaki, S.; Fujino, K.; Takeuchi, Y. X-Ray Determination of Electron-Density Distributions in Oxides, MgO, MnO, CoO, and NiO, and Atomic Scattering Factors of Their Constituent Atoms. *Proc. Jpn. Acad. B*, **1979**, *55*, 43-48.

52. Wilkinson, M. K.; Cable, J. W.; Wollan, E. O.; Koehler, W. C. Neutron Diffraction Investigations of the Magnetic Ordering in $FeBr_2$, $CoBr_2$, $FeCl_2$, and $CoCl_2$. *Phys. Rev.*, **1959**, *113*, 497-507.

53. Alsén, N. Röntgenographische Untersuchung der Kristallstrukturen von Magnetkies, Breithauptit, Pentlandit, Millerit und verwandten Verbindungen. *GFF*, **1925**, *47*, 19-72.

54. Nowack, E.; Schwarzenbach, D.; Hahn, T. Charge-Densities in CoS_2 and NiS_2 (Pyrite Structure). *Acta Crystallogr. B*, **1991**, *47*, 650-659.

55. Knop, O.; Reid, K. I. G.; Sutarno; Nakagawa, Y. Chalkogenides of the transition elements. VI. X-Ray, neutron, and magnetic investigation of the spinels Co_3O_4, $NiCo_2O_4$, Co_3S_4, and $NiCo_2S_4$. *Can. J. Chem.*, **1968**, *46*, 3463-3476.

56. Geller, S. Refinement of the crystal structure of Co_9S_8. *Acta Crystallogr.*, **1962**, *15*, 1195-1198.

57. Falkowski, J. M.; Concannon, N. M.; Yan, B.; Surendranath, Y. Heazlewoodite, Ni_3S_2: A Potent Catalyst for Oxygen Reduction to Water under Benign Conditions. *J. Am. Chem. Soc*. **2015**, *137*, 7978-7981.

58. Cai, P. W.; Huang, J. H.; Chen, J. X.; Wen, Z. H. Oxygen-Containing Amorphous Cobalt Sulfide Porous Nanocubes as High-Activity Electrocatalysts for the Oxygen Evolution Reaction in an Alkaline/Neutral Medium. *Angew. Chem. Int. Ed*. **2017**, *56*, 4858-4861.

59. Zhao, W. W.; Bothra, P.; Lu, Z. Y.; Li, Y. B.; Mei, L. P.; Liu, K.; Zhao, Z. H.; Chen, G. X.; Back, S.; Siahrostami, S.; Kulkarni, A.; Norskov, J. K.; Bajdich, M.; Cui, Y. Improved Oxygen Reduction Reaction Activity of Nanostructured CoS_2 through Electrochemical Tuning. *ACS Appl. Energy Mater*. **2019**, *2*, 8605-8614.

60. Chang, S.-H.; Lu, M.-D.; Tung, Y.-L.; Tuan, H.-Y. Gram-Scale Synthesis of Catalytic Co_9S_8 Nanocrystal Ink as a Cathode Material for Spray-Deposited, Large-Area Dye-Sensitized Solar Cells. *ACS Nano* **2013**, *7*, 9443-9451.

61. Kumar, N.; Raman, N.; Sundaresan, A. Synthesis and Properties of Cobalt Sulfide Phases: CoS_2 and Co_9S_8. *Z. Anorg. Allg. Chem*. **2014**, *640*, 1069-1074.

62. Cheng, J.; Chen, X.; Wu, J.-S.; Liu, F.; Zhang, X.; Dravid, V. P., Porous Cobalt Oxides with Tunable Hierarchical Morphologies for Supercapacitor Electrodes. *CrystEngComm* **2012**, *14*, 6702-6709.

63. Li, C.; Tardajos, A. P.; Wang, D.; Choukroun, D.; Van Daele, K.; Breugelmans, T.; Bals, S. A simple method to clean ligand contamination on TEM grids. *Ultramicroscopy,* **2021**, *221*.

64. Ravel, B.; Newville, M. ATHENA, ARTEMIS, HEPHAESTUS: data analysis for X-ray absorption spectroscopy using IFEFFIT. *J. Synchrotron Radiat.,* **2005**, *12*, 537-541.